Charge transport in bulk hematite and at the hematite/water interface

Christian Ahart

A dissertation submitted in partial fulfillment

of the requirements for the degree of

Doctor of Philosophy

of

University College London.

Department of Physics and Astronomy

University College London

August 8, 2022

I, Christian Ahart, confirm that the work presented in this thesis is my own. Where information has been derived from other sources, I confirm that this has been indicated in the work.

Abstract

Transition metal oxide materials have attracted much attention for photoelectrochemical water splitting, but problems remain, e.g. the sluggish transport of excess charge carriers in these materials, which is not well understood. In this thesis I will show how periodic, spin-constrained and gap-optimised hybrid density functional theory can be used to uncover the nature and transport mechanisms of excess electrons and electron holes in a widely used water splitting material, hematite ($\alpha-Fe_2O_3$). I will show that upon ionisation the electron hole relaxes from a delocalized band state to a polaron localised on a single iron atom with localisation induced by tetragonal distortion of the 6 surrounding iron-oxygen bonds. This distortion is responsible for the sluggish hopping transport in bulk hematite, characterised by an activation energy of 70 meV and a hole mobility of 0.031 cm^2/Vs. By contrast, the excess electron induces a smaller distortion of the iron-oxygen bonds resulting in delocalisation over two neighbouring Fe units. I will show that 2-site delocalisation is advantageous for charge transport due to the larger spatial displacements per transfer step. As a result, the electron mobility is predicted to be a factor of 3 higher than the hole mobility, 0.098 cm^2/Vs, in qualitative agreement with experimental observations. Extending this analysis to the hematite/liquid water interface, I will show that both excess electrons and electron holes localise at the interface with qualitatively similar structures to bulk hematite. However, the presence of the interface breaks the symmetry present in the bulk crystal and as a result the hole mobility is expected to be greatly reduced. These calculations provide new fundamental insights essential for a better understanding of rate-limiting transport processes governing photocatalytic water splitting efficiency at the hematite/liquid water interface.

Impact Statement

With increasing environmental concerns, it is necessary to pursue more sustainable and more efficient materials. Iron oxides and oxyhydroxides are highly abundant, cheap and stable and have many properties such as visible spectrum band gaps which make them ideal candidates in photoelectrochemical applications. Hematite ($\alpha-Fe_2O_3$) in particular has received much attention as a photoanode material for water splitting, however problems remain including low mobility and short carrier lifetimes due to electron-hole recombination. This thesis provides new fundamental insight into the nature and transport mechanisms of both excess electrons and electron holes, essential for a better understanding of the rate-limiting transport processes governing photocatalytic water splitting efficiency at the hematite/liquid water interface.

This thesis demonstrates how periodic, spin-constrained and gap-optimised hybrid density functional theory can be used to calculate all the electron transfer parameters required to predict the charge mobility in bulk hematite. This method is generally applicable to all semiconducting materials, and may be applied to other oxides of technological interest for the study of intrinsic charge transfer processes or for charge transfer between defects. Moreover, constrained density functional theory is well suited for the study of interfacial charge transfer processes between different semiconductors or between semiconductor electrodes and liquids. It could thus become an essential tool for the emerging field of *ab-initio* electrochemistry.

Acknowledgements

I would like to first thank my supervisor Prof Jochen Blumberger for his help and guidance throughout my PhD. I would also like to thank Dr Zdenek Futera for his kind support during the first months of my PhD, Dr Guido von Rudorff for performing earlier calculations on neutral hematite, Dr Philipp Schienbein who continued this work with a machine learning model as well as the past and current group members: Dr Matt Ellis, Dr Xiuyun Jiang, Dr Samuele Giannini, Dr Xioajing Wu, Dr Lijljana Stojanovic, Dr Roohollah Hafizi, Jan Elsner, Dr Orestis Ziogos, Dr Wei-Tao Peng and Nora Gildemeister.

I would also like to thank all my family, with special thanks to my Mum and Dad for their support. Most of all, I would like to thank my partner Xia Zeng for her patience and encouragement throughout my PhD.

Finally I would like to thank my collaborator and co-sponsor Dr Kevin Rosso from Pacific Northwest National Laboratory (PNNL), and acknowledge my funding entity and computational resources. My PhD studentship is cosponsored by University College London and Pacific Northwest National Laboratory (PNNL) through its BES Geosciences program supported by the U.S. Department of Energy's Office of Science, Office of Basic Energy Sciences, Chemical Sciences, Geosciences and Biosciences Division. Via membership of the UK's HEC Materials Chemistry Consortium, which is funded by EPSRC (EP/L000202, EP/R029431), this work used the ARCHER UK National Supercomputing Service (http://www.archer.ac.uk), as well as the UK Materials and Molecular Modeling (MMM) Hub, which is partially funded by EPSRC (EP/P020194), for computational resources.

List of Publications

Parts of this thesis have been published as follows:

1. Christian S. Ahart, Jochen Blumberger and Kevin M. Rosso. Polaronic structure of excess electrons and holes for a series of bulk iron oxides. *Phys. Chem. Chem. Phys.* 22, 10699–10709, 2020.

2. Christian S. Ahart, Kevin M. Rosso and Jochen Blumberger. Electron and Hole Mobilities in Bulk Hematite from Spin-Constrained Density Functional Theory. *J. Am. Chem. Soc.* 144, 4623–4632, 2022.

3. Christian S. Ahart, Kevin M. Rosso and Jochen Blumberger. Implementation and Validation of Constrained Density Functional Theory Forces in the CP2K Package. *J. Chem. Theory Comput.* 18, 4438–4446, 2022.

Contents

List of Figures

List of Tables

Chapter 1

Introduction

1.1 Charge transport in iron oxides

Understanding charge transport in transition metal oxides is essential to advancing technical frontiers across diverse fields ranging from biogeochemistry, to renewable energy materials and microelectronics. Hematite is a prominent example. It is a naturally abundant n-type semiconductor [1] and plays a crucial role in redox cycling [2, 3], bioremediation [4] and colloid chemistry [5]. Moreover, the mineral oxide has a visible spectrum band gap and consequently has attracted much interest as a photoanode material for water splitting [6–11].

In a water splitting reaction water is split into gaseous oxygen and hydrogen,

$$2\,H_2O \rightleftharpoons O_2 + 2\,H_2, \tag{1.1}$$

where the generated hydrogen can be used as a clean energy resource with a high energy density [9]. Photocatalytic water splitting is particularly attractive as it involves direct solar-to-chemical energy conversion, in contrast to the current commercial methods for producing hydrogen which rely on steam reforming of methane [7]. In a photoelectrochemical (PEC) cell a photon is absorbed such that an electron is excited into the conduction band, leaving a photo-generated hole in the valance band. The carriers are then separated, and as in conventional water electrolysis oxidation occurs at the anode,

$$2\,OH^- + 2\,h^+ \rightleftharpoons H_2O + \frac{1}{2}O_2, \tag{1.2}$$

and reduction occurs at the cathode,

$$2H_2O + 2e^- \rightleftharpoons H_2 + 2OH^-. \tag{1.3}$$

Generally, the anode is a semiconducting material and the cathode is a metal [6]. There are a number of important properties for a photoanode material including: a visible spectrum band gap, stability in aqueous solution and a high conversion efficiency of photogenerated charge carriers to water splitting products. The latter is related to the charge mobility μ, as well as the lifetime of the photogenerated charges. While hematite is highly abundant and naturally stable, it has low intrinsic mobility and short carrier lifetimes. As such the goal of this thesis is to better understand the nature of charge carriers in hematite, and to investigate the physical mechanisms that lead to the sluggish transport of charge carriers.

At most practical temperatures charge transport in hematite occurs through thermally-activated hopping of polarons, localised lattice distortions that lower the energy of the excess electron or electron hole such that it becomes self-trapped [12]. As a result of the antiferromagnetic structure of hematite, shown in Figure 1.1, electrical conductivity measurements show that conduction is around four orders of magnitude greater in the parallel spin basal plane than in the perpendicular direction [13, 14]. Despite the large number of studies that this material has inspired over the past decades, it is noteworthy that the intrinsic electron and hole mobilities of undoped hematite remain experimentally poorly constrained. Likely as a result of the low intrinsic mobility, challenges in creating pure hematite samples and difficulties in determining the intrinsic carrier concentration, to the best of my knowledge there is no published experimental data for the mobility of undoped hematite. In addition, polaron structures and associated reorganisation energies are not readily experimentally accessible.

Some time ago, Rosso and co-workers [15–18] performed pioneering calculations on small hematite clusters using Hartree-Fock (HF), calculating an inner-sphere reorganisation energy of 1.30 eV for excess electron transfer between two neighbouring iron sites. An approximation of the polarisation of the full bulk crystal

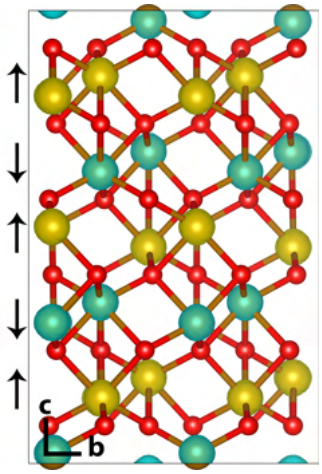

Figure 1.1: Structure of hematite. 2x2x1 supercell spin density with AFM spin orientation indicated by arrows to the left of the figure.

in response to the presence of the electron polaron, referred to as the outer-sphere reorganisation energy, was calculated as 0.17 eV. Their results are consistent with the small electron polaron model, with the excess electron localising over a single iron atom. More recent work by Rosso and co-workers continues to support the small electron polaron [19, 20], and other groups have also utilised cluster models with wavefunction methods with similar results [21].

As a result of the treatment of holes as minority charge carriers, in addition to experimental challenges regarding the production of p-type hematite [22], the electron hole polaron has received less attention than the electron polaron in hematite. Early experimental work showed that the electron hole polaron has a higher activation energy and reorganisation energy than that of the electron polaron, attributing this to hole transport in narrow oxygen bands [23, 24]. However, more recent experimental work on the hematite photoanode observed two different electron hole polaron types: high energy O(2p) holes, and lower energy Fe(3d) holes [25]. Computational studies are also frequently in disagreement, with HF cluster calculations by Rosso and co-workers supporting the Fe(3d) hole [18], while electrostatically embedded HF cluster model calculations from Liao et al. [22] supported the O(2p) hole. Lee et al. [26] performed calculations utilising the Hubbard U correction, a common approach to address the failings of semi-local density functional theory (DFT) functionals in the treatment of strongly correlated Fe(3d) electrons [27], however were unable to

identify any localised hole that was more stable than the delocalised one. Some groups have attempted to compare the possible Fe(3d) or O(2p) holes, with Ansari et al. [28] recently using post Hartree-Fock methods on cluster models to support the O(2p) hole.

It is well known that polaron formation is very sensitive to the DFT functional used, in particular the amount of exact Hartree-Fock Exchange (HFX). HF, used in early calculations of hematite by Rosso and co-workers [15–18], is prone to overbinding of excess charge [29] and may overstabilise small polarons. Moreover, the cluster model that was often used has a number of shortcomings: artificial hydrogen atoms necessary for bond termination, and a lack of consideration of the strain imposed from the full bulk crystal. While some groups have performed bulk DFT+U calculations, these do not produce a uniformly good description of the Fe(3d) and O(2p) centres, band gap and spin population of hematite [30, 31].

With increasing efficiency of computer codes and platforms, it is now possible to study polaron formation in oxide materials using hybrid functionals and large supercells under periodic boundary conditions. In this way some of the complications and uncertainties introduced by cluster models are removed. Vitally, in this work I use hybrid functionals with the fraction of HFX adjusted empirically to reproduce the experimental band gap. While this strategy is rather pragmatic, it is also one of the most effective and accurate to date, allowing new insight into charge carrier structure and dynamics.

1.2 Structure of this thesis

In Chapter 2 I present a brief overview of electron transfer theory, DFT and constrained DFT (CDFT). Computational details regarding the use of the CP2K software package are also presented, including methods used to decrease the computational cost of hybrid DFT calculations such as the auxiliary density matrix method.

While hematite has received the most attention due to its greatest electron mobility [32], other iron oxides and oxyhydroxides may also have similar photoelectrochemical applications and an equal understanding of their polaron structures is

desirable. As such, in Chapter 3 I will present calculations of both the electron and electron hole polaron structures and associated reorganisation energies for a series of iron oxides: hematite ($\alpha-Fe_2O_3$), lepidocrocite ($\gamma-FeOOH$), goethite ($\alpha-FeOOH$) and white rust ($Fe(OH)_2$). This series enables examination of a variety of structural effects including hydration state, hydrogen bonding and the valence of bulk iron.

In Chapter 4 I will discuss in further detail the nature of charge carriers in hematite, and calculate the electron transfer parameters and rates for both electron and electron hole transfer in bulk hematite using CDFT. I will then compare my calculated mobilities to literature calculated and experimental values.

In Chapter 5 I will provide motivation for Hirshfeld based CDFT, and present my implementation of the necessary force terms in the popular DFT package CP2K. I will benchmark my implementation against previous plane-wave CDFT calculations [33] also performed using Hirshfeld partitioning, for both geometry optimisation and molecular dynamics of: electron tunnelling between oxygen defects in MgO [34], and electron self-exchange in aqueous Ru^{2+}-Ru^{3+} [33]. I will also discuss the general reliability of condensed phase CDFT calculations.

In Chapter 6 I will present calculations of the electron and hole polarons at the hematite/liquid water interface, performed in collaboration with Dr. Philipp Schienbein. I will compare the structure and dynamics of charge carriers between bulk hematite and the hematite/liquid water interface, essential for a better understanding of rate-limiting transport processes governing photocatalytic water splitting efficiency at the hematite/water interfaces.

Finally, in Chapter 7 I will conclude the findings of my PhD and provide an outlook on future works.

Chapter 2

Theory

In Chapters 3-4 I will use DFT and CDFT to calculate the electron transfer parameters necessary to calculate the mobility of electrons and electron holes in bulk hematite. As such, in this Chapter I will present an overview of electron transfer theory in Section 2.1, DFT in Section 2.2 and CDFT in Section 2.3. Particular emphasis is placed on the justification for gap-optimised hybrid functionals, the choice of functional throughout this thesis.

I will also briefly discuss some of the computational details regarding the use of the CP2K software package in Section 2.4, including methods used to decrease the significant computational cost of hybrid DFT calculations such as the auxiliary density matrix method.

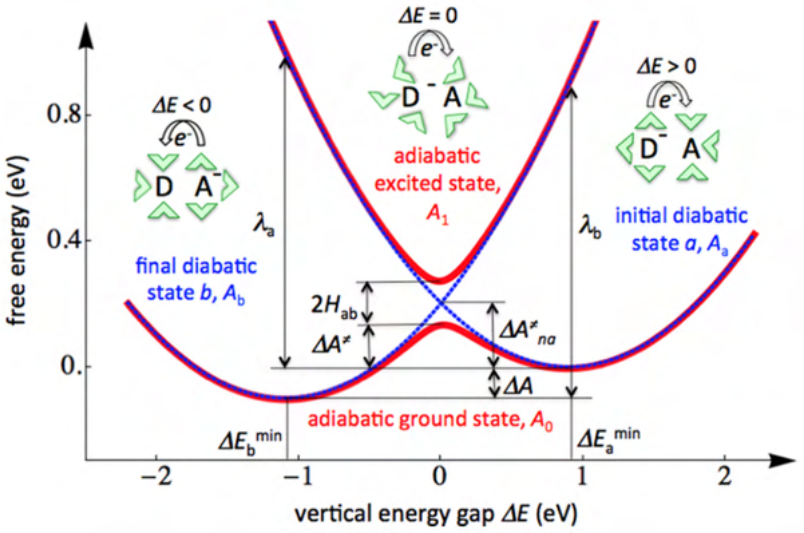

Figure 2.1: Free energy curves for electron transfer between electron donor (D) and acceptor (A). Reprint from Ref [37] with permission.

2.1 Electron transfer theory

For calculation of the required electron transfer (ET) parameters and mobility I adopt the same ET theory as used in previous studies of hematite [18], and in other CDFT calculations [34]. The semi-classical expression for the rate of ET in a donor–acceptor complex derived from transition state theory in the harmonic approximation and Landau–Zener theory has the form [35, 36]

$$k = \kappa_{\mathrm{el}} \nu_{\mathrm{n}} \exp\left(\frac{-\Delta A^{\ddagger}}{k_{\mathrm{B}} T}\right), \tag{2.1}$$

with the electronic transmission coefficient $\kappa_{\mathrm{el}} = 2P_{\mathrm{LZ}}/(1+P_{\mathrm{LZ}})$ where $P_{\mathrm{LZ}} = 1-\exp(-2\pi\gamma)$ is the Landau–Zener transition probability with γ the adiabaticity parameter defined as $2\pi\gamma = \pi^{3/2}\left\langle|H_{\mathrm{ab}}|^2\right\rangle_{\mathrm{TS}}/h\nu_{\mathrm{n}}\sqrt{\lambda k_{\mathrm{B}} T}$. $\left\langle|H_{\mathrm{ab}}|^2\right\rangle_{\mathrm{TS}}$ is the squared electronic coupling averaged over the transition state (TS) configurations, ν_{n} is the effective nuclear frequency along the reaction coordinate, $\Delta A^{\ddagger}$ is the activation free energy, λ is the reorganisation free energy, k_{B} the Boltzmann constant and T the temperature [37]. For an effective nuclear frequency I use the same value as Rosso and co-workers [18], the energy of the highest infra-red active longitudinal optical mode phonon 1.85×10^{13} s^{-1}. I note this is very close to the experimental Fe-O stretch vibration 1.72×10^{13} s^{-1} [38].

The general expression for the activation free energy $\Delta A^{\ddagger}$ valid in the non-adiabatic, adiabatic and intermediate regimes is [39]

$$\Delta A^{\ddagger} = A_0(\Delta E = 0) - A_0(\Delta E = \Delta E_0) \tag{2.2}$$

$$= \Delta A^{\ddagger}_{\mathrm{na}} - \Delta^{\ddagger}, \tag{2.3}$$

where A_0 is the free energy curve for the adiabatic electronic ground state for electron transfer taking the vertical energy gap, ΔE, as reaction coordinate,

$$\Delta E(\mathbf{R}^N) = E_b(\mathbf{R}^N) - E_a(\mathbf{R}^N), \tag{2.4}$$

E_a and E_b are the electronic energies for initial and final diabatic states a and b, $\mathbf{R}^N$ the nuclear configuration, $\Delta E = \Delta E_0$ the position of the minimum of state a and ΔE = 0 the position of the TS. Refer to Figure 2.1.

$\Delta A^{\ddagger}_{\mathrm{na}}$ is the activation free energy on the diabatic electronic states,

$$\Delta A^{\ddagger}_{\mathrm{na}} = \frac{(\lambda + \Delta A)^2}{4\lambda}, \tag{2.5}$$

and $\Delta^{\ddagger}$ is a correction that becomes important when the electronic coupling H_{ab} is large ($|H_{\mathrm{ab}}| > \sim$ 0.01-0.1 λ)

$$\Delta^{\ddagger} = \left\langle |H_{\mathrm{ab}}|^2 \right\rangle^{1/2}_{\mathrm{TS}} - \frac{1}{\lambda} \left\langle |H_{\mathrm{ab}}|^2 \right\rangle_{\Delta E_0,} \tag{2.6}$$

with the assumption that the free energy difference, ΔA, between the initial and final state is zero, which is the case in hematite due to symmetry. Ignoring thermal effects of phonons on electronic coupling and reorganisation free energy, the activation free energy is approximated by the activation energy, $\Delta E^{\ddagger}$,

$$\Delta A^{\ddagger} \approx \Delta E^{\ddagger} = \frac{\lambda}{4} - (H_{\mathrm{ab}} - \frac{H^2_{\mathrm{ab}}}{\lambda}), \tag{2.7}$$

where H_{ab} is taken at the TS and the reorganisation energy λ is calculated as

$$\lambda = 4(E_a(\mathrm{TS}) - E_a(\Delta E_0)), \tag{2.8}$$

where $E_a(\mathrm{TS})$ and $E_a(\Delta E_0)$ are the electronic energies of the initial diabatic state at the transition state and minimum energy nuclear configurations, respectively, calculated using CDFT. Note that for the current system, $E_a(\Delta E_0)$ is virtually identical with the DFT (adiabatic) ground state energy at the minimum energy nuclear configuration.

Charge transport in hematite can be modelled as a succession of hopping between sites, with associated rate constants calculated from Eq. 2.1. As electrical conductivity measurements show that conduction is four orders of magnitude greater in the basal plane than in the perpendicular direction [13, 14], in this thesis I only consider the basal plane mobility. The charge mobility is obtained from the Einstein relation

$$\mu = \frac{eD}{k_{\mathrm{B}}T}. \tag{2.9}$$

Calculation of the diffusion coefficient D can be performed through methods such as kinetic Monte Carlo [40], or by solving a chemical master equation to obtain the time-dependent charge population of each site as by Giannini et al. [41]. The mean squared displacement (MSD) is calculated from the time evolution of the charge population, and following an initial non-linear equilibration period the diffusion coefficient is given by gradient of the MSD [42]

$$D = \frac{1}{2}\lim_{t\to\infty}\frac{d\mathrm{MSD}(t)}{dt}. \tag{2.10}$$

As a result of the lattice symmetry, diffusion is isotropic within the basal plane and therefore the calculated mobility tensor becomes a single value.

Alternatively, the diffusion coefficient can be calculated analytically for a 1D chain model as

$$D = \frac{R^2 ik}{2}, \tag{2.11}$$

for the transfer distance R, site multiplicity i and rate constant k. Rosso and co-workers [15, 18] directly used Equation 2.11 for a 1D model of the 2D basal plane

of hematite, with the site multiplicity i=3 to approximately account for the 3 first nearest neighbours of an iron atom in the 2D plane. Adelstein et al. [43] also used Equation 2.11 for an approximation of the 2D plane, but with i=0.5. My approach moves beyond these approximations, calculating the full mobility tensor in the basal plane.

2.2 Density functional theory

While in principle the Schrödinger equation can be solved to provide the solutions for any quantum mechanical problem, for a system with N nuclei and n electrons the solutions depend on $3(n+N)$ interacting degrees of freedom. Even with the ability to separate the electronic and nuclear degrees of freedom via the Born-Oppenheimer approximation, this is a $3n$ many-body problem that can only be solved for the simplest of systems. As such, further approximations must be made.

In 1964 Hohenberg and Kohn showed that the energy of the ground electronic state is a unique functional of the electron density, laying the foundations for DFT [44]. Further refinement by Kohn and Sham in 1965 [45] provided a general methodology, based on a fictitious system of non-interacting electrons where the ground state density is the same as the real system where the electrons interact. The total energy for this system can be written as

$$E[\rho] = T[\rho] + \int d\mathbf{r} V_{\text{ext}}(\mathbf{r})\rho(\mathbf{r}) + E_H[\rho] + E_{XC}[\rho], \tag{2.12}$$

where $T[\rho]$ is the kinetic energy, V_{ext} is the external potential, $E_H[\rho]$ is the Hartree energy and $E_{XC}[\rho]$ is the exchange correlation energy.

While Equation 2.12 is exact in principle, as a result of the many-body contributions incorporated into the exchange-correlation functional the exact form is unknown. The majority of exchange-correlation functionals are derived starting from the homogeneous electron gas model, where the exchange energy is known analytically and the correlation energy can be fit from higher level theories such as quantum Monte Carlo. The simplest form of the exchange correlation functional is

known as the local density approximation (LDA)

$$E_{XC}^{\mathrm{LDA}}[\rho(r)] = \int \rho(r)\varepsilon_{xc}[\rho(r)]d\mathbf{r}, \tag{2.13}$$

where the exchange-correlation functional depends only on the local value of the density. The most common improvement is known as the generalised gradient approximation (GGA)

$$E_{XC}^{\mathrm{GGA}}[\rho(r)] = \int f(\rho(r), \nabla\rho(r))d\mathbf{r}, \tag{2.14}$$

which includes the first derivative of the electron density, and forms the basis for many functionals including PBE [46]. Generally, GGA functionals vastly outperform LDA functionals in the calculation of total energies and have therefore become the standard choice in most calculations [47].

2.2.1 Optimised hybrid functionals

The electron self interaction error (SIE) is one of the major shortcomings of standard density functionals [48–50], and in the context of this work is particularly problematic due to the spurious delocalisation of localised charges [47, 51]. For example at electron transfer (ET) transition states, where the exact adiabatic ground state is delocalized over the donor and acceptor, the energy is strongly underestimated by standard density functionals due to the wrong scaling of these functionals with fractional electron number, resulting in too low ET barriers and strongly overestimated ET rates [52, 53].

The incorrect scaling of standard density functionals is demonstrated in Figure 2.2. Exact DFT should give a total energy that is piecewise linear with respect to the fractional number of electrons in a system [55], while standard functionals such as those based on the generalised gradient approximation (GGA) display convex behaviour. As mentioned previously HF tends to overlocalise excess charges, due to a concave behaviour [47]. The delocalisation error can therefore be related to the negative deviation of the $E(N)$ curve from the exact linearity condition, while the localisation error is related to positive deviation. The justification for hybrid

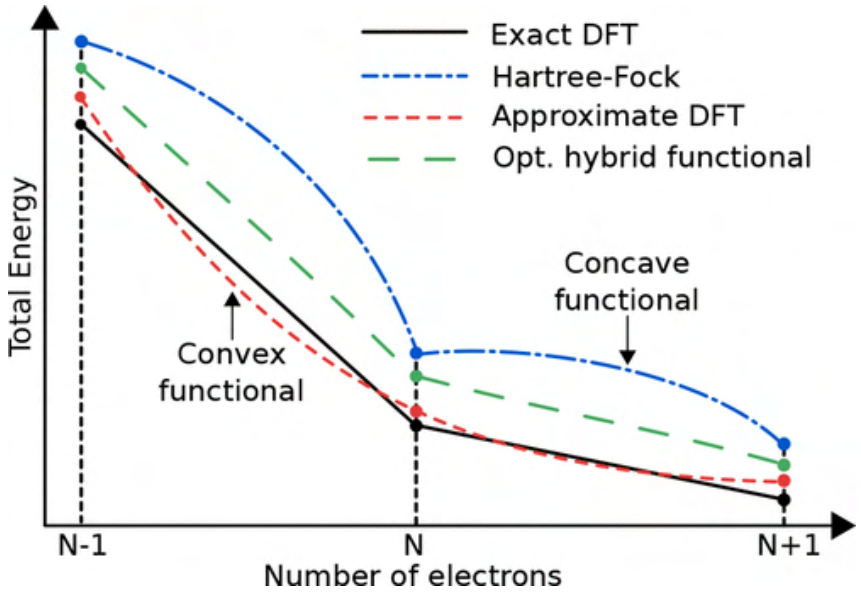

Figure 2.2: Deviation of total energy with number of electrons. Reprint from Ref [54] with CC-BY licence.

functionals is also clear, that by mixing both of these opposing errors a new piecewise linear functional can be obtained.

In this thesis I study a number of different materials, primarily iron oxides and oxyhydroxides, using gap-optimised hybrid functionals. This method of adjusting the fraction of exact exchange to reproduce the experimental band gap is a popular approach for transition metal oxides [31, 56]. The function I use is HSE06 [57],

$$E_{XC}^{\mathrm{HSE}} = aE_X^{\mathrm{HF,\,SR}}(\omega) + (1-a)E_X^{\mathrm{PBE,\,SR}}(\omega) + E_X^{\mathrm{PBE,\,LR}}(\omega) + E_C^{\mathrm{PBE}}, \qquad (2.15)$$

where $E_X^{\mathrm{HF,\,SR}}(\omega)$ is the short-range (SR) HF exchange while $E_X^{\mathrm{PBE,\,SR}}$ and $E_X^{\mathrm{PBE,\,LR}}$ are the short and long range components of the PBE exchange functional. The main contribution of this functional is the introduction of the screening parameter ω, which defines the separation range. For ω=0 HSE reduces to the global hybrid functional PBE0 [58], and for ω=∞ the functional becomes identical to PBE. As such, a finite value of ω is equivalent to extrapolation between these two limits. The original form of HSE used ω=0.15 au = 0.3 $\mathrm{Å}^{-1}$ [59–61], later revised to ω=0.11 au = 0.207 $\mathrm{Å}^{-1}$ in HSE06 [57].

The piecewise linearity of the total energy can be quantified through the gener-

alised Koopmans condition, with nonlinearity

$$\xi = \begin{cases} E(N+1) - E(N) - \varepsilon(N+1) & \text{for electrons} \\ E(N) - E(N-1) - \varepsilon(N) & \text{for holes} \end{cases} \tag{2.16}$$

where $E(N)$ and $\varepsilon(N)$ are the total energy and HOMO energy of a system with N electrons [54, 62]. The values obtained for ξ are summarised in Table 2.1. All functionals with the fraction of exact exchange adjusted to reproduce the experimental band gap have a nonlinearity of no more than 0.04 eV (except for the lepidocrocite electron) while forming localised polarons (except for the goethite electron hole). I note that in addition to tuning the fraction of HFX, there are other methods which aim to restore the linearity of the total energy which are used in Koopmans compliant functionals [63].

2.2.2 Other functionals

Optimised hybrid functionals belong to the 4th rung of Jacobs ladder, a popular classification scheme of DFT functionals proposed by Perdew [65]. Methods belonging to lower rungs are less expensive, and include alternatives to HSE06 such as PBE+U and SCAN [66].

Rather than introducing a certain fraction of exact exchange, in GGA+U an onsite Coulomb interaction is introduced that acts upon a particular orbital [27,67,68]. Similar to the fraction of exact exchange, this introduces a tunable parameter known as the Hubbard U which can be optimised to reproduce the experimental band gap. Previous studies for hematite have shown a surprising variation in the choice of the Hubbard U parameter from 4 V - 6 V [31, 43, 69–72], and that it is difficult to simultaneously reproduce important structural and electronic properties with the same parameter [31]. In addition, it has been shown that certain experimentally known surface terminations of hematite can be reproduced by HSE(12%) but not by PBE+U [30].

A further alternative to either hybrid functionals or GGA+U are the class of meta-GGA functionals, which incorporate a dependency on either the second

Table 2.1: Band gap and hole and electron nonlinearity for each iron oxide, calculated with PBE and HSE DFT functionals. Supercell size for hematite is 221 unless specified otherwise, for lepidocrocite is 613 and for goethite is 316. The experimental band gap for hematite is around 2.2 eV, lepidocrocite around 2.4 eV and goethite around 2.5 eV [64].

	Hematite / eV			Lepidocrocite / eV			Goethite / eV		
	E_g	ξ(h)[a]	ξ(e)[a]	E_g	ξ(h)[a]	ξ(e)[a]	E_g	ξ(h)[a]	ξ(e)[a]
PBE	0.89	-0.01	0.00						
HSE(25%)	3.62	0.11	0.27	3.15	0.03	-0.16	3.33	0.05	-0.02
HSE[b]	2.17	0.03	0.03	2.34	0.02	-0.12	2.52	0.03	-0.04
	2.14 (331)	-0.01 (331)	-0.01 (331)						

[a] Equation 2.16

[b] HSE(12%) for hematite, HSE(18%) for lepidocrocite and goethite

derivative of the electron density or more commonly the kinetic energy density [73]. In particular, the recently developed Strongly Constrained and Appropriately Normed (SCAN) meta-GGA functional [66] has received much interest due to its computational cost comparable to standard GGA functionals, while more accurately predicting important structural and electronic properties [74]. However, it has been demonstrated that SCAN only slightly improves on PBE in regards to the band gap for most materials [75–77] including hematite [78, 79]. In my calculations, I found that SCAN is unable to provide a good description of the charged hematite potential energy surface where it predicts a localised hole and electron polaron energy degenerate with the delocalised charges.

As such, no calculations with either PBE+U or SCAN are presented in this thesis.

2.3 Constrained DFT

Constrained DFT (CDFT) is an established method for generating diabatic electronic states and calculating ET parameters in molecular systems [34, 52, 80–83], although applications to condensed phase/periodic systems remain rare to date. An external potential is added to the Kohn-Sham (KS) Hamiltonian to enforce localisation of the excess electron on the electron donor or acceptor, thereby creating a set of charge localised diabatic states that can be used to obtain the basic quantities of ET theories (reorganisation energy, driving force and electronic coupling). The rationale behind CDFT is that the charge localised diabatic states suffer less from the electron delocalisation error than the adiabatic electronic states in DFT calculations [52].

In Chapter 4 I will take advantage of a recent and very efficient periodic atomic-orbital implementation of CDFT [84] to calculate at hybrid DFT level all the ET parameters required to predict the charge mobility of electrons and holes in bulk hematite. As CDFT is a well established method, with many recent implementations in popular DFT packages [84–88], I choose to only briefly summarise the theory relevant to this thesis.

Charge localised states are constructed by minimising the energy functional

$E[\rho]$ under the condition that the constraint

$$N_c = \int w(\mathbf{r})\rho(\mathbf{r})\mathrm{d}\mathbf{r}, \tag{2.17}$$

is satisfied. $w(\mathbf{r})$ is a weight function that defines how electron density is assigned to atoms or molecules in the constraint region, e.g., electron donor and electron acceptor, and N_c is the constraint value, e.g., the charge of the atoms or molecules or their charge difference. Both remain fixed during CDFT minimisation.

The constrained minimisation is performed by introducing a Lagrangian multiplier V and a new energy functional

$$W[\rho,V] = E[\rho] + V\left(\int w(\mathbf{r})\rho(\mathbf{r})\mathrm{d}\mathbf{r} - N_c\right). \tag{2.18}$$

$W[\rho,V]$ is minimised with respect to ρ for a given V, and V is iteratively adjusted so that the minimised electron density obeys the constraint Eq. 2.17.

There are many different partitioning schemes which can be used to construct the weight function, however in this thesis I use Hirshfeld partitioning of the electron density as this is shown to be a good descriptor for polaron formation in Chapter 3. The Hirshfeld weight function $w(\mathbf{r})$ is constructed from the promolecular atomic densities $\rho_i(\mathbf{r}\text{ - }\mathbf{R}_i) = \rho_i(r)$ where $r = |\mathbf{r}\text{ - }\mathbf{R}_i|$. For a system with N total atoms and a charge difference constraint defined between donor atoms D and acceptor atoms A the weight function has the form

$$w(\mathbf{r}) = \frac{\sum_{i\in D}\rho_i(\mathbf{r}\text{ - }\mathbf{R}_i) - \sum_{i\in A}\rho_i(\mathbf{r}\text{ - }\mathbf{R}_i)}{\sum_j^N \rho_j(\mathbf{r}\text{ - }\mathbf{R}_j)}. \tag{2.19}$$

In Chapter 5 I will discuss the implementation of the necessary force terms for CDFT geometry optimisation and CDFT-MD based on Hirshfeld partitioning of the electron density. However, for calculation of the charge mobility in Chapter 4 the CDFT forces were not needed, as only single point calculations were performed to obtain the energy of the diabatic states and the electronic couplings. The electronic couplings are calculated with the method of Wu and Van Voorhis [52], where the electronic couplings are simply the off diagonal elements of the orthogonal diabatic

Hamiltonian.

2.4 Computational details

Essential for the use of hybrid functionals such as HSE06 for electron rich transition metal oxides in combination with large supercells is the highly efficient implementation in the CP2K code [89, 90]. In particular, the use of integral screening (Section 2.4.1) and the auxiliary density matrix method (ADMM) (Section 2.4.2) significantly improve the speed of HFX calculations [91, 92].

A noteworthy limitation is that at the time of writing, hybrid DFT calculations with k-point sampling is not supported in CP2K. As such, all calculations performed in this thesis are for the Γ-point of the Brillouin zone.

2.4.1 Integral screening

Hartree-Fock is typically quoted as scaling with N^4, where N is the number of basis functions, based on the the calculation of four-center two-electron integrals [93]. In practice, many of these integrals are negligible and through use of the Schwarz inequality an upper bound can be determined allowing for screening and a subsequent decrease in scaling from N^4 to N^2 [94]. A similar procedure can be applied to the density matrix, further decreasing the computational cost to linear scaling [95].

2.4.2 ADMM

While integral screening allows for linear scaling HFX calculations [95], the computational cost can still be significant. The use of a smaller or sparser auxiliary density matrix for the HFX calculation allows for a decrease in computational cost of over an order of magnitude, with negligible decrease in accuracy [92].

The primary basis set used for all calculations in this work is DZVP-MOLOPT-SR-GTH [96], a short range variant of the popular double-ζ basis set optimised for condensed phase calculations. The auxiliary basis set used for ADMM was cpFIT3 for O and H, corresponding to three Gaussian exponents for each valence orbital in addition to polarisation functions from the standard 6-31G** basis sets [92]. For Fe the cFIT11 basis set was used which includes 4s, 3p, 3d and 1f orbitals. I note that

both the primary and auxiliary basis sets were chosen to be consistent with previous work performed on hematite in the Blumberger group [30, 97–100].

2.4.3 Periodic boundary conditions

In periodic boundary conditions the use of global hybrid functionals is problematic due to the integratable singularity [59]. As such, the global hybrid functional PBE0 is typically used with a truncated Coulomb (TC) potential introducing a cutoff radius R_c similar to the range separation parameter ω of HSE06. More commonly, the variant formally known as PBE0-TC-LRC is used where a long-range correction (LRC) based on the PBE exchange hole is added which slightly improves accuracy for short-range cutoffs [91]. I note that a clear benefit of the HSE06 functional is defined range separation parameter ω [57], while there is no defined value of the cutoff radius R_c for PBE0-TC-LRC and as such comparisons between different calculations with this functional must be performed carefully. While I use HSE06 for all iron oxides and oxyhydroxides in thesis, in Chapter 5.2.1.2 I use PBE0-TC-LRC for calculations of oxygen defects in MgO to enable a direct comparison to previous calculations [34, 82].

2.4.4 Dispersion correction

For consistency, in all calculations performed in this thesis I use the Grimme DFT-D3 dispersion correction [101]. This is a post-hoc addition to the DFT calculation at negligible computational cost, which aims to provide a better description of dispersion interactions important in weakly bonded systems. I note however that my calculations for bulk hematite (Chapters 3 and 4) are not dependent on the inclusion of this dispersion correction.

Chapter 3

Polaron structure for a series of iron oxides

While hematite has received the most attention due to its greatest electron mobility [32], other iron oxides and oxyhydroxides may also have similar photoelectrochemical applications and a similar understanding of their polaron structures is desirable. As polaron structures are not readily experimentally accessible [102], the calculations in this Chapter provide valuable insights into the structure of charge carriers important for photocatalytic water splitting. This work has been published in [103].

In this Chapter I present calculations of the both the electron and electron hole polaron structures and associated reorganisation energies for a series of iron oxides: hematite ($\alpha-Fe_2O_3$) in Section 3.2.1, lepidocrocite ($\gamma-$FeOOH) in Section 3.2.2, goethite ($\alpha-$FeOOH) in Section 3.2.3 and white rust ($Fe(OH)_2$) in Section 3.2.4. This series enables a discussion of a variety of structural effects including hydration state, hydrogen bonding and the valence of bulk iron in Section 3.3. In particular, the 2-site delocalisation of the electron polaron is discussed in Section 3.3.1 and the lack of any localised hole polaron in goethite is discussed in Section 3.3.2.

Crystal	a / Å	b / Å	c / Å	α	β	γ
Hematite [105]	5.036	5.036	13.747	90	90	120
Lepidocrocite [106]	3.072	12.516	3.873	90	90	90
Goethite [107]	4.598	9.951	3.018	90	90	90
White rust [108]	3.259	3.259	4.577	90	90	120

Table 3.1: Crystal structure used for all iron oxides and oxyhydroxides studied in this thesis, with reference to experimental sources. I note that to decrease computational cost, no unit cell optimisations were performed.

3.1 Computational setup

As discussed in Chapter 2.2.1, all calculations were performed applying unrestricted DFT with a modified form of the range-separated hybrid functional HSE06 [57], where the percentage of HFX is optimised to reproduce the experimental band gap for each iron oxide [31]. Refer to Table 2.1 for the values used for each iron oxide with reference to the unmodified form of HSE06.

I note that the original publication of this work [103] used a slightly underconverged cutoff of 400 Ry for the real-space integration grid used for representing the electron density, consistent with previous calculations of hematite in the Blumberger group [30, 97–100], which was later increased to 600 Ry in my calculations of charge mobility for bulk hematite [104]. While there is no qualitative change in the results, the more strongly converged cutoff in combination with a more exhaustive examination of polaron structures has resulted in a slight refinement of the original reorganisation energies. I stress however that there is negligible change in bond lengths and spin moment, and that the change in reorganisation energy is within chemical accuracy (<1 kcal/mol). This applies only to calculations for bulk hematite and as such the lepidocrocite, goethite and white rust calculations remain as originally published [103].

Initial coordinates and cell sizes were taken from the experimental crystal structures for hematite [105], lepidocrocite [106], goethite [107] and white rust [108] as shown in Table 3.1. The wavefunction was optimised for the experimental spin ground state [108–111], which are antiferromagnetic.

During the geometry optimisations structures were converged until the residual

forces were smaller than 0.02 eV/Å. Unit cell parameters were fixed, and no symmetry restrictions were applied. For an examination of finite size effects calculations for each iron oxide were performed on at least two different supercell sizes, and to prevent bias of the system no atom was specified as the initial guess for the removal or addition of an electron.

The reorganisation energy λ associated with polaron formation is calculated from Nelsen's four-point method [17, 112]:

$$\lambda = \frac{\lambda_{\mathrm{R}} + \lambda_{\mathrm{O}}}{2}, \tag{3.1}$$

where $\lambda_{\mathrm{O}} = E_{\mathrm{O}}(\mathbf{R}_{\mathrm{R}}) - E_{\mathrm{O}}(\mathbf{R}_{\mathrm{O}})$ is the difference in energies between the oxidised states in their reduced ($E_{\mathrm{O}}(\mathbf{R}_{\mathrm{R}})$) and oxidised geometries ($E_{\mathrm{O}}(\mathbf{R}_{\mathrm{O}})$), and $\lambda_{\mathrm{R}} = E_{\mathrm{R}}(\mathbf{R}_{\mathrm{O}}) - E_{\mathrm{R}}(\mathbf{R}_{\mathrm{R}})$ is the difference in energies between the reduced states in their oxidised ($E_{\mathrm{R}}(\mathbf{R}_{\mathrm{O}})$) and reduced geometries ($E_{\mathrm{R}}(\mathbf{R}_{\mathrm{R}})$).

For comparison of the extent of localisation for the different iron oxides, the change in spin moment was calculated from Hirshfeld analysis [113] for the atoms over which the polaron localises. Another metric that is commonly used to identify polaron formation is the inverse participation ratio (IPR) [114, 115], which quantifies the degree of localisation,

$$\mathrm{IPR}(\psi_n) = \frac{\sum_{i=1}^{N} a_{ni}^4}{(\sum_{i=1}^{N} a_{ni}^2)^2}, \tag{3.2}$$

where

$$\psi_n = \sum_{i=1}^{N} a_{ni}\phi_i, \tag{3.3}$$

is the nth Kohn–Sham eigenvector, N is the number of atomic orbitals and ϕ_i is the ith atomic orbital. The IPR is $1/N$ for completely delocalised states and 1 for fully localised states.

3.2 Results

3.2.1 Hematite $\alpha-Fe_2O_3$

Hematite is a corundum type iron oxide, with a hexagonal structure where each iron(III) atom is bonded to six oxygen atoms. Calculations performed by Pozun et al [31] established that 12% HFX is able to recover the correct band gap and geometry for hematite, and has been used extensively for both bulk hematite as well as the hematite/liquid water interface by the Blumberger group [30, 97–100].

Calculations were performed on three different supercells: a 2x2x1 supercell composed of 120 atoms, a 3x3x1 supercell composed of 270 atoms and the largest 4x4x1 supercell composed of 480 atoms. Neutral geometry optimisation results in a structure in good agreement with experiment [105], where the the two distinct planes of iron atoms that comprise an iron bilayer form average Fe-O bond lengths of 1.94 and 2.12 Å.

3.2.1.1 Hole polaron

Figure 3.1 shows the localisation of an electron hole in the 2x2x1 supercell. When an electron is removed with electronic but no nuclear relaxation (referred to as the vertical state) the hole delocalises over the Highest Occupied Molecular Orbital (HOMO), composed of both O(2p) and Fe(3d) orbitals. The electron hole relaxes from a delocalized band state to a polaron localised on a single iron atom with localisation induced by tetragonal distortion of the 6 surrounding Fe-O bonds. There is a contraction of four equatorial Fe-O bonds, and and a very slight expansion of two axial Fe-O bonds. These changes in bond lengths are in response to the removal of electron density in the equatorial plane, more specifically in response to removal of an electron from a $d_{x^2-y^2}$ orbital. Similar tetragonal elongation is observed in the Jahn-Teller effect of high spin d^4 complexes [116], however this is not strictly Jahn-Teller distortion as there are there are two distinct groups of Fe-O bond lengths of 1.94 and 2.12 Å in the neutral geometry due to the iron bilayer [105]. A schematic energy level diagram is shown in Figure 3.2.

As a result of the two distinct groups of Fe-O bonds, the contraction is asymmet-

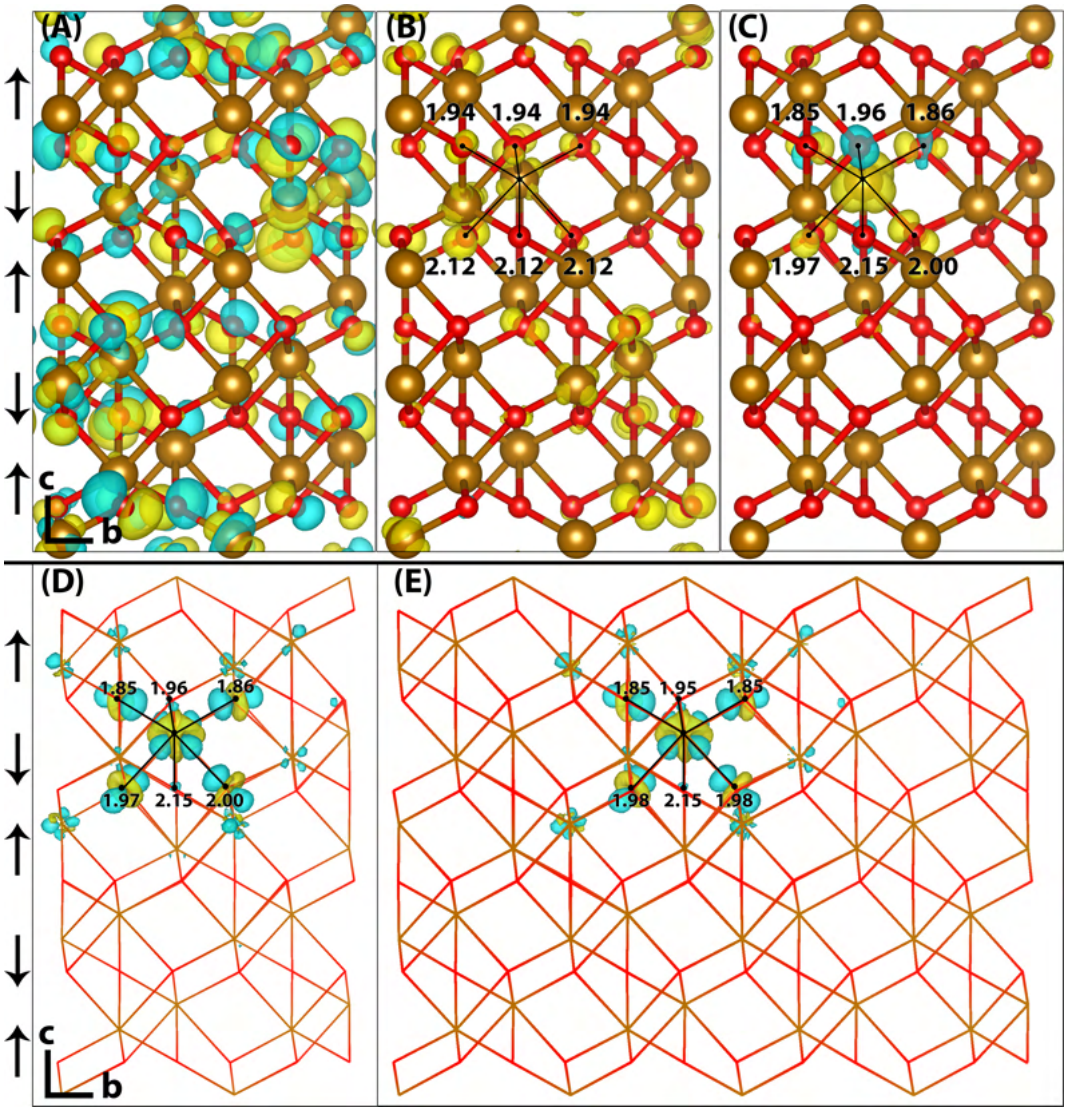

Figure 3.1: Electron hole in hematite: (A) Sum of 5-fold degenerate HOMO (isosurface 0.02 e/Bohr^3). (B) Excess spin density for the vertical state (isosurface 0.002 e/Bohr^3) and (C) the relaxed state (isosurface 0.005 e/Bohr^3). (D-E) Excess electron density for the relaxed state (isosurface 0.005 e/Bohr^3). The electron hole relaxes onto a single iron site, with positive increase in density indicated by yellow isosurfaces and negative by blue isosurfaces. Bond lengths between the iron site and bonded oxygen atoms are shown in Angstrom. Calculations are for the bulk hematite 2x2x1 supercell (A-D) and for the 4x4x1 supercell (E), viewed perpendicular to the AFM layers. AFM spin orientation is indicated by arrows to the left of the figure. The standard 'ball-and-stick model' is shown for images A-C, while the 'wireframe' model is used to highlight the polaron structure in images D-E.

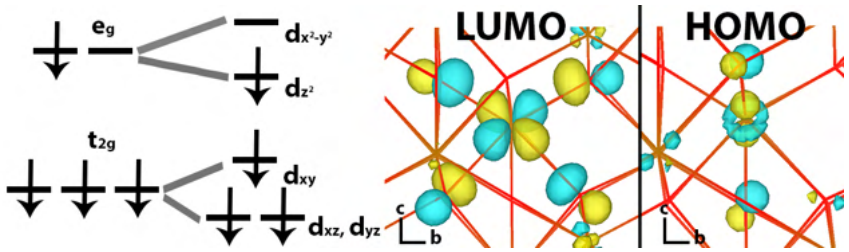

Figure 3.2: Schematic energy level diagram for the hole polaron in hematite. Ignoring the asymmetry of the Fe-bilayer, the structure of the hole polaron in hematite can be understood from the Jahn-Teller effect of high spin d4 octahedral metal complexes. The DFT LUMO and HOMO on the ground state hole polaron geometry are shown for comparison.

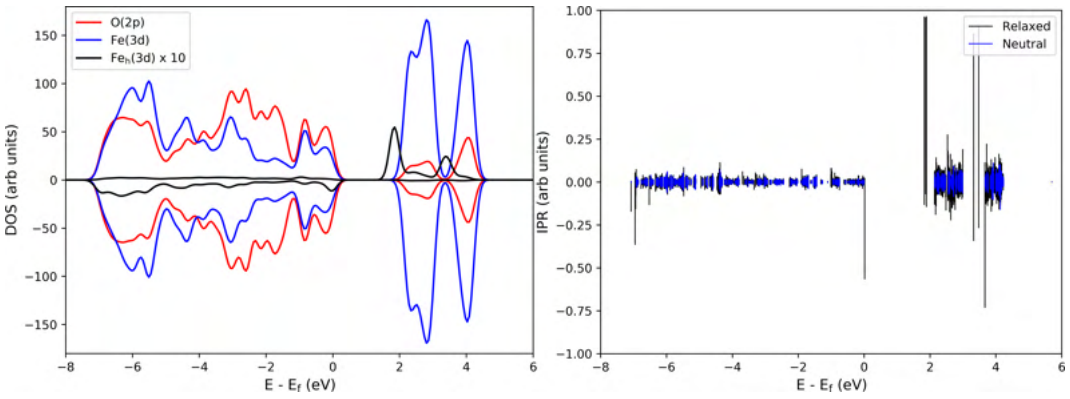

Figure 3.3: Electron hole in hematite: (A) projected density of states for the hole ground state and (B) IPR demonstrating the localisation of the electron hole polaron onto a single iron atom.

ric. For example in the 2x2x1 supercell the longer Fe-O bonds (2.12 Å) experience a slightly stronger contraction, -0.080 Å in comparison to -0.050 for the shorter Fe-O bonds (1.94 Å). Figure 3.1 also compares the polaron structure for the 2x2x1 and 4x4x1 supercells, with only a slight decrease in bond lengths from -0.065 Å to -0.070 Å.

The reorganisation energy calculated from Equation 3.1 for the 2x2x1 supercell is 0.33 eV, increasing to 0.34 eV for the 3x3x1 and 4x4x1 supercells. The formation of polaronic states within the band gap has been verified from the density of states and the IPR (Figure 3.3).

Tables 3.2-3.3 show the spin moment and charge over the iron atom that the polaron localises for the 2x2x1 supercell. It can be seen that the change in spin moment from Hirshfeld partitioning (+0.66 from neutral to hole ground state) is a

	Neutral GS	Charged	Charged GS	Neutral
Electron hole	-3.95	-3.93	-3.29 (+0.66)	-3.87
Excess electron	-3.95	-3.90	-3.72 (+0.23)	-3.96

Table 3.2: Spin localisation in bulk hematite. Spin of the iron atom that the electron hole localises on, and the average spin of the two iron atoms that the excess electron localises on. 'Neutral GS' refers to neutral ground state, 'Charged' to neutral ground state geometry with the excess charge added, 'Charged GS' to charged ground state and 'Neutral' to neutral state on the charged ground state geometry. Shown in brackets is the change from Neutral GS to Charged GS. Calculations are shown for the 2x2x1 supercell with Hirshfeld partitioning of the electron density.

	Neutral GS	Charged	Charged GS	Neutral
Electron hole				
Hirshfeld	0.44	0.45	0.43 (-0.01)	0.41
Hirshfeld-I	0.56	0.57	0.55 (-0.01)	0.54
DDEC6	1.56	1.57	1.62 (+0.06)	1.65
Bader	1.76	1.76	1.80 (+0.04)	1.80
Excess electron				
Hirshfeld	0.44	0.41	0.36 (-0.08)	0.45
Hirshfeld-I	0.56	0.57	0.46 (-0.10)	0.56
DDEC6	1.56	1.52	1.38 (-0.18)	1.51
Bader	1.76	1.72	1.61 (-0.15)	1.73

Table 3.3: Charge localisation in bulk hematite. Charge of the iron atom that the electron hole localises on, and the average charge of the two iron atoms that the excess electron localises on. 'Neutral GS' refers to neutral ground state, 'Charged' to neutral ground state geometry with the excess charge added, 'Charged GS' to charged ground state and 'Neutral' to neutral state on the charged ground state geometry. Shown in brackets is the change from Neutral GS to Charged GS. Calculations are shown for the 2x2x1 supercell.

good indicator of polaron formation while the change in charge (-0.01) is not. The change in electron density in Figure 3.1 shows a clear decrease in electron density at the $d_{x^2-y^2}$ orbital, and therefore the change in spin moment without a change in charge is a result of (paired) electron rearrangement. While it is surprising that the hole polaron localises with no change in charge, I note that Adelstein et al. [43] and Ansari et al. [28] have also observed this effect. Notably, Ansari et al. [28] found that even for MP2 and CCSD calculations on small hematite clusters only the change in spin moment is a useful indicator of polaron formation.

To investigate whether the lack of charge localisation is an artefact of Hirshfeld

partitioning, I also include in Table 3.3 the charges calculated with a number of more sophisticated partitioning schemes: Hirshfeld-I [117] as implemented in CP2K, DDEC6 as developed by Manz and co-workers [118] and Bader partitioning as implemented by Henkelman and co-workers [119]. Hirshfeld-I improves upon the use of isolated neutral densities in standard Hirshfeld partitioning, using an iterative refinement scheme for the promolecular density. DDEC6 and Bader partitioning are both post-processing charge partitioning schemes, which take an electron density .cube file as an input and generate charges either through a method similar to Hirshfeld-I (DDEC6) or by searching for zero flux surfaces (Bader). I note that a key advantage to DDEC6 over the Henkelman implementation of Bader partitioning is the inclusion of reference core charge densities, necessary for pseudopotential codes such as CP2K where the .cube file only includes valence electron density. Consistent with other studies I find that Hirshfeld-I predicts slightly larger charges than standard Hirshfeld partitioning [120], and both DDEC6 and Bader both predict significantly larger charges [121, 122]. For the electron hole there is a slight decrease in charge from the neutral ground state to the charged ground state with standard Hirshfeld partitioning (-0.01) and Hirshfeld-I (-0.01), which becomes slightly positive with DDEC (+0.06) and Bader partitioning (+0.04). This suggests that while the more sophisticated partitioning schemes support some degree of charge localisation of the electron hole, this is still significantly less than would typically be expected for polaron formation. As previously mentioned these results for hematite are consistent with calculations performed by other groups [28, 43], and given the focus on spin moments rather than charges for other transition metal oxide materials [54, 123, 124] it would be interesting to confirm whether this is a general trend.

3.2.1.2 Electron polaron

The vertical state for an excess electron is shown in Figure 3.4 and is consistent with the Lowest Unoccupied Molecular Orbital (LUMO), composed of Fe(3d) t_{2g} character. Upon nuclear relaxation the excess electron delocalises over two iron atoms, with equal changes in spin moment of +0.23 (see Table 3.2). Due to the delocalisation over two iron sites and the subsequent smaller change in bond lengths,

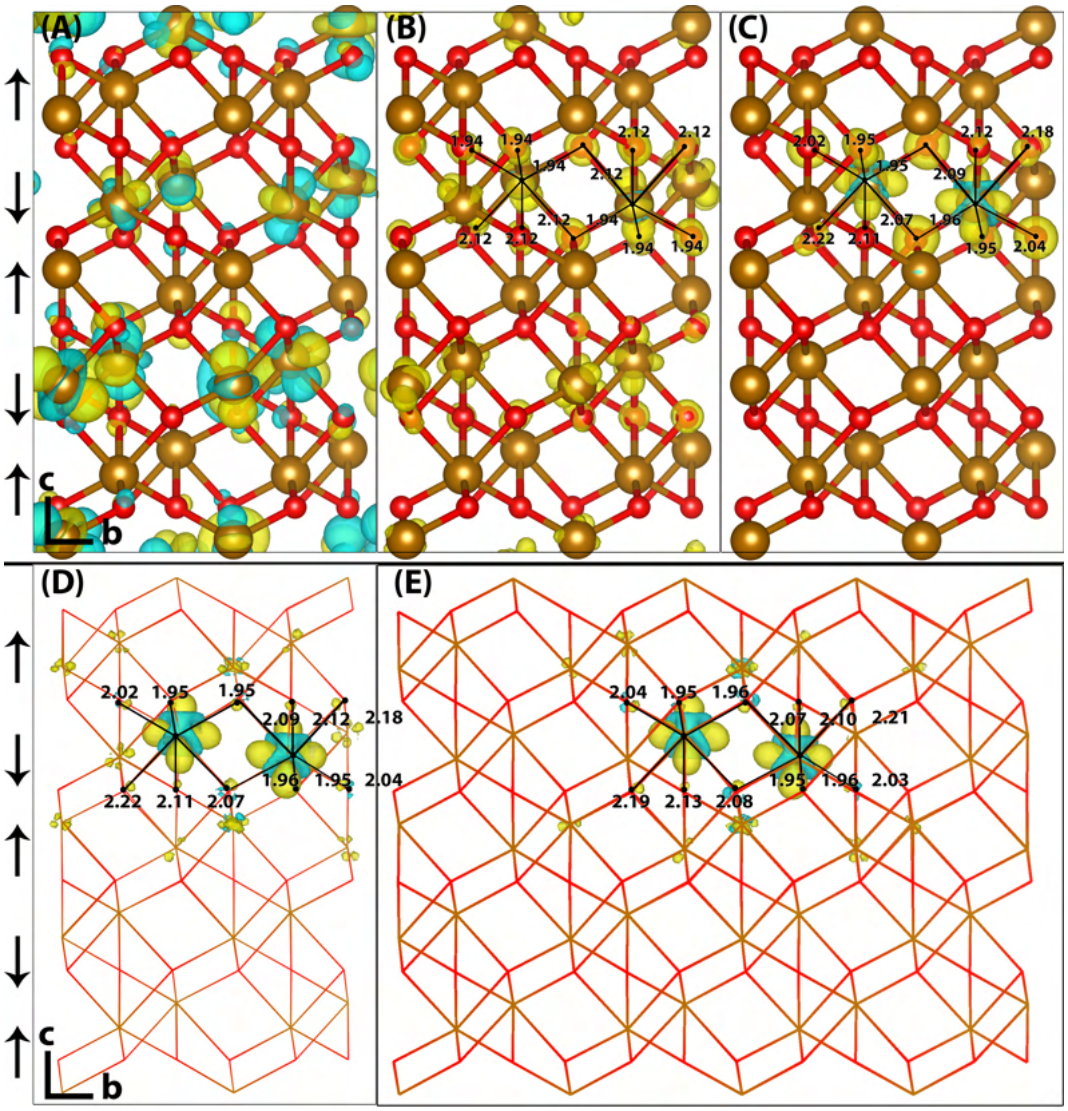

Figure 3.4: Excess electron in hematite: (A) LUMO (isosurface 0.02 e/Bohr^3), (B) excess spin density for the vertical state (isosurface 0.002 e/Bohr^3) and (C) the relaxed state (isosurface 0.005 e/Bohr^3). (D-E) excess electron density for the relaxed state (isosurface 0.005 e/Bohr^3). The excess electron delocalises over two iron sites, with a positive increase in density indicated by yellow isosurfaces and negative by blue isosurfaces. Bond lengths between the iron site and bonded oxygen atoms are shown in Angstrom. Calculations are for the bulk hematite 2x2x1 supercell (A-D) and for the 4x4x1 supercell (E), viewed perpendicular to the AFM layers. AFM spin orientation is indicated by arrows to the left of the figure. The standard 'ball-and-stick model' is shown for images A-C, while the 'wireframe' model is used to highlight the polaron structure in images D-E.

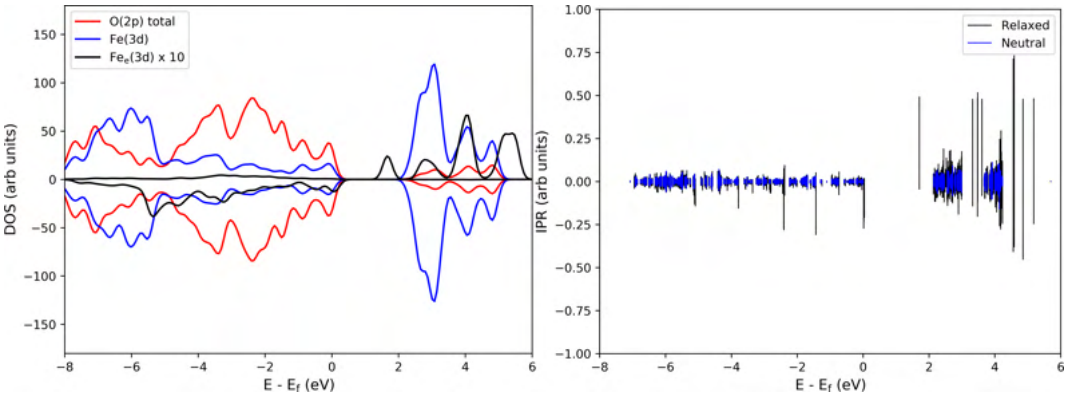

Figure 3.5: Excess electron in hematite: (A) Density of states and (B) IPR demonstrating the delocalisation of the electron polaron across two iron atom.

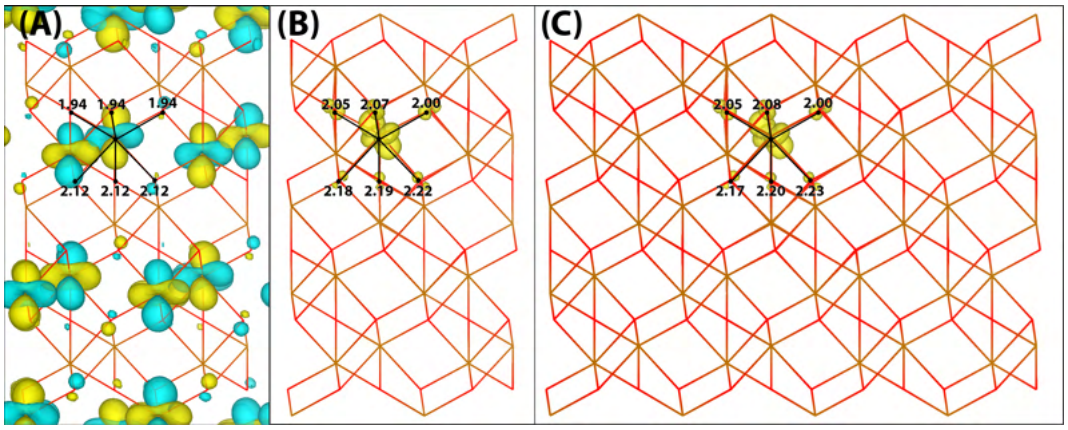

Figure 3.6: Excess electron in hematite. (A) LUMO (isosurface 0.02 e/Bohr^3), (B) excess spin density (isosurface 0.005 e/Bohr^3) for the relaxed state in a 2x2x1 supercell and (C) a 4x4x1 supercell. Increasing the percentage of HFX from 12% to 50% causes localisation of the electron polaron on a single iron atom. Bond lengths between the iron site and bonded oxygen atoms are shown in Angstrom, and the density plots are shown in the 'wireframe' model to highlight the polaron structure.

the reorganisation energy is reduced from 0.34 eV for the hole polaron to 0.23 eV for the electron polaron. There is no qualitative change in polaron structure as the supercell size is increased from 2x2x1 to 4x4x1, indicating that this is not an artefact of finite size effects.

An important consideration is that the percentage of HFX has been optimised to reproduce the experimental band gap, and that this may alter the (de)localisation behaviour. Therefore for completeness, the localisation patterns at 25% and 50% HFX have also been investigated for the excess electron. The value of 25% HFX is

notable as this is the value used in unmodified HSE06. At this value the change in spin density reduces significantly over one of the iron sites, resulting in a change in spin moment of 0.50 and 0.09 over the two iron sites. At 50% HFX, shown in Figure 3.6, the electron is fully localised with a change in spin moment of 0.68 and 0.02. Interestingly, even for the fully localised electron polaron there is still some interaction between the iron atom and the nearest neighbour as indicated by the asymmetry of the increase in Fe-O bond lengths in Figure 3.6 and the alignment of the spin density such that it maximises overlap with a nearest neighbour. This is very similar to calculations performed by Adelstein et al. [43] with DFT+U, where they observed even for an electron polaron that appeared fully localised from spin moment analysis (0.51, 0.01) there was still some degree of delocalisation of the electron polaron over two iron atoms as identified from shorter Fe-Fe bond lengths.

At 25% and 50% HFX the band gap rises to 3.6 eV and 6.4 eV respectively, and therefore it can be understood that only at unphysically high values of HFX does the electron localise over a single iron site as previously understood in the literature. It has been confirmed that in restarting the HSE06(50%) structure with 12% HFX there is immediate electronic relaxation to the 2-site delocalised structure, even without geometry re-optimisation.

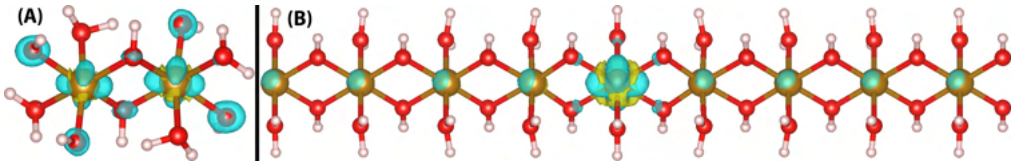

Figure 3.7: Excess spin density for an excess electron in (A) a hematite dimer cluster and (B) a 1D hematite chain. Calculations for the hematite dimer cluster are performed with HSE06(12%), where the excess electron is delocalised over both iron atoms. In the 1D hematite chain the excess electron is delocalised across the whole chain with HSE06(12%), and therefore the excess spin density is shown for pure HF where there is localisation on a single iron atom. The same isosurface colouring scheme is used as for bulk hematite (Figures 3.1 and 3.4), however due to the localisation across the opposite spin channel the colours are inverted.

3.2.1.3 Hematite cluster and 1D chain

Much of the current understanding of small polaron formation in hematite originates from pioneering cluster and 1D chain model calculations [15–18]. As such, for completeness I briefly discuss calculations performed for these systems.

Figure 3.7 shows the excess spin density for an excess electron in a hematite dimer cluster calculated with HSE06(12%) and for a 1D hematite chain calculated with pure HF. I calculated the reorganisation energy for the same hematite dimer cluster as used by Rosso and co-workers [18], finding a reorganisation energy of 0.48 eV which is more than twice that found in my calculations for bulk hematite of 0.23 eV. As such, the larger reorganisation energy found in earlier calculations of hematite can be attributed to the presence of artificial hydrogen atoms necessary for termination of the dimer cluster, and the neglect of strain effects present in the bulk crystal.

For the 1D hematite chain I found that with HSE06(12%) there is no localised electron or hole polaron. With pure HF, shown in Figure 3.7, the band gap is severely overestimated as 16 eV compared to the experimental band gap of 2.2 eV. As such, I do not provide any further results for either the 1D hematite chain or the hematite dimer cluster.

3.2.2 Lepidocrocite γ−FeOOH

Lepidocrocite is a naturally occurring metastable iron oxyhydroxide, of interest for charge transport processes in addition to proton transfer as a consequence of

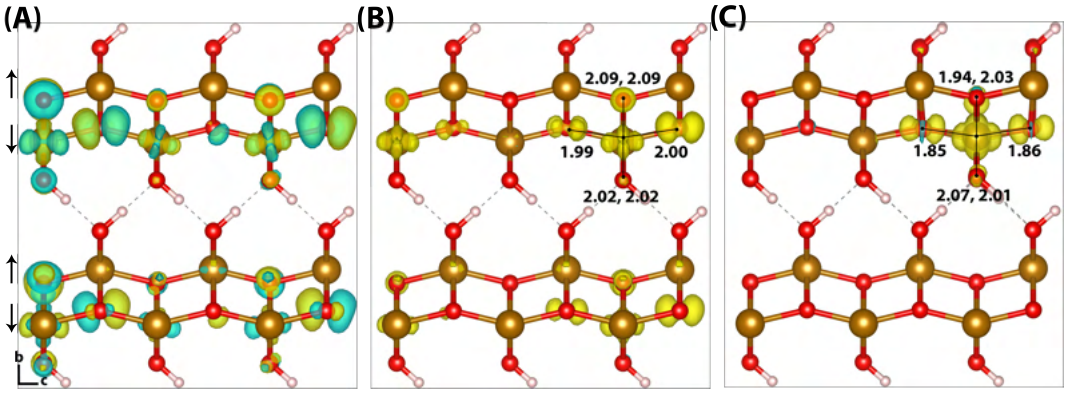

Figure 3.8: Excess hole in lepidocrocite: (A) HOMO with asymmetry caused by degeneracy (<0.06 meV) between the top four levels, (B) difference in spin density for vertical state, and (C) the relaxed state. The excess hole relaxes onto a single iron site, where the positive increase in spin density is indicated by yellow isosurfaces and negative by blue isosurfaces. Bond lengths between the iron site and coordinated oxygen atoms are shown in Angstrom. Data for a 313 supercell of bulk lepidocrocite calculated with HSE06(18%), viewed perpendicular to the AFM layers along the (100) plane. AFM spin orientation is indicated by arrows to the left of the figure.

its layered graphite-like structure [125]. The band gap of lepidocrocite calculated using HSE06(12%) is 1.4 eV, outside of the experimental range 2.1-2.4 eV [64, 126]. The band gap for goethite is similarly underestimated, and as lepidocrocite and goethite are polymorphs it would be desirable to use the same value of HFX for both systems. Therefore the percentage of HFX is increased to 18%, in order to reproduce the experimental band gaps for both lepidocrocite and goethite. The two supercell sizes used are 313 (144 atoms) and 613 (288 atoms), increased in the direction of localisation only in order to examine finite size effects.

There are a few notable differences between the experimental and neutral optimised geometries, a result of the experimental uncertainty regarding the hydrogen atom positions. Two space groups have been proposed for lepidocrocite: the centrosymmetric group Cmcm where the hydrogen atoms occupy two positions either side of the Fe-O bond, and the Cmc2 group where the hydrogen atoms occupy only one of these positions (Figure 3.8). A number of experimental papers quote either space group [106, 110, 127], however it is clear that only the Cmc2 space group used in this work results in a physically meaningful structure. The Pmc2 space group structure containing alternating hydrogen bonds in adjacent layers is found to be

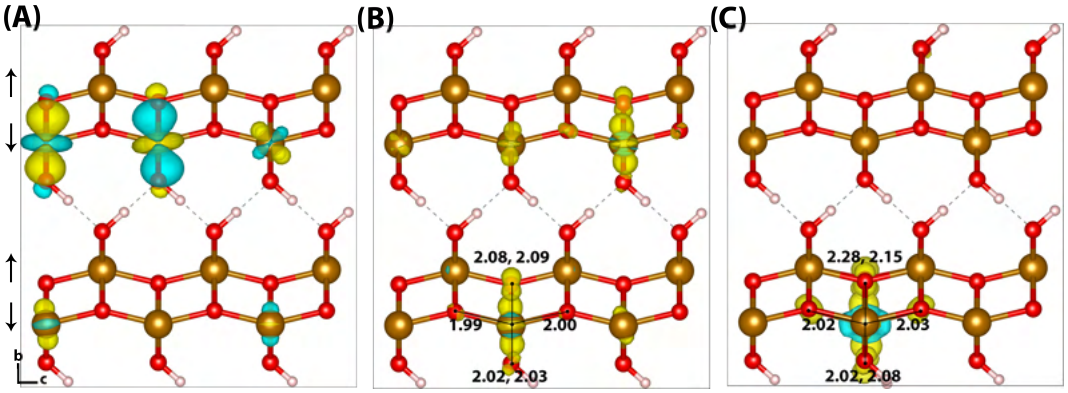

Figure 3.9: Excess electron in lepidocrocite: (A) LUMO with asymmetry caused by degeneracy (<5 meV) between the top four levels. (B) Difference in spin density for vertical state, and (C) the relaxed state. The excess electron relaxes onto two parallel spin iron sites, with a positive increase in spin density caused by the addition of an anti-symmetric spin. An alternative view of the lepidocrocite electron polaron structure can be found in Figure 3.10, highlighting the 2-site delocalisation. Data for a 613 supercell of bulk lepidocrocite calculated with HSE06(18%).

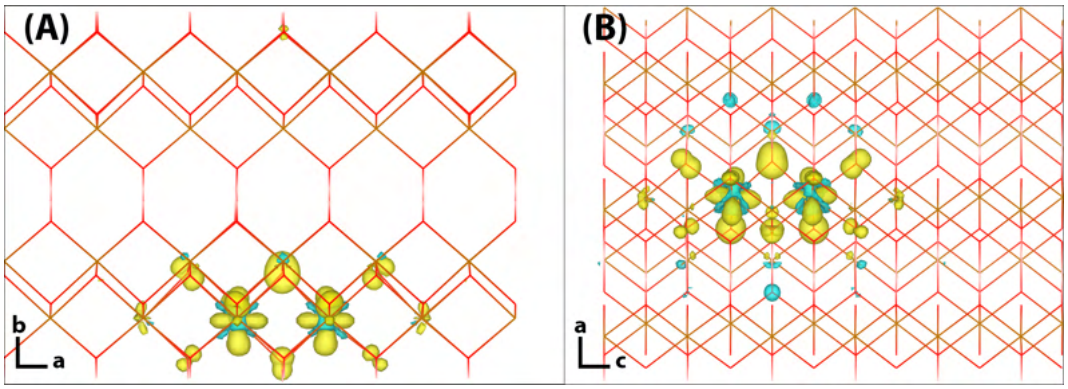

Figure 3.10: Excess electron 2-site delocalised structure: difference in spin density for (A) lepidocrocite and (B) goethite. The 'wireframe' model is used to highlight the polaron structure.

energy-degenerate with Cmc2, as different layers will be weakly correlated. This may be a cause for the experimental identification of the space group as Cmcm, as the hydrogen atoms may occupy either space group with no energy penalty. These results are in good agreement with other computational studies [125].

3.2.2.1 Hole polaron

Similar to hematite, the HOMO of lepidocrocite (Figure 3.8) is composed of a mixture of O(2p) and Fe(3d) orbitals. Following nuclear relaxation a single iron

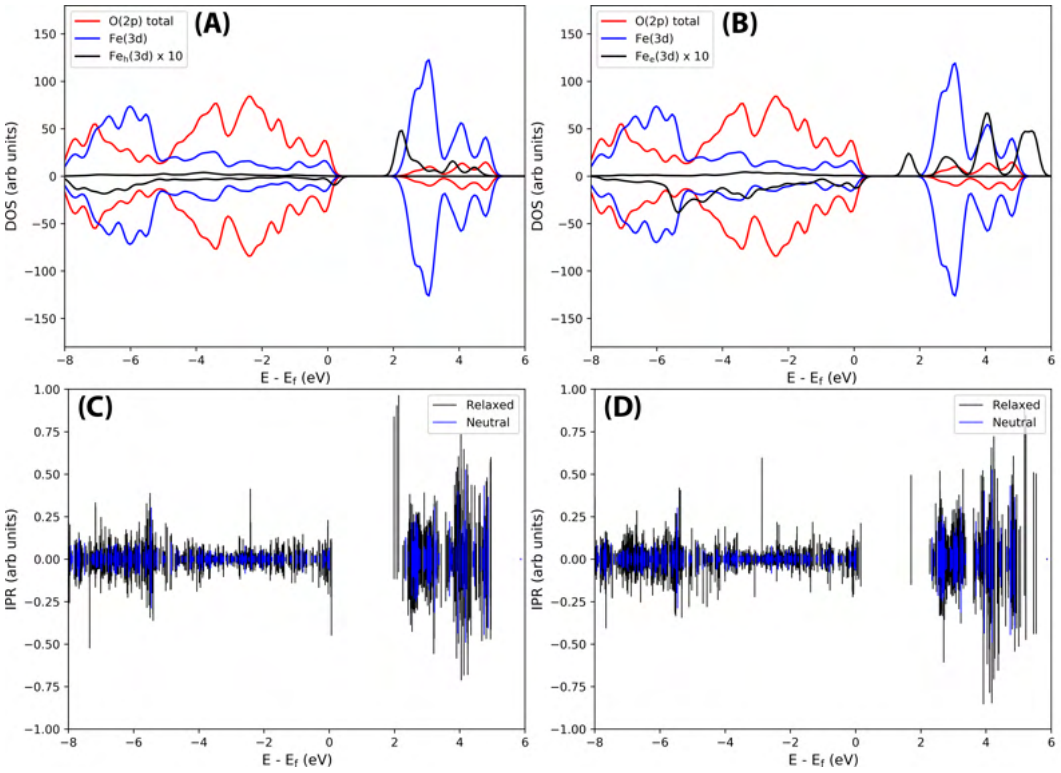

Figure 3.11: Excess electron and electron hole in lepidocrocite: (A-B) density of states and (C-D) IPR demonstrating the 1-site localised hole polaron (A, C) and the 2-site delocalised electron polaron.

site emerges with a change in spin moment of 0.64, very similar to that found for the hematite 2x2x1 supercell of 0.66. With the larger 613 supercell the change in spin moment increases slightly to 0.65, and the average change in bond lengths increases from -0.073 Å to -0.080 Å. The largest change in bond lengths of -0.14 Å is experienced by the two non-hydrogen bonded oxygen atoms of the same spin layer ($\pm$ c direction), and the smallest of +0.02 Å is over the hydrogen bonded oxygen atoms (-b direction). This increase in bond lengths is a consequence of the iron atom moving in the opposite direction to maximise orbital overlap with the in-plane oxygen atoms, as well as the inflexible hydrogen bonding network which leads to a low change in spin moment and bond lengths over the hydrogen bonded oxygen atoms. As such while the average change in bond lengths and spin moment over the iron atom is similar to the hematite 3x3x1 supercell, the reorganisation energy of 0.59 eV is much greater. The density of states and IPR for both the hole and electron polaron can be found in Figure 3.11.

3.2.2.2 Electron polaron

Upon nuclear relaxation the excess electron in the 313 supercell localises across a single parallel spin layer composed of three iron atoms, a result of interaction with periodic self-images of the excess charge. The larger 613 supercell (Figure 3.9) is able to avoid these finite size effects with twice the number of atoms in this direction, leading to a two iron site delocalisation with equal changes in spin moment of 0.24 and an average change in bond lengths of +0.063 Å and +0.064 Å. The reorganisation energy for the 613 supercell is 0.36 eV, higher than that for hematite of 0.23 eV.

3.2.3 Goethite $\alpha-$FeOOH

Goethite is the most thermodynamically stable iron oxyhydroxide, isostructural with diaspore. In contrast to lepidocrocite, goethite is not a layered structure but one based upon oxo-bridged double-chains of iron octahedra. While experimental band gap data ranges from 2.1-2.5 eV, recent experiments favour 2.5 eV [64] which is reproduced with HSE06(18%). In addition to the same HFX value, the same supercell sizes are also constructed from experimental data to ensure fair comparison of the two polymorphs lepidocrocite and goethite [107].

The neutral geometry optimisation of goethite has been challenging, as the structure becomes easily distorted along the Fe-O chains. The O-H bond lengths from x-ray diffraction experiments are calculated as 0.88 Å, while the HSE06(18%) optimised value is 0.99 Å. This is in agreement with other computational studies [128], and is attributed to lack of sensitivity to hydrogen atoms present in x-ray diffraction experiments. It has been confirmed that the hydrogen bonding distances are not strongly dependent on the inclusion of the D3 dispersion correction.

3.2.3.1 Hole polaron

The HOMO of goethite in Figure 3.12 is consistent with the other iron oxides studied, a mixture of O(2p) and Fe(3d) orbitals. The structure of the hole polaron however is very different, remaining fully delocalised even after nuclear relaxation. The density of states and IPR for both the hole and electron polaron can be found in Figure 3.15.

In order to verify the delocalisation of the electron hole a number of different

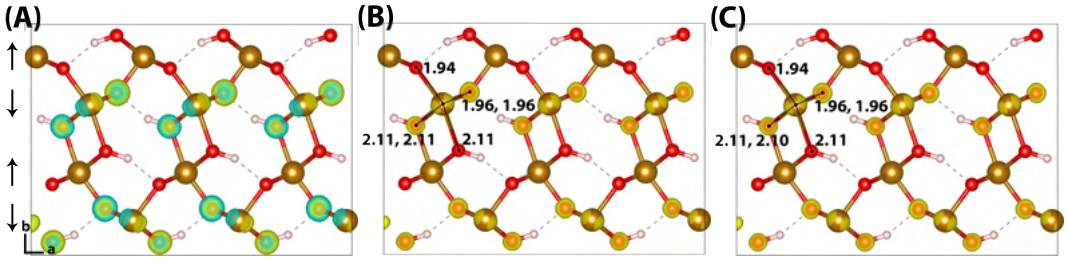

Figure 3.12: Excess hole in goethite: (A) HOMO, (B) difference in spin density for vertical state, and (C) the relaxed state. The excess hole in goethite does not localise, with no qualitative difference between the vertical and relaxed states. Bond lengths between the iron site and coordinated oxygen atoms are shown in Angstrom. Data for a 313 supercell of bulk goethite calculated with HSE06(18%), viewed perpendicular to the AFM layers along the (001) plane. AFM spin orientation is indicated by arrows to the left of the figure.

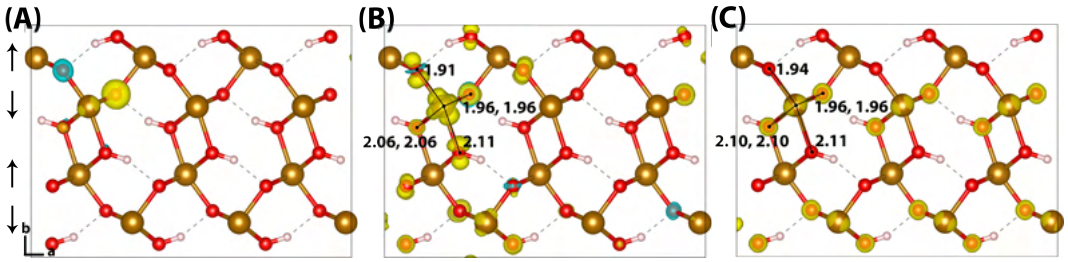

Figure 3.13: Excess hole in goethite: (A) Difference in spin density for the relaxed excess hole calculated at 50% HFX, (B) restarted at 18% HFX and (C) re-optimised at 18% HFX.

initial conditions have been tested, including restarting the optimisation from a localised state from a higher percentage of HFX. While increasing the amount of HFX to 50% does not lead to spontaneous localisation for the 316 supercell, for the smaller 313 supercell the excess hole delocalises across a row of oxygen atoms. A similar dependency on the fraction of HFX has been observed in hematite and lepidocrocite, as well as in the literature [28], where at high values of HFX the hole localises over oxygen atoms. Figure 3.13 shows how restarting this localised state at 18% HFX immediately results in delocalisation of the excess hole. Following nuclear relaxation, the hole fully delocalises across the parallel spin layers with a relaxation energy of ~1 eV.

A final confirmation of the lack of excess hole localisation in goethite can be found from an analysis of the local force constants, where in the vertical state each unique oxygen atom is displaced up to 5% (around 0.1 Å) along the corresponding

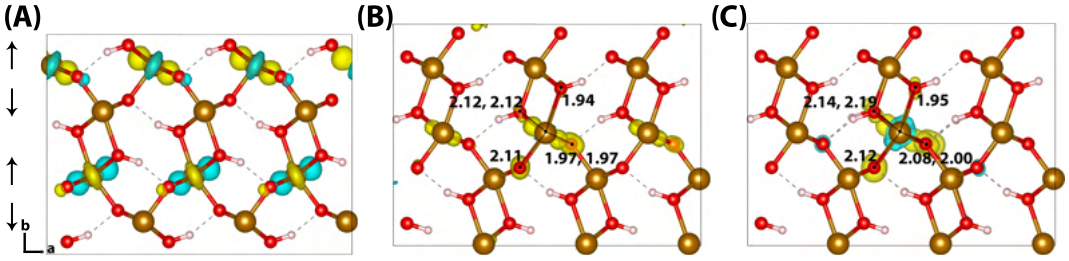

Figure 3.14: Excess electron in goethite: (A) LUMO, (B) difference in spin density for vertical state, and (C) the relaxed state. The excess electron relaxes onto two parallel spin iron sites, with a positive increase in spin density caused by the addition of an anti-symmetric spin. (B) and (C) are shown centred on the localisation atoms, as these are on the supercell edge. An alternative view of the goethite electron polaron structure can be found in Figure 3.10, highlighting the 2-site delocalisation. Data for a 316 supercell of bulk goethite calculated with HSE06(18%).

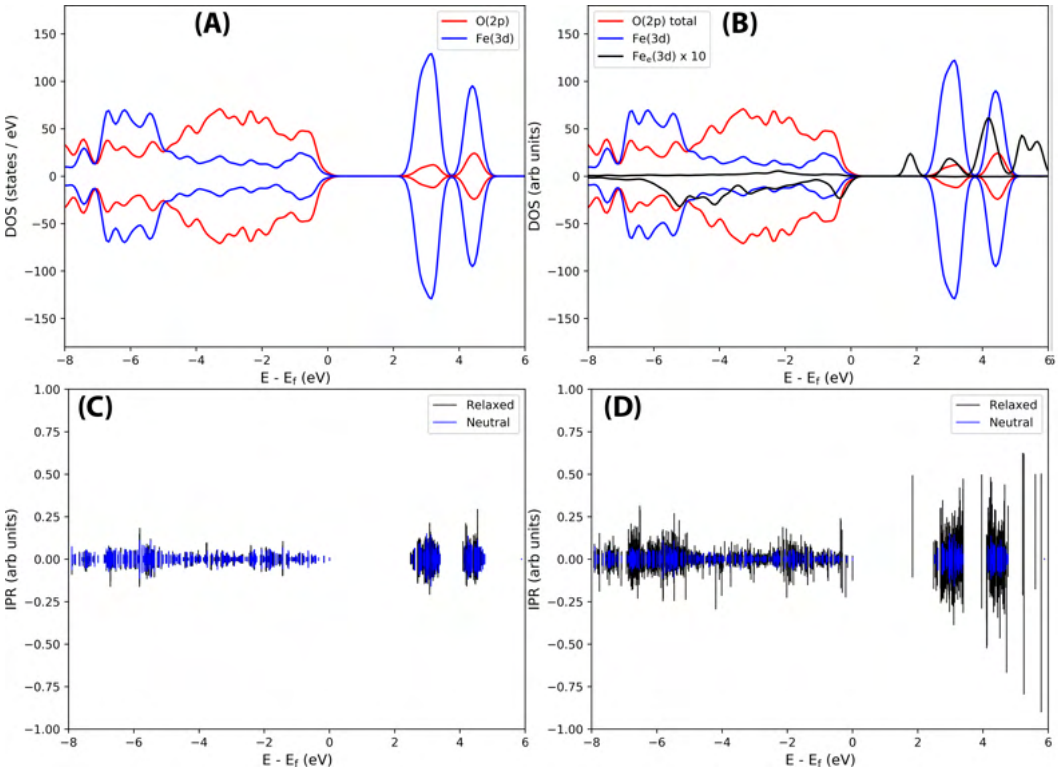

Figure 3.15: Excess electron and electron hole in goethite: (A-B) Density of states and (C-D) IPR demonstrating the fully delocalised hole (A, C) and the 2-site delocalised electron polaron.

Fe-O bond. For both the neutral and excess hole state these fit well to the harmonic approximation $\Delta E = \frac{1}{2}k\Delta r^2$ (RMSE <2 meV). This is is strong contrast to lepidocrocite, where for the excess hole there is a decrease in energy for displacement along the Fe-O-Fe bonds up to 0.06 Å (same spin plane) and 0.02 Å (out of spin

plane). The attractive region present in lepidocrocite demonstrates how the decrease in local bond lengths leads to a lower energy localised state, which does not occur in goethite. A final result from this force constant analysis is that there is no decrease in energy for displacement of the Fe-OH bonds in lepidocrocite, suggesting that the energy penalty for disrupting the hydrogen bonding framework is greater than the decrease in energy from polaron formation. This appears to be the case in both lepidocrocite and goethite. See Section 3.3.2 for further discussion.

3.2.3.2 Electron polaron

Similar to lepidocrocite, the localisation of the excess electron in the larger 316 supercell results in a two iron site delocalisation with changes in spin moment of 0.25 and 0.26 (Figure 3.14). The subsequent reorganisation energy is 0.35 eV, very similar to that of lepidocrocite at 0.36 eV.

3.2.4 White rust $Fe(OH)_2$

White rust is a highly unstable iron oxyhydroxide, isostructural with brucite, with a layered structure of iron atoms in octahedral coordination with oxygen separated by non-bonded hydrogen atoms [129–132]. In contrast to previous oxides all iron atoms have formal oxidation state (II) rather than (III) in the neutral state, and therefore only the electron hole polaron is considered. To the best of the authors knowledge this is the first work to perform DFT calculations of white rust, although Rosso and co-workers have studied white rust with a similar methodology to their cluster calculations of hematite using HF [133].

While the crystal structure and antiferromagnetic spin pattern have been determined experimentally [108], the band gap has not been verified. From the white colour it should be expected that the band gap exceeds 3.1 eV (violet light), and an experimental study using ultraviolet–visible spectroscopy indicates that the band gap may be around 3.5 eV [134]. As such white rust has been examined using a range of HFX values, including 29% which reproduces the band gap of 3.5 eV. An alternative approach would be to minimise the non-linearity (see Chapter 2.2.1), however this appears to favour low fractions of HFX with a band gap lower than 3.1

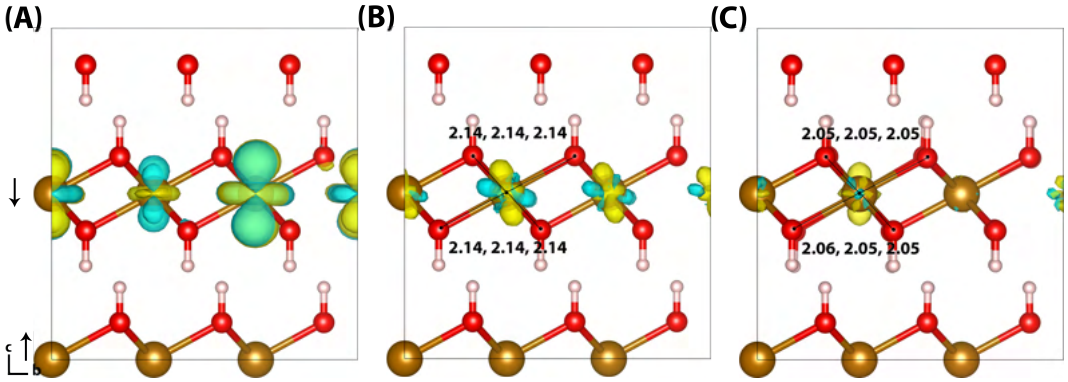

Figure 3.16: Excess hole in white rust: (A) HOMO, with asymmetry caused by degeneracy (<0.5 meV) between the top two HOMO levels. (B) Difference in spin density for vertical state, and (C) the relaxed state. The excess hole relaxes onto a single iron site, where the positive increase in spin density is indicated by yellow isosurfaces and negative by blue isosurfaces. Bond lengths between the iron site and coordinated oxygen atoms are shown in Angstrom. Data for a 3x3x2 supercell of bulk white rust calculated with HSE06(29%), viewed perpendicular to the AFM layers along the (100) plane. AFM spin orientation is indicated by arrows to the left of the figure.

Fraction of HFX	18%	25%	29%	50%
Band gap / eV	2.5	3.1	3.5	5.4
Non-linearity / eV	0.03	0.12	0.18	1.25
Reorganisation energy / eV	0.08	0.38	0.47	0.63
Change in Fe-O bond lengths / Å	-0.035, -0.019	-0.090	-0.090	-0.097
Change in Fe spin moment	0.24, 0.17	0.59	0.62	0.72

Table 3.4: Band gap, non-linearity, reorganisation energy, changes in bond lengths and spin moments for localisation of an excess electron in white rust as a function of the fraction of HFX. With HSE06(14%) the excess electron is fully delocalised with a band gap of 2.1 eV, while with HSE06(18%) the excess electron is delocalised over 2 iron atoms and from HSE06(25%) to HSE06(50%) the excess electron is localised on a single iron atom.

eV. For completeness, I provide a summary of all white rust calculations including the band gap and non-linearity in Table 3.4.

The mixed spin state and non-bonded interactions make white rust an extremely challenging system to model, requiring very tight wavefunction convergence and a robust conjugate gradient optimiser. As such, the available system size is limited to a 90 atom 3x3x2 supercell. A careful optimisation for the neutral state results in a structure in good agreement with experiment [108], the only notable difference with the increase in O-H bond lengths from 0.90 Å to 0.96 Å.

Figure 3.16 shows the HOMO of white rust, composed of entirely Fe(3d) character. At 14% HFX, with a band gap of 2.1 eV, the excess hole fully delocalises. As the percentage of HFX increases the excess hole converges to the single iron site localisation, where Figure 3.16 shows the results at 29% HFX with a change in spin moment of 0.62 and a reorganisation energy of 0.47 eV. I note that the residual forces could only be converged to 0.08 eV/Å, which may be exacerbated by the small supercell size where only up the nearest neighbour iron atoms are included.

3.3 Discussion

A comparison of all results for hematite, lepidocrocite, goethite and white rust can be found in Table 3.5.

In the original publication of this work [103] I stated that as calculations become unfeasible for supercells larger than the ones used here, the computed reorganisation energies need to be corrected for finite size effects. However, by including the results for the 4x4x1 hematite supercell used in later calculations of the electron and hole mobility [104] it would appear that the finite size effects were overestimated. The reorganisation energy can be partitioned into inner-sphere λ_i and outer-sphere λ_o contributions: the inner-sphere accounts for the local changes in bond lengths, while the outer-sphere accounts for the polarisation of the surrounding environment [135]:

$$\lambda = \lambda_i + \lambda_o. \tag{3.4}$$

It is the outer-sphere reorganisation energy contribution that generally needs to be corrected for finite size effects. My later work [104] (see Chapter 4) indicated that the inner sphere reorganisation energy is actually overestimated in the smaller supercells, which compensates for the reduced outer-sphere reorganisation energy. As such, in assuming that only the outer-sphere reorganisation will change and extrapolating to infinity with only two supercell sizes I had obtained an overestimate of the reorganisation energy. For lepidocrocite and goethite I have only calculated a single reorganisation energy for the excess electron, and therefore in this thesis I have chosen to not to include any finite size corrections.

Table 3.5: Reorganisation energies, changes and in bond lengths and spin moments for the localisation of an excess hole and electron in each iron oxide. For the electron polaron, the average spin moment and change in bond lengths for the two iron sites where the polaron delocalises are shown. The values for hematite have been updated from my original publication [103], with the planewave cutoff increased from 400 to 600 Ry and with the values taken from an average of more than 5 geometry optimisations for each supercell [104].

	Hematite	Lepidocrocite	Goethite	White rust
Excess hole				
Reorganisation energy λ^a / eV	0.33 (2x2x1)	0.51 (3x1x3)		
	0.34 (3x3x1)	0.59 (6x1x3)		0.47 (3x3x2)
	0.34 (4x4x1)			
Average change Fe-O bond lengths / Å	-0.065 (2x2x1)	-0.073 (3x1x3)		
	-0.068 (3x3x1)	-0.080 (6x1x3)		-0.090 (3x3x2)
	-0.070 (4x4x1)			
Change in Fe spin moment	0.66 (2x2x1)	0.64 (3x1x3)		
	0.66 (3x3x1)	0.65 (6x1x3)		0.62 (3x3x2)
	0.66 (4x4x1)			
Excess electron				
Reorganisation energy λ^a / eV	0.21 (2x2x1)			
	0.23 (4x4x1)	0.36 (6x1x3)	0.35 (3x1x6)	
Average change Fe-O bond lengths / Å	0.025 (2x2x1)			
	0.026 (4x4x1)	0.063 (6x1x3)	0.050 (3x1x6)	
Change in Fe spin moment	0.23 (2x2x1)			
	0.23 (4x4x1)	0.24 (6x1x3)	0.25 (3x1x6)	

[a] Equation 3.1

Another concern can be image charges, that due to the use of periodic boundary conditions the localised polaron will interact with periodic self-images. This effect can be seen in the use of smaller supercells for lepidocrocite and goethite, where the excess electron fully delocalises across a row of iron atoms rather than forming the 2-site delocalised structure found in larger supercells. There are a number of methodologies to attempt to correct for the effect of image charges [34,136], however in the context of this work I assume that the use of large supercells for materials with large dielectric constants results in a negligible contribution of image charges to the reorganisation energy. As seen in Table 3.5, there is a negligible change in reorganisation energy with increasing supercell size for hematite which supports this assumption.

3.3.1 Electron two site delocalisation.

Much of the current understanding of electron small polaron formation originates from pioneering cluster model calculations supporting the view that the excess electron is localised on a single iron atom [15–18]. Twenty years on, such calculations can now be carried out for extended supercells in periodic boundary conditions, which removes some of the well-known deficiencies of cluster models: the presence of artificial hydrogen atoms necessary for termination of the dimer cluster; and the neglect of strain effects present in the bulk crystal. Moreover, HF, which tends to overbind excess electrons is replaced with a hybrid functional with empirically tuned exact exchange. The result is a significantly smaller reorganisation energy to the extent that the excess electron localises over two rather than one iron atom. Similar cluster model calculations in this work using HSE06(12%) give reorganisation energies more than twice as large as in the bulk, indicating that it is mostly the missing steric strain in the cluster models that cause the large reorganisation energies.

Viewed from the perspective of electron transfer theory (i.e. in the diabatic representation of electronic states), my results mean that the electronic coupling matrix element, H_{ab}, between between Fe(II) and Fe(III) is greater than half of the reorganisation energy, which leads to instability of the diabatic states such that the transition state of electron transfer theory becomes the minimum [39]. See Chapter

4 for further discussion.

I note that there are some conceptual similarities between this 2-site delocalised electron polaron and both bipolarons [137, 138] and molecular polarons [139], where two excess electrons may overcome their Coulombic repulsion to form a 2-site localised structure or a dynamically coupled complex. In Chapter 4 I will demonstrate that the 2-site delocalised electron polaron hops through the hematite crystal as a single unit, similar to the process of bipolaron diffusion [137].

3.3.2 Hole delocalisation in goethite.

One of the most surprising findings of this work is that the excess hole does not localise in goethite. The density of states for the two polymorphs lepidocrocite and goethite are very similar, and so this is not due to a lack of available states for localisation but instead a consequence of the extended hydrogen bonding framework.

In lepidocrocite there are two distinct oxygen environments: the hematite-like oxygen atoms within the layers with four O-Fe bonds, and the hydrogen bonded oxygen atoms linking the layers with two O-Fe bonds and two hydrogen bonds. It is found that these hematite-like oxygen atoms undergo a larger change in bond lengths and spin moment in comparison to the hydrogen bonded oxygen atoms, due to the inflexible hydrogen bonding framework in the charged state. Indeed, from force constant analysis there is no decrease in energy for displacement of the Fe-OH bonds in the vertical state for lepidocrocite. This effect is more pronounced in goethite, where every oxygen atom is hydrogen bonded. The energy gained from polaron formation in hematite is around 8 kcal/mol, on the same energy scale as that of a hydrogen bond (5-10 kcal/mol). Therefore in goethite there are two competing effects: the lowering of energy due to polaron formation, and the energy cost of disrupting/breaking the extended hydrogen bonding framework. As such, the excess hole remains delocalised in goethite.

This hole delocalisation in goethite should be experimentally testable, as the band conduction of holes would have a temperature dependence that does not fit the classical small polaronic hopping model. I note that in a similar semiconductor with photocatalytic water splitting applications, bismuth vanadate $BiVO_4$, standard gap-

optimised hybrid functionals also predict a delocalised hole polaron. For bismuth vanadate experimental resistivity measurements do show a temperature dependence consistent with the small polaron model [140, 141], however without optimisation to reproduce the experimental band gap it is unclear what value of HFX should be chosen [142, 143].

3.3.3 Trend of reorganisation energy.

Before I discuss reorganisation energy of the oxides in more detail, I note that they are much smaller (~0.5 eV) than for transition metal ions in aqueous solution [144–146] (about 2-3 eV). The difference is most likely related to the contrast between the steric strain of the crystal environment compared to the higher degrees of conformational freedom among solvating water molecules as well as the significantly higher optical dielectric constant of the iron oxides compared to water.

While it has been found that the extent of excess charge localisation is similar across the studied iron oxides, there are differences in the reorganisation energies that merit discussion. Hematite has consistently the lowest reorganisation energy and average change in bond lengths of the iron oxides, a consequence of the local bonding environment. In hematite there are two distinct bond types around each iron atom, splitting the iron bilayer into two distinct planes of iron atoms leading to Fe-O bonds of 1.94 Å and 2.12 Å. This allows the excess hole or electron a large amount of freedom to localise, which is not present in lepidocrocite or goethite where the localisation is much more heavily restricted by the local bonding environment. This can be seen clearly by comparing the localisation of the excess hole between hematite, where the hole is able to localise freely over the oxygen atoms, to lepidocrocite where the hole is forced largely onto only two oxygen atoms. As such, lepidocrocite experiences a much larger hole reorganisation energy than hematite. White rust is likely an intermediate between these two extremes, having less freedom than hematite but more then lepidocrocite as the excess hole is forced to localise isotropically over the six bonded oxygen atoms due to the hexagonal crystal symmetry.

Due to the reduced extent of localisation the reorganisation energy for the excess electron is lower, by around a factor of 1.5. The same trend appears as for the

excess hole, where the same change in spin moment is experienced but with a greater reorganisation energy for lepidocrocite and also now for goethite. The localisation of the excess electron in hematite across two iron sites within the same Fe-bilayer is the cause for the smaller change in bond lengths, as in order to maximise the orbital overlap between the iron atoms two of the longer Fe-O bonds contract (see Figure 3.4). The reorganisation energies for lepidocrocite and goethite differs only by 0.01 eV, and the smaller change in bond lengths for goethite is likely a result of the interaction of the different spin layers. While the excess electron in goethite localises partially over the oxygen atoms of the opposing spin layer, this occurs with no change in bond length as this would have a high energy penalty. In lepidocrocite the LUMO has greater overlap with the oxygen atoms in the $\pm$b direction, and while the oxygen atoms in this direction are more strongly associated with the opposing spin layer there is still some contribution from this spin layer which allows for a change in bond lengths. This is similar to hematite where the oxygen atoms are shared by both spin layers. These findings are consistent with experimental observations, where hematite has the highest electron mobility among the examined iron oxides.

3.4 Conclusions

In this Chapter both the electron and hole polaron structures and associated reorganisation energies have been calculated for a series of bulk iron oxides. While the polaron structures and extent of charge localisation remains largely consistent across the studied iron oxides, except for the hole in goethite, hematite has consistently the lowest reorganisation energy in agreement with its experimental electron mobility.

The calculation of hole polaron structures reveals a lack of localisation of the excess hole for goethite, as a result of the energy penalty for disrupting the extended hydrogen bonding framework. This may make this material a promising candidate as a hole conducting material. It would be of interest to verify this prediction, such as by temperature dependent hole conductivity measurements.

Electron polaron calculations consistently produce a two iron site delocalisation of the excess electron for all studied iron oxides and oxyhydroxides, contrary to

previous understanding of the electron polaron in these materials. Calculations from hematite dimer clusters and 1D hematite chains have been demonstrated to lead to an overestimate of the reorganisation energy and an overbinding of the excess electron to a single iron site, and the importance of reproducing both the experimental structural and electronic properties (i.e. band gap) has been emphasised. To the best of my knowledge these are the most sophisticated calculations performed for these materials, and as such these results should provide new and valuable insights into the structure of charge carriers of importance for photocatalytic water splitting .

Chapter 4

Electron and hole mobilities in bulk hematite

In this Chapter I calculate the electron and electron hole diffusivity and mobility for bulk hematite. In particular, I would like to understand how the 2-site delocalised electron moves along the lattice and how its mobility differs from that of the electron hole. To this end, I calculate the electron transfer parameters and rates for electron and electron hole transfer in hematite using CDFT. These calculations will provide valuable insights into the mechanisms that lead to the sluggish transport of charge carriers in hematite, relevant for increasing photocatalytic water splitting efficiency. This work has been published in [104].

In this Chapter I present results for the electron hole polaron in Section 4.2.1 and for the electron polaron in Section 4.2.2. Charge mobilities are calculated in Section 4.2.3, with an examination of finite size effects in 4.2.4 and a discussion of the results in Section 4.3.

4.1 Computational setup

As discussed in Chapter 3, the Hirshfeld spin moment of iron atoms is a suitable descriptor for polaronic states. The spin moment changes from -3.95 to -3.29 for the electron hole, and -3.95 to -3.72 for each of the two Fe atoms over which the electron polaron is delocalized.

For electron hole transfer between two Fe atoms, Fe_A and Fe_B, I define the initial (final) ET state as the spin constrained CDFT state with the spin moment on Fe_A (Fe_B) constrained to -3.29. For electron transfer between two 2-site delocalized Fe pairs, $(Fe_1\text{-}Fe_2)_A$ and $(Fe_3\text{-}Fe_4)_B$ I define the initial (final) ET state as the spin constrained CDFT state with the spin moment on each of the two iron atoms Fe_1 and Fe_2 (Fe_3 and Fe_4) constrained to -3.72. These constraints ensure that for any geometry (including transition state geometry) diabatic states are obtained that resemble very closely the DFT electronic ground state of the electron hole or electron polaron in the global minimum energy structure.

Other definitions of the spin constraint would be possible. For instance, one could include the first shell oxygen atoms but I found that their spin moment is rather small and their inclusion in the constraint is not beneficial. Moreover, one could constrain the spin density difference between donor and acceptor groups which is a common choice in CDFT calculations [34]. However, I found that a single absolute spin constraint on the Fe atoms in question is the most suitable choice in the present case.

To setup the CDFT calculations, first the polaron is localised on each of the desired iron atoms, typically by offsetting the local Fe-O bond lengths to encourage polaron formation at this location. After geometry optimisation to form the charged DFT ground state, linear interpolation is performed to create the transition state geometries. These transition state geometries are then used to calculate both the electronic couplings and reorganisation energies (Eq. 2.8) using CDFT. This is performed by constraining the spin moment of the iron atoms to the spin moment of the charged ground state given above, thus generating the diabatic electronic states at the transition state geometry.

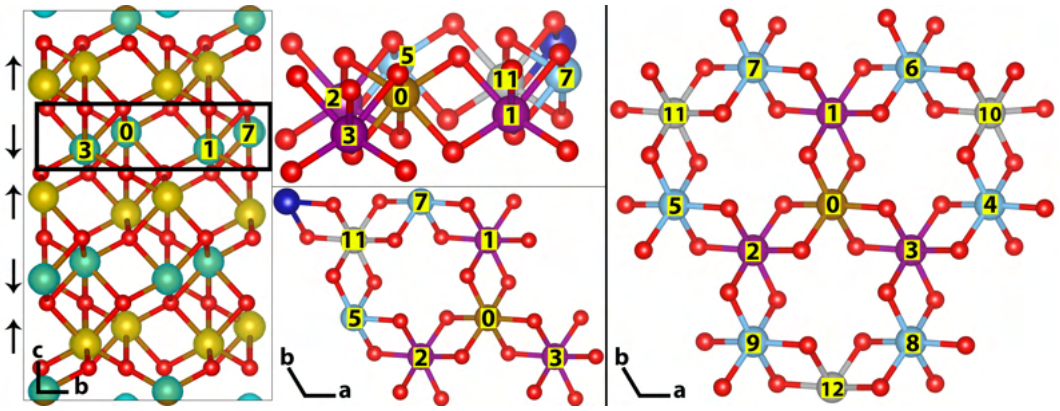

Figure 4.1: Structure of hematite 2D mobility plane. 2x2x1 supercell spin density (left), with a single AFM plane highlighted in black shown colour coded by distance from a central iron atom 0 (middle). A single AFM plane truncated to third nearest neighbours is shown (right). There are three first nearest neighbours (purple) numbered 1-3 at a distance of 2.97 Å, six second nearest neighbours (blue) numbered 4-9 at 5.04 Å and three third nearest neighbours (grey) numbered 10-12 at 5.87 Å.

4.2 Results

4.2.1 Hole polaron

The electron hole polaron, shown in Figure 4.2 is mainly localised on a single Fe atom and to a lesser extent on 1st shell oxygen atoms. As explored in Chapter 3, the hole polaron is stabilised by an octahedral distortion of the iron-oxygen bonds. There is a contraction of four equatorial Fe-O bonds, and and a very slight expansion of two axial Fe-O bonds. These changes in bond lengths are in response to the removal of electron density in the equatorial plane, more specifically in response to removal of an electron from a $d_{x^2-y^2}$ orbital. Importantly, this tetragonally distorted structure can be realised in three equivalent ways giving exactly the same electronic energy. Each of these symmetry-related structures can be transformed into one another by lattice vibrations. To the best of my knowledge this three-fold degeneracy of the hole polaron has not been previously explored, and its effect on the mobility has not been investigated.

Due to the 3-fold structural degeneracy, there are 3 x 3 = 9 possible transition state structures for hole transfer between an Fe atom and any of the three nearest neighbours. However, only 5 of these 9 combinations are unique featuring different

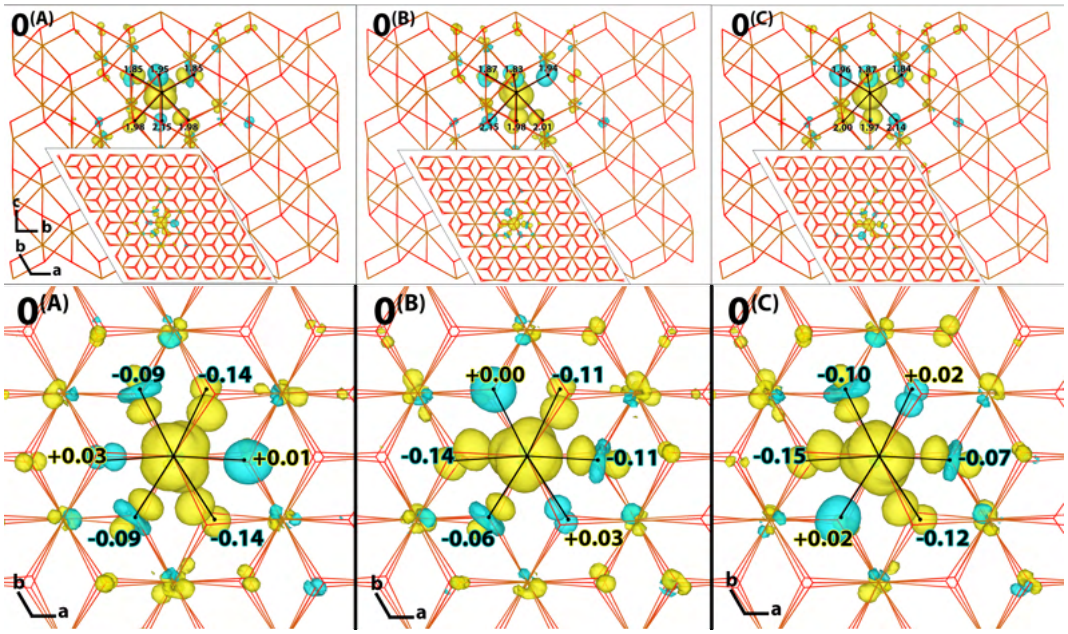

Figure 4.2: Excess hole in hematite: 4x4x1 supercell excess spin density for ground state hole polaron. A hole polaron localised on an iron atom has three degenerate structures (A, B, and C) due to the octahedral distortion of the Fe-O bonds. The entire supercell spin density is shown (top row), with a zoomed in image of the hole polaron (bottom row). Bond lengths (top row) and differences with respect to neutral hematite (bottom row) are shown between the iron atom and bonded oxygen atoms in Angstrom.

Electronic coupling / meV			
	$1^{(A)}$	$1^{(B)}$	$1^{(C)}$
$0^{(A)}$	203	110	101
$0^{(B)}$	110	53	39
$0^{(C)}$	101	39	53

Table 4.1: First nearest neighbour electronic coupling for the hole polaron in bulk hematite, accounting for all possible degenerate structures of atoms 0 and 1. All other atom combinations can be inferred by symmetry, e.g. highest coupling direction $0^{(A)}1^{(A)}$ is equivalent to $0^{(B)}2^{(B)}$.

donor-acceptor orbital combination and electronic coupling, see Table 4.1, and reorganisation and activation energy, Table 4.2. Note that the same set of 5 unique electronic couplings exist for all 3 nearest neighbours.

The 5 unique nearest neighbour couplings can be placed into three groups shown in Fig. 4.3: highest coupling (203 meV) where the polaron in initial and final ET states has $d_{x^2-y^2}$ orbitals aligned along the Fe-Fe direction shown in Fig. 4.3 (upper row); moderate coupling (101, 110 meV) where in one polaronic state the $d_{x^2-y^2}$

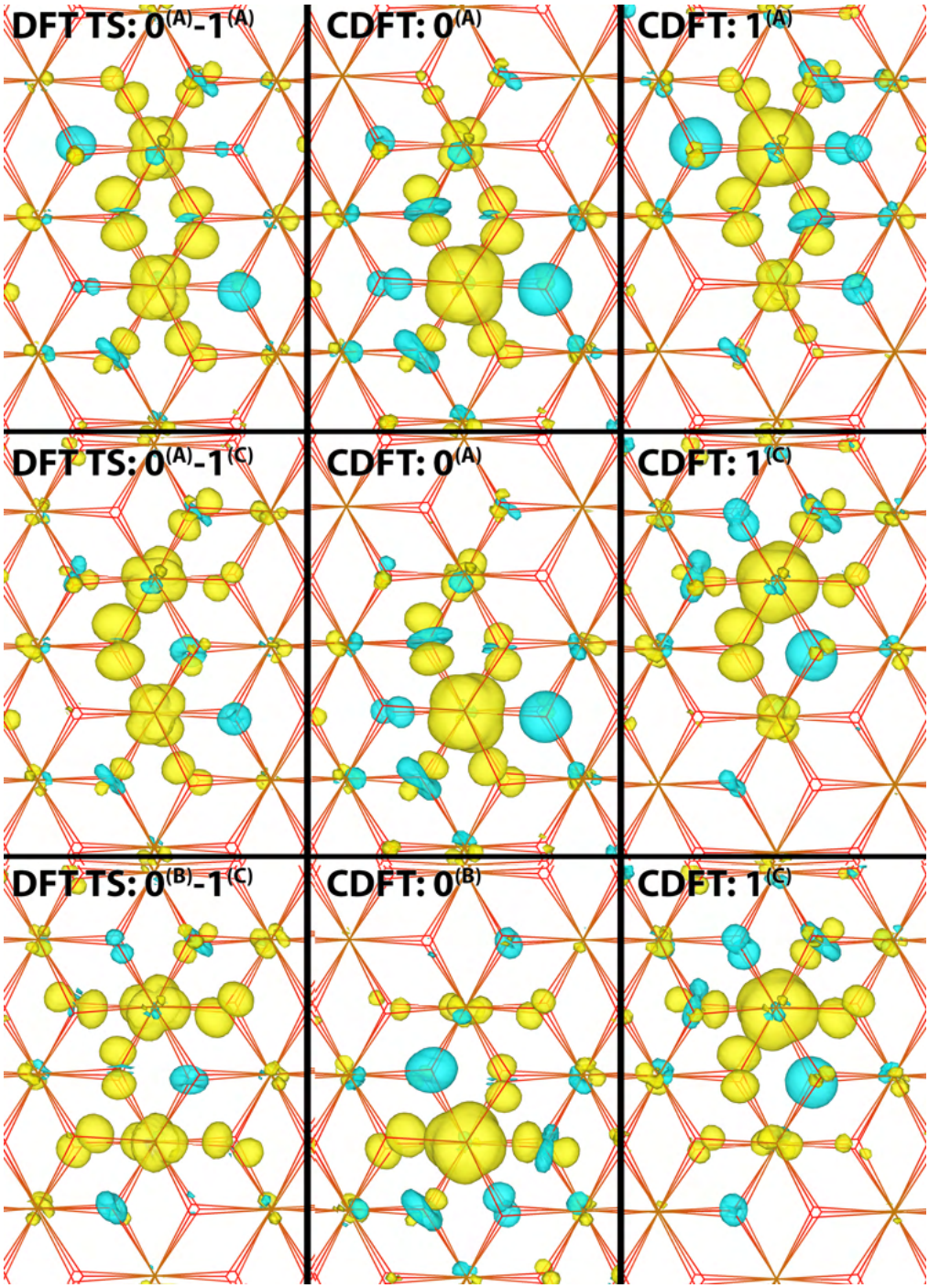

Figure 4.3: Excess hole transition states: 4x4x1 supercell excess spin density for electronic ground state, obtained from DFT calculations (left column) and for the diabatic initial (middle column) and final hole transfer states (right column). The diabatic states are obtained from CDFT with a spin constraint on the Fe atom 0 or 1 respectively, see Figure 4.1 for atom labelling. Only three of the five unique transition state geometries for nearest neighbour hole transfer are shown, see Table 4.2 for hole transfer parameters.

orbital is aligned along the Fe-Fe direction shown in Fig. 4.3 (middle row); low couplings (39, 53 meV) where in neither polaronic state the $d_{x^2-y^2}$ orbital is aligned along the Fe-Fe direction shown in Fig. 4.3 (lower row). The slight differences within these groups (e.g. $0^{(A)}1^{(B)}$ and $0^{(A)}1^{(C)}$) are a result of the asymmetry of the Fe-bilayer. In addition to the electronic couplings the reorganisation energies of the 5 unique combinations are also slightly different, refer to Table 4.2.

Similar considerations apply for second nearest neighbours and beyond. However, as accounting for every structural combination of the hole polaron for all of the second and third nearest neighbours would become too computationally demanding, I choose to only consider these for the (A) orientation of the hole polaron. As Table 2 shows, the decay of the electronic coupling with distance and the increase in reorganisation energy is such that the interaction of the hole polaron with its second and third nearest neighbours is negligible. This means that only nearest neighbour charge transfer processes are important for the hole polaron in bulk hematite, consistent with work from other groups [15, 18].

4.2.2 Electron polaron

In Chapter 3 I showed that the excess electron in hematite is delocalised over two neighbouring iron sites in the DFT electronic ground state. According to electron transfer theory, this suggests that electronic coupling between 1-site localised excess electronic states is so large that they are are no longer stable states, as they no longer correspond to a minimum of the ground state potential energy surface. This is the case when $H_{\mathrm{ab}} > \frac{\lambda}{2}$ [39]. I are now in a position to verify this hypothesis using CDFT.

Indeed, using CDFT to constrain the excess electron on a single Fe atom, I obtain a very large coupling value of 407 meV (4x4x1 supercell), while an upper limit for reorganisations energy for nearest neighbour hopping of a 1-site localised polaron from Chapter 3 is 0.68 eV, hence $H_{\mathrm{ab}} > \frac{\lambda}{2}$. Thus, both DFT calculation of the electronic ground state (adiabatic representation) and CDFT calculations of spin-localised states (diabatic representation) suggest that the 1-site localised electron polaron is unstable and delocalises over 2 adjacent sites.

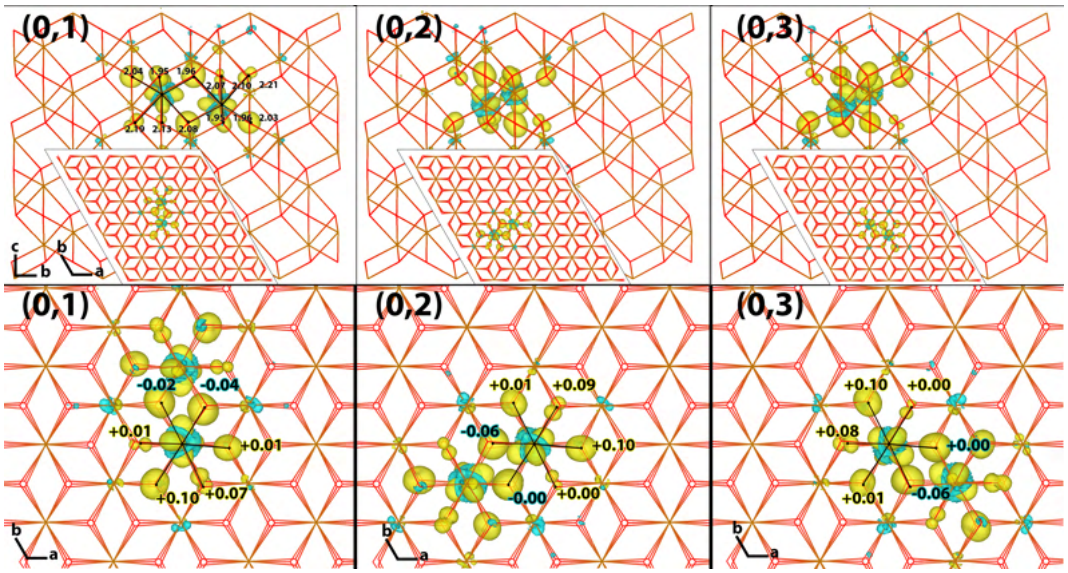

Figure 4.4: Excess electron in hematite: 4x4x1 supercell excess spin density for ground state electron polaron. As the electron polaron is localised across two iron atoms, for any combination of first nearest neighbours, the structures are degenerate. The entire supercell spin density is shown (top row), with a zoomed in image of the electron polaron (bottom row). Bond lengths (top row) and differences with respect to neutral hematite (bottom row) are shown between the iron atom and bonded oxygen atoms in Angstrom.

Considering a given iron atom “0", delocalisation can occur over one of the three first nearest neighbours of 0: either (0,1); (0,2) or (0,3) (see Fig. 4.4 for numbering scheme). These states are energy degenerate due to the symmetry of the lattice. There are several possible charge transfer events of 2-site delocalized electron polaron. The shortest transfer (2.97 Å between centres of excess spin) includes the transitions: (0,1)-(0,2); (0,1)-(0,3) and (0,2)-(0,3) where (0,1)-(0,2) denotes the electron transfer from the 2-site delocalized state (0,1) to the 2-site delocalized state (0,2), and similarly for the other electron transfers. All of these three electron transfers are equivalent by symmetry. The coupling between these adjacent states of 26 meV is surprisingly small given that they share an Fe atom with significant excess spin density in both states. The reason is that the Fe t_{2g} orbital carrying the excess spin density is rotated by 120 degrees with respect to one another in the two diabatic electronic states, see Figure 4.5 (upper row). This results in a small overlap of the two (non-orthogonal) diabatic CDFT electronic wavefunctions and thus a small electronic coupling.

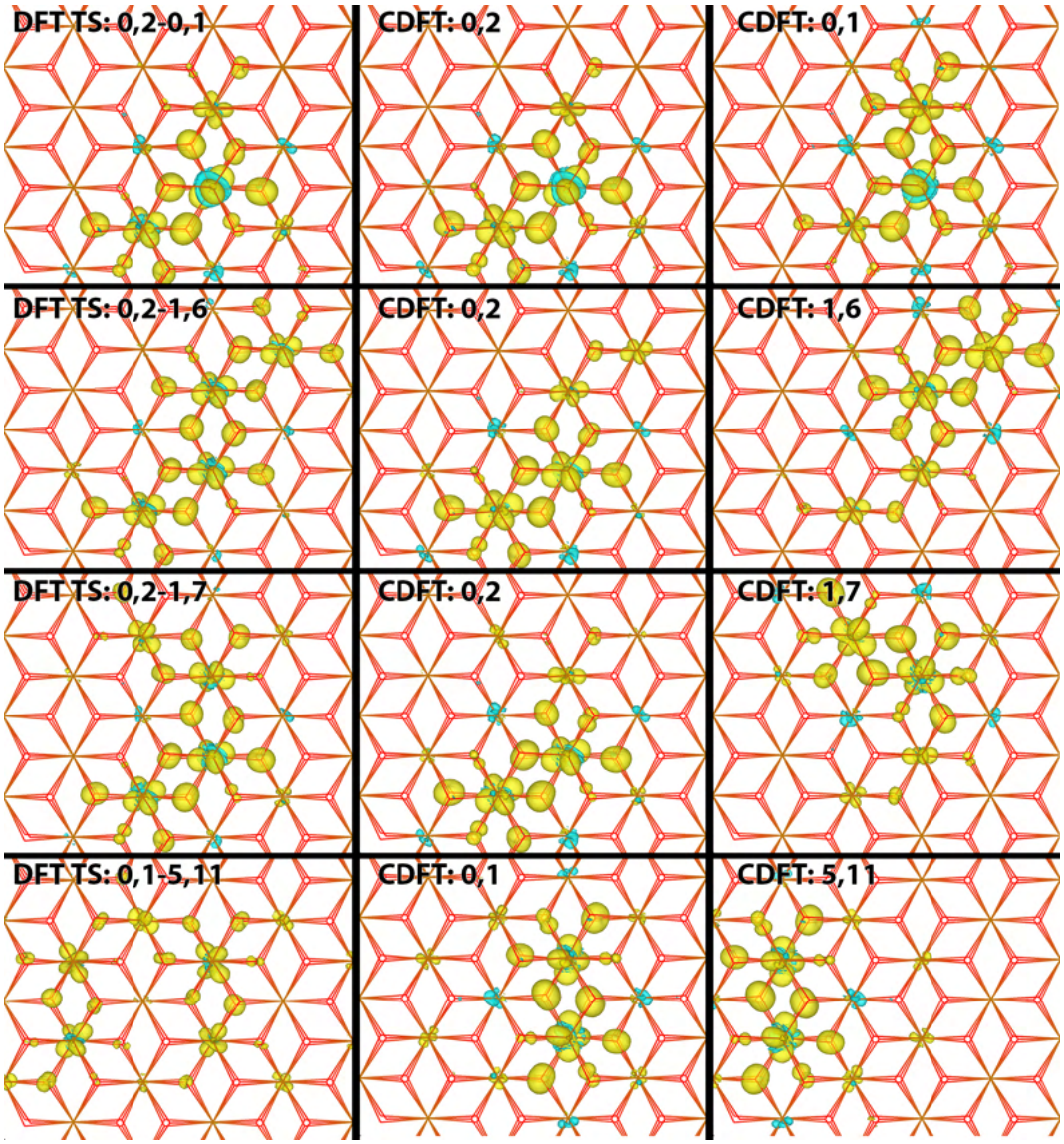

Figure 4.5: Excess electron transition states: 4x4x1 supercell excess spin density for electronic ground state, obtained from DFT calculations (left column) and for the diabatic initial (middle column) and final electron transfer states (right column). The diabatic states are obtained from CDFT with a spin constraint on the two Fe atoms as indicated, see Figure 4.1 for atom labelling. The first row is for electron transfer over the shortest distance (2.97 Å) and the second to fourth row for electron transfer over the second shortest distance (5.04 Å). See Table 4.2 for electron transfer parameters.

Transfers over the next largest distances (5.04 Å between the centres of excess spin) includes the transitions: (0,2)-(1,6), (0,2)-(1,7) and (0,1)-(5,11) as shown in Fig. 4.5. The highest coupling of 57 meV is found for combination (0,2)-(1,6) where the Fe t_{2g} orbitals which the excess electron occupies are orientated parallel. While

the combination (0,1)-(5,11) has the same centre of mass distance, the iron atoms do not share Fe-O bonds as for the other two transition states and as such the coupling is the lowest of the three. Refer to Table 4.2 for all electron transfer parameters.

4.2.3 Electron hole and electron mobilities

The three structurally degenerate states of the hole polaron are expected to interconvert fast, on the time scale of the high frequency lattice modes ($\sim 10^{13}$ s^{-1}). As such, I perform a Boltzmann average over the electronic couplings and reorganisation energy for the 9 possible transitions i, with weights proportional to $\exp(-\beta\lambda_i/4)$, and use the averages for calculation of a nearest neighbour hopping rate (Eq. 2.1). The latter is $\sim 10^{12}$, slow enough to support degenerate mixing of hole states by phonons. The rates for second and third nearest neighbour hops are orders of magnitudes smaller showing that only first nearest neighbour hops are important for hole polaron transport.

Table 4.2 gives the hole mobility for bulk hematite in the 2D (Fe bilayer) plane at room temperature, calculated by solving a chemical master equation to get the MSD and diffusion coefficient (Eq. 2.10) as by Giannini et al. [41]. Inclusion of the six second nearest neighbours and three third nearest neighbours of the hole polaron increases the mobility only from 3.08×10^{-2} to 3.10×10^{-2} cm^2/Vs. To the best of my knowledge this is the first calculation of a mobility tensor in hematite, which fully accounts for the effect of the 2D conduction environment.

For the electron polaron, I consider both the three transitions over the shortest possible distance and the transition over the next largest distance having the highest electronic coupling. Due to the 2-site delocalised electron polaron structure, there are only four symmetry related second nearest neighbours to which the polaron may hop. This introduces a similar complication to the hole polaron, that for a single energy degenerate structure of the electron polaron the mobility is locally anisotropic. As there are three energy degenerate structures for a given electron polaron, the overall mobility remains isotropic. The electron mobility calculated for hopping to first nearest neighbours is 2.0×10^{-2} cm^2/Vs while for second nearest neighbours is 7.8×10^{-2} cm^2/Vs, as a consequence of how the coupling for first nearest neighbours

is smaller than for second nearest neighbours due to unfavourable orientation of orbitals. Accounting for both the first and second nearest neighbour contributions to the diffusion coefficient gives a total mobility of 9.8×10^{-2} cm^2/Vs. Hops across larger distances are not expected to contribute to electron mobility as the electronic coupling for those decays very quickly. I note that the hopping activation energy of 80 meV is much smaller than the ionisation energy into the valence band.

4.2.4 Finite size effects

The results shown in this Chapter are for the 4x4x1 supercell of hematite, with a total of 480 atoms and 4800 electrons. It could be argued that the 2x2x1 supercell (120 atoms, 1200 electrons) is large enough for the first nearest neighbour interactions. Table 4.3 shows that this is true for the weak coupling directions, but not for the highest coupling direction for which I observe a non-negligible increase from 167 to 203 meV. I analysed the origin for this by preparing a transition state geometry in the 2x2x1 supercell that has exactly the same geometry as the one obtained for the 4x4x1 supercell. The coupling is virtually identical in both cases which means that the increase in coupling going from the 2x2x1 to the 4x4x1 supercell is due to a slightly different geometry of the transition state structure in the 4x4x1 supercell (rather than due to other finite size effects such as, e.g., polarisation effects due to polaron images). The slight differences in nuclear relaxation are also indicated by a small decrease in reorganisation energy going from 2x2x1 to 4x4x1, which I attribute to a smaller reorganisation of the first coordination shell ("inner sphere") in the larger supercell.

Use of a 4x4x1 supercell is essential for the calculation of ET parameters for third nearest neighbours for the hole and second nearest neighbour for the electron polaron. This supercell should be large enough as the distance to the third nearest neighbour of the hole polaron is a factor of 3 smaller than to the distance to the closest periodic image. Remaining finite size effects could not be investigated as supercells larger than 4x4x1 are computationally unfeasible at the moment.

Table 4.2: Summary of ET parameters. Coupling, reorganisation energy, activation energy, transmission coefficient and rate constant for bulk hematite at room temperature. For the hole polaron the Boltzmann average for the electronic coupling and reorganisation energy is calculated for each nearest neighbour, while for the electron polaron there is only a single second nearest neighbour with an adiabaticity parameter greater than one and therefore this is not necessary.

r / Å	Neighbour	H_{ab} (meV)	λ (meV)	$\Delta E^{\ddagger}$ (meV)	κ_{el}	k (s^{-1})
Hole polaron						
2.97	$0^{(A)}$-$1^{(A)}$	203	652	23	1.0	7.5×10^{12}
	$0^{(A)}$-$1^{(B)}$	110	814	108	1.0	2.8×10^{11}
	$0^{(A)}$-$1^{(C)}$	101	784	108	1.0	2.8×10^{11}
	$0^{(B)}$-$1^{(B)}$	53	865	166	0.9	2.5×10^{10}
	$0^{(B)}$-$1^{(C)}$	39	881	183	0.7	1.1×10^{10}
	Average	147[a]	752[b]	70	1.0	1.2×10^{12}
5.04	$0^{(A)}$-$4^{(A)}$	15	1050	248	0.2	2.2×10^{8}
	$0^{(A)}$-$5^{(A)}$	8	1050	255	0.1	5.3×10^{7}
	$0^{(A)}$-$6^{(A)}$	15	1028	242	0.2	2.8×10^{8}
	$0^{(A)}$-$7^{(A)}$	30	1016	225	0.5	1.5×10^{9}
	$0^{(A)}$-$8^{(A)}$	28	1022	228	0.5	1.2×10^{9}
	$0^{(A)}$-$9^{(A)}$	16	1034	243	0.2	3.0×10^{8}
	Average	21[a]	103[b]	237	0.3	5.7×10^{8}
5.87	$0^{(A)}$-$10^{(A)}$	3	1087	269	0.0	4.4×10^{6}
	$0^{(A)}$-$11^{(A)}$	9	1106	268	0.1	3.9×10^{7}
	$0^{(A)}$-$12^{(A)}$	45	1026	213	0.8	3.6×10^{9}
	Average	32[a]	1061[b]	234	0.5	1.1×10^{9}
Electron polaron						
2.97	(0,1)-(0,2)	26	363	67	0.6	8.0×10^{11}
5.04	(0,2)-(1,6)	57	522	80	0.9	7.7×10^{11}
	(0,2)-(1,7)	19	572	125	0.3	4.9×10^{10}
	(0,1)-(5,11)	10	641	150	0.1	5.7×10^{9}

[a] Boltzmann average for electronic coupling $H_{ab} = \left(\sum_i H_{ab,i}^2 e^{\frac{-\lambda_i}{4k_B T}} / \sum_i e^{\frac{-\lambda_i}{4k_B T}} \right)^{\frac{1}{2}}$ for hole transition states i.

[b] Boltzmann average for reorganisation energy $\lambda = 4 \left(\sum_i \frac{\lambda_i}{4} e^{\frac{-\lambda_i}{4k_B T}} / \sum_i e^{\frac{-\lambda_i}{4k_B T}} \right)$ for hole transition states i.

	Supercell size			
	2x2x1	4x4x1	2x2x1	4x4x1
Neighbour	H_{ab} / meV		λ / meV	
$0^{(A)}$-$1^{(A)}$	167	203	843	652
$0^{(A)}$-$1^{(B)}$	36	39	1012	881
$0^{(A)}$-$1^{(C)}$	51	53	1035	865

Table 4.3: Comparison of first nearest neighbour electronic coupling and reorganisation energy for the hole polaron, 2x2x1 and 4x4x1 supercells.

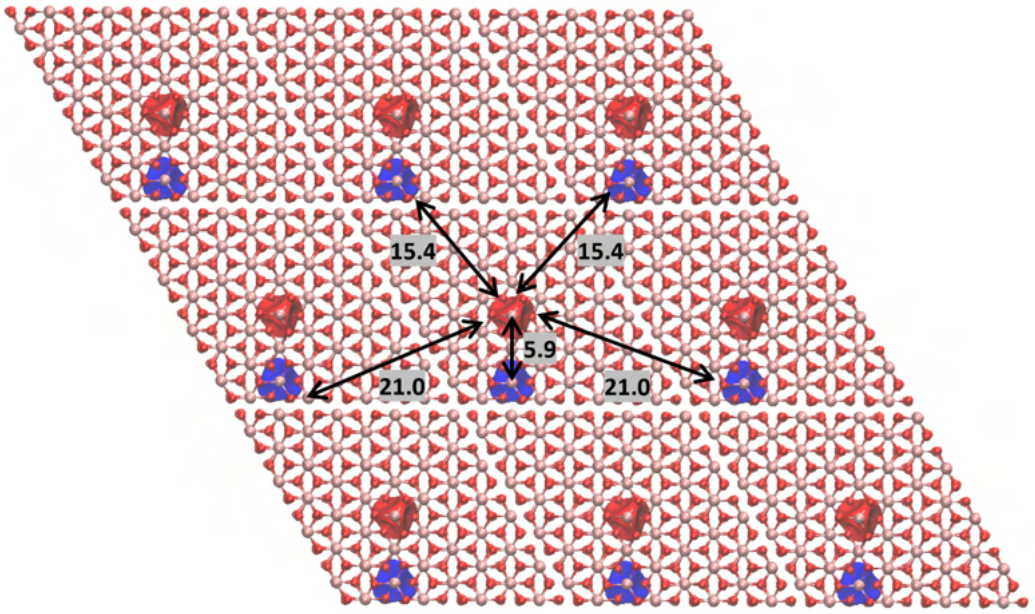

Figure 4.6: Finite size effects of the hole polaron. Isosurface of CDFT weight function, showing that the distance between the third nearest neighbour of 5.9 Å is a factor of three smaller than the distance to the periodic image of this charge (15.4 Å).

4.3 Discussion

Table 4.2 shows a comparison of my calculated and literature results, with Figure 4.8 showing this comparison plotted as mobility against temperature. A direct comparison of different mobility calculations is difficult due to the different methods used, and therefore I alleviate this somewhat by comparing to mobilities obtained according to Equations 2.1-2.11 using the reported literature values for electronic couplings and reorganisation energy. A simplified schematic for both hole and electron polaron hopping is shown in Figure 4.7.

Rosso and co-workers [15,18] performed Hartree-Fock calculations of both hole and electron mobility for small hematite clusters, considering up to second nearest

Table 4.4: Summary of results and comparison with literature. To facilitate direct comparison, both the mobility cited in the paper (μ_{lit}) as well as mobilities re-calculated using Equations 2.1-2.11 for the 2D basal plane (μ_{2D}) are provided. Literature results are presented in chronological ordering by method.

Source	Dopant	H_{ab} (meV)	λ (meV)	$\Delta A^{\ddagger}$ (meV)	T (K)	μ_{lit} (cm^2/Vs)	μ_{2D} (cm^2/Vs)
Hole polaron							
This work		147	752	70	300		3.1×10^{-2}
This work		147	752	70	1000		6.1×10^{-2}
Cluster HF [18]		200	1590	220	298	1.7×10^{-4}	8.3×10^{-5}
Estimate [148]				100	300	1×10^{-2}	
Experiment [149]	Mg			200	1000	9.1×10^{-1}[a]	
Electron polaron							
This work		57	522	80	300		9.8×10^{-2}
This work		57	522	80	1000		2.0×10^{-1}
Cluster HF [15]		200	1200	110	298	6.2×10^{-2}	2.6×10^{-3}
Cluster HF [18]		190	1420	190	298	5.6×10^{-4}	2.9×10^{-4}
Bulk DFT [43]		41	(674)[b]	130	300	9.0×10^{-3}	1.4×10^{-3}
Bulk DFT [150]		40	800	(162)[b]	300		6.2×10^{-4}
Estimate [148]				100	300	1×10^{-2}	
Experiment [151]	Nb, Zr				960-1500	1×10^{-1}	
Experiment [149]	Ti			170	1000	2.8×10^{-1}[a]	
Experiment [152]	2%Ti			80	780	2×10^{-2}	
Experiment [153]	3%Ti			118	290	4×10^{-2}	
Experiment [153]	5%Ti			116	290	4.6×10^{-1}	
Experiment [153]	9%Ti			116	290	1.4×10^{-1}	

[a] Calculated from fitted mobility equation given in paper, valid above 923 K.

[b] Calculated in this work from values in paper.

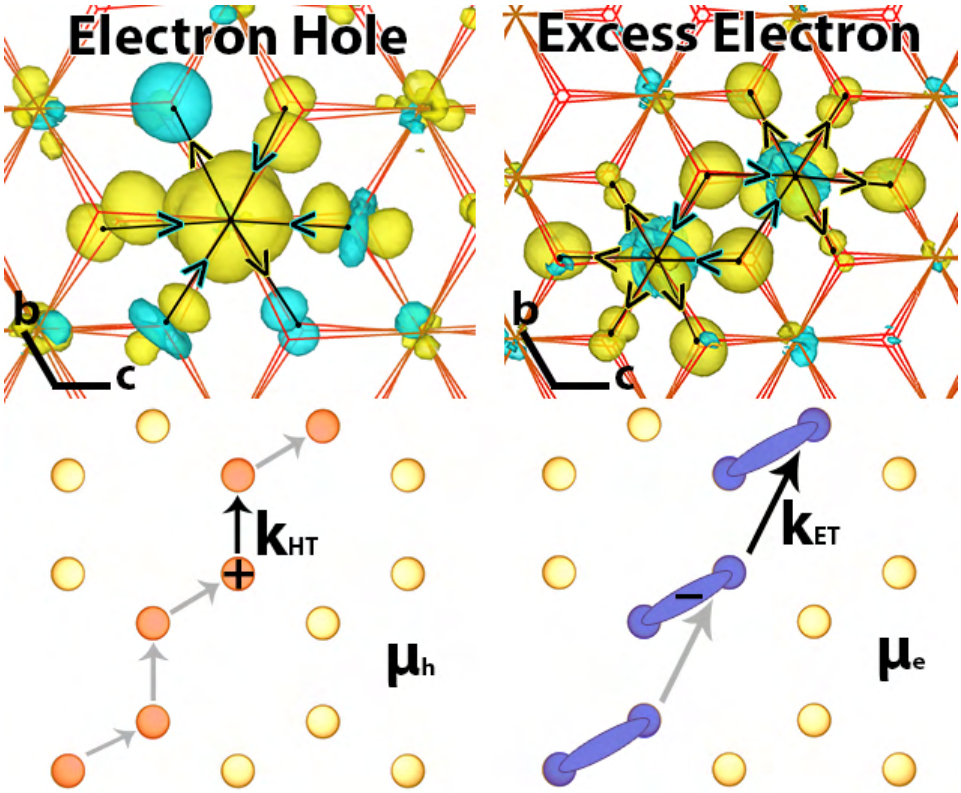

Figure 4.7: Polaron structures and hopping mechanisms. Excess spin density (top row) for the electron and electron hole polarons, simplified hopping schematic (bottom row) showing the hopping of the 1-site localised hole polaron and the 2-site delocalised electron polaron.

neighbours. Both their couplings and reorganisation energies tend to be considerably higher resulting in larger activation energies and lower mobilities for both electrons and holes. Though, one early estimate reported by Rosso and co-workers [15] for electron mobility is within a factor of 1.6 of my current best estimate. In Chapter 3 I attributed the larger reorganisation energy of cluster models to the absence of lattice strain effects present in the bulk structure, as well as the use of Hartree-Fock which tends to overbind excess charge.

Adelstein et al. [43] and Behara et al. [150] calculated electron mobilities using a similar approach as in this work with a 2x2x1 supercell, but using DFT+U in place of hybrid CDFT to model the polaronic states. Their reorganisation energies are similar, albeit slightly higher than mine and significantly smaller than typical values for cluster models. In fact, Behara reported values for bulk hematite around half of that for the 1D chain [150]. Their electronic coupling values are also very

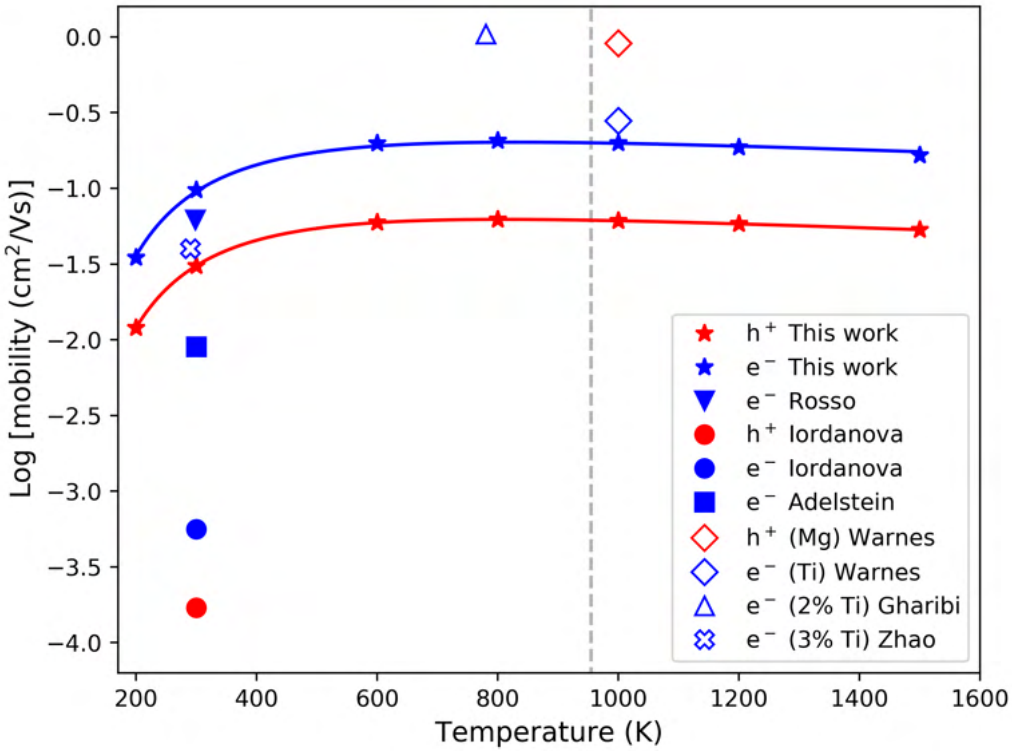

Figure 4.8: Mobility as a function of temperature. Literature calculated mobilities indicted with solid filled markers, doped experimental mobilities as unfilled markers. My results are valid below the Neel temperature (T=955 K) [147], indicated with a dashed line.

similar to my estimates but this is a coincidence as my electronic polaronic states are 2-site delocalized whereas theirs are localised on a single iron atom. The 2-site delocalisation also permits larger transfer distances for a single hop resulting in higher mobilities than the 1-site localised polaron (see R^2 dependence, Eq. 2.10). This is partly the reason for the higher electron mobilities that I obtain in this current work compared to Adelstein et al. and Behara et al. Interestingly, Adelstein et al. in their calculations did find that there was some degree of delocalisation of the electron polaron over two iron atoms, identified from both a shorter Fe-Fe bond length and from the magnetic moment.

While other groups have attempted a justification of their results via comparison to experiment, this is problematic as there are no experimental results for the mobility of pure (undoped) hematite. The available experimental mobilities are all for doped hematite, sometimes for temperatures above the Neel temperature where hematite

is no longer anti-ferromagnetic (955 K) [147]. Further, as there are no direct measurements of either the reorganisation energy or couplings there are multiple combinations of each that would compare well with the observed mobilities.

The most suitable experimental data for comparison are probably the ones reported by Zhao et al [153] for electron mobility in 3% and 5% Ti-doped hematite. These values are within a factor of 2.5 of my computed mobilities for pure hematite, which is reassuring despite the above mentioned caveats.

4.4 Conclusion

In this Chapter both the electron and hole mobility has been calculated for hematite using spin-constrained gap-optimised hybrid density functional theory with large supercells. Where previous studies have only considered coupling between a single nearest neighbour or a single orientation of the polaron, I account for all possible degenerate polaron structures and coupling with up to third nearest neighbours. In addition, for the first time the mobility is calculated for the full 2D Fe bilayer rather than for a 1D model.

The CDFT calculations provide further evidence that the excess electron is delocalized over two iron sites and hops across the hematite crystal as a two-site delocalized polaron. While the activation energy for these hops is slightly higher, the hopping distance is larger than for the 1-site localised hole polaron. As a consequence, the electron mobility is predicted to be a factor of 3 higher than the hole mobility.

Charge transport has been identified as a key issue for the use of hematite in a number of technological applications, especially in photocatalysis and photoelectrochemistry [6, 9, 11, 154]. This Chapter provides a comprehensive and detailed understanding of the physical mechanisms that lead to the sluggish transport of charge carriers in bulk hematite. This sets the scene for similar calculations at the hematite/liquid water interface (see Chapter 5). In particular, it will be important to understand if and how the presence of water at the interface changes the picture obtained for the bulk material and how this depends on the specific surface cut under

investigation and the protonation state of the surface [100]. Such investigations, which my work has now made possible, could help refine models, and resolve ongoing questions, about rate-limiting transport processes governing photocatalytic water splitting efficiency at hematite/water interfaces [11, 154].

I have shown in this Chapter that CDFT is a useful tool for the prediction of charge mobilities in an ubiquitous oxide material. The method is generally applicable to semiconducting materials and may be applied to other oxides of technological interest for the study of intrinsic charge transfer processes or for charge transfer between defects. Moreover, the CDFT approach is well suited for the study of interfacial charge transfer processes between different semiconductors or between semiconductor electrodes and liquids. It could thus become an essential tool for the emerging field of *ab-initio* electrochemistry [155].

Chapter 5

Implementation and validation of CDFT forces

Recently CDFT has been implemented in the CP2K simulation package [84, 90], however the CDFT forces required for CDFT geometry optimisation and molecular dynamics simulation are currently only available for Becke partitioning of the electron density. Therefore, in this Chapter I present the implementation of CDFT forces arising from the more robust Hirshfeld partitioning scheme of the electron density. I find that CDFT is a powerful tool for the calculation of electron transfer parameters at a reasonable computational cost. This work has recently been accepted for publication [156].

In this Chapter I first discuss the motivation for Hirshfeld based CDFT and provide the necessary force terms, Section 5.1, before presenting validation and benchmarking for both CDFT geometry optimisation (Section 5.2.1) and CDFT molecular dynamics (Section 5.2.2). An example of systems for which CDFT calculations can be problematic is shown in Section 5.2.3, and a discussion of the general reliability of condensed phase CDFT calculations is presented in Section 5.2.4.

Atom	Becke	Hirshfeld
O	0.84	-0.30
H	-0.42	0.15

Table 5.1: Atomic charges for a neutral water molecule according to different partitioning schemes. Becke charge partitioning produces qualitatively incorrect charges, with a large positive charge on the oxygen atom in contrast to the small negative charge from Hirshfeld charge partitioning.

5.1 Theory and implementation

In recent years there have been several new implementations of CDFT in popular DFT packages [20, 33, 84–88, 157, 158], which generally follow the seminal work by Wu and Van Voorhis [159]. As outlined in Chapter 2.3, a Lagrangian multiplier is introduced to search for an external potential applied to the Kohn-Sham Hamiltonian, performed self-consistently with a second iteration loop in addition to that of a standard DFT calculation. The definition of this external potential introduces a weight function, describing the partitioning of electron density (or charge). In their earlier work [159] Wu and Van Voorhis utilised the Lowdin atomic population scheme [160], later recommending real space partitioning schemes of the electron density, in particular Becke partitioning [161]. As a purely geometric approach that divides space equally between all atoms, Becke partitioning of the electron density avoids any issues with basis set convergence found for Lowdin or Mulliken atomic charge partitioning [80]. An alternative real space partitioning scheme is the one according to Hirshfeld [113] where molecular electron density is assigned to atoms in proportion to their promolecular density, thus accounting for their different sizes.

Table 5.1 demonstrates the problem of equally dividing space between all atoms as done in Becke partitioning, that for a water molecule the oxygen atom becomes positively charged and the hydrogen atoms become negatively charged. This is in direct contrast to Hirshfeld charge partitioning, which predicts a qualitatively correct charge distribution. The qualitative failure of Becke charge partitioning in heteronuclear systems is well known [161], where it is common to define atomic size adjustments based on either covalent or ionic radii [84]. Such introduction of empirical parameters is undesirable, with significant ambiguity in their choices. I

note that an approximation made in Hirshfeld partitioning is in the use of neutral atomic densities to calculate the weight function, although it is possible to apply this to charged densities via an iterative extension of Hirshfeld partitioning (Hirshfeld-I) [117]. To the best of my knowledge there are no CDFT implementations which use Hirshfeld-I, or any other charge partitioning scheme more sophisticated than standard Hirshfeld partitioning.

In CDFT the total force on an atom i is given by

$$\mathbf{F}_{\mathrm{tot},i} = \mathbf{F}_i + \mathbf{F}_{ci}, \tag{5.1}$$

where $\mathbf{F}_i$ is the usual force arising from the unmodified DFT functional $E[\rho]$ and $\mathbf{F}_{ci}$ is the additional force arising from the constraint. The latter is given by

$$\mathbf{F}_{ci} = -V \int \rho(\mathbf{r}) \frac{\partial w(\mathbf{r},\mathbf{R})}{\partial \mathbf{R}_i} \mathrm{d}\mathbf{r}. \tag{5.2}$$

The derivative of the weight function can be shown to be [33]

$$\frac{\partial w(\mathbf{r})}{\partial \mathbf{R}_i} = \frac{\delta - w(\mathbf{r})}{\sum_J \rho_J(\mathbf{r} \text{ - } \mathbf{R}_J)} \frac{\partial \rho_i(\mathbf{r} \text{ - } \mathbf{R}_i)}{\partial \mathbf{R}_i}, \tag{5.3}$$

where

$$\delta = \begin{cases} 1 & i \in D \\ -1 & i \in A \\ 0 & i \notin D \cup A. \end{cases} \tag{5.4}$$

The derivative of the density is given by [33]

$$\frac{\partial \rho_i(\mathbf{r} \text{ - } \mathbf{R}_i)}{\partial \mathbf{R}_i} = \frac{\partial \rho_i(|\mathbf{r} \text{ - } \mathbf{R}_i|)}{\partial \mathbf{R}_i} = \frac{\partial \rho_i(|\mathbf{r} \text{ - } \mathbf{R}_i|)}{\partial |\mathbf{r} \text{ - } \mathbf{R}_i|} \frac{\mathbf{r} \text{ - } \mathbf{R}_i}{|\mathbf{r} \text{ - } \mathbf{R}_i|}. \tag{5.5}$$

In CP2K the atomic densities ρ_i are calculated by performing a DFT calculation on the isolated atoms, and fitting a minimal Gaussian basis set to this density. As such, the radial derivatives are known analytically. The calculation of the atomic densities and their derivatives is performed only once per atomic species, and therefore the

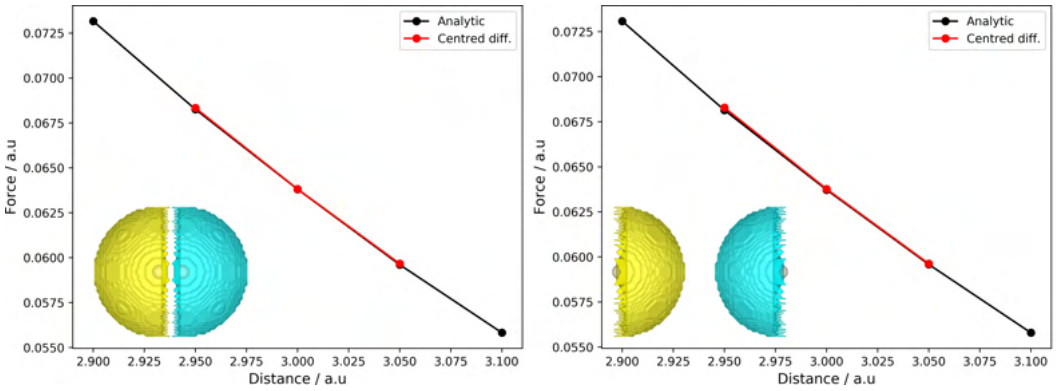

Figure 5.1: (A) Verification of analytical forces against forces calculated from centred finite differences of the total energy for a helium dimer, both with (right) and without (left) periodic boundary conditions. For the system under periodic boundary conditions, the helium dimer interacts at the same distance except with their periodic image and therefore the resultant force is the same. An isosurface of the weight function is shown on the bottom left of each figure.

computational cost is negligible.

To both ensure numerical stability and to further reduce the computational cost, an adjustable cutoff is introduced for the denominator of Eq. 2.19. When the total promolecular density is smaller than $1 \times 10^{-12} e$ the weight function is set to zero. Similar numerical cutoffs can be found in other implementations of CDFT based on Hirshfeld partitioning of the electron density [88]. I have verified that the total energy and forces are insensitive to this choice of cutoff.

A simple test of the implementation of the constraint force and Hirshfeld partitioning can be performed by checking that the total force is equal to the force calculated from finite differences of the minimised energy functional $W[\rho, V]$ subject to the density constraint. Such a comparison is performed for the helium dimer He_2^+. The difference in the force obtained from Eq. 5.1 and the finite difference calculation is 4.7×10^{-5} H/Bohr, similar to that obtained from other CDFT implementations [88].

5.2 Results

I present validation and benchmarking of the CDFT force implementation for both geometry optimisation (Section 5.2.1) and molecular dynamics (Section 5.2.2), for a variety of systems. Through considering a wider selection of systems than previous

	DFT (isolated)	DFT	CDFT
$(O_1-H_1)^+$ / Å	1.017	0.988	1.017
$(O_1-H_2)^+$ / Å	1.017	0.989	1.017
θ^+_{HOH}	108.51	105.91	108.50
(O_2-H_3) / Å	0.970	0.988	0.971
(O_2-H_4) / Å	0.970	0.985	0.971
θ_{HOH}	104.17	105.95	103.94

Table 5.2: Geometry optimisation of a water dimer $(H_2O)_2^+$ in vacuum at a distance of 10 Å. With the use of CDFT to form the charge localised state H_2O^+-H_2O, the bond lengths and angles of the isolated H_2O^+ and H_2O molecules are reproduced. In comparison, standard DFT predicts that the excess hole is equally delocalized over both molecules and the geometry of the two molecules is the same.

work, I am also able to discuss the general reliability of condensed phase CDFT calculations (Section 5.2.4).

5.2.1 CDFT geometry optimisation

5.2.1.1 $(H_2O)_2^+$ in vacuum

Charged dimers or molecular clusters are a well known problem for standard DFT functionals [50]. The electron delocalisation errors tends to favour charge delocalisation over charge localisation, in particular for situations where both these states are energy degenerate in exact theory, e.g. in a charged molecular dimer at the dissociation limit. CDFT can be used to correct this error. In the following I consider the water dimer cation, creating the charge localised state H_2O^+-H_2O by imposing a charge difference constraint of N_c=1e between the donor (H_2O) and acceptor (H_2O^+) regions using the Hirshfeld weight function Eq. 2.19. The constraint is converged until the residual error is less than $1\times10^{-4}e$, with a energy gradient of 1×10^{-6} Ha. Calculations are performed in vacuum for a centre of mass distance of 10 Å, with the PBE-D3 functional [46, 162]. Geometry optimisation is converged until the residual forces are smaller than 0.02 eV/Å. Unless specified otherwise these values were used for all systems studied in this work.

Table 5.2 shows the DFT optimised geometries of the isolated H_2O^+ and H_2O molecules, confirming that CDFT geometry optimisation of the charge localised state H_2O^+-H_2O reproduces these geometries for the large water-water separation of

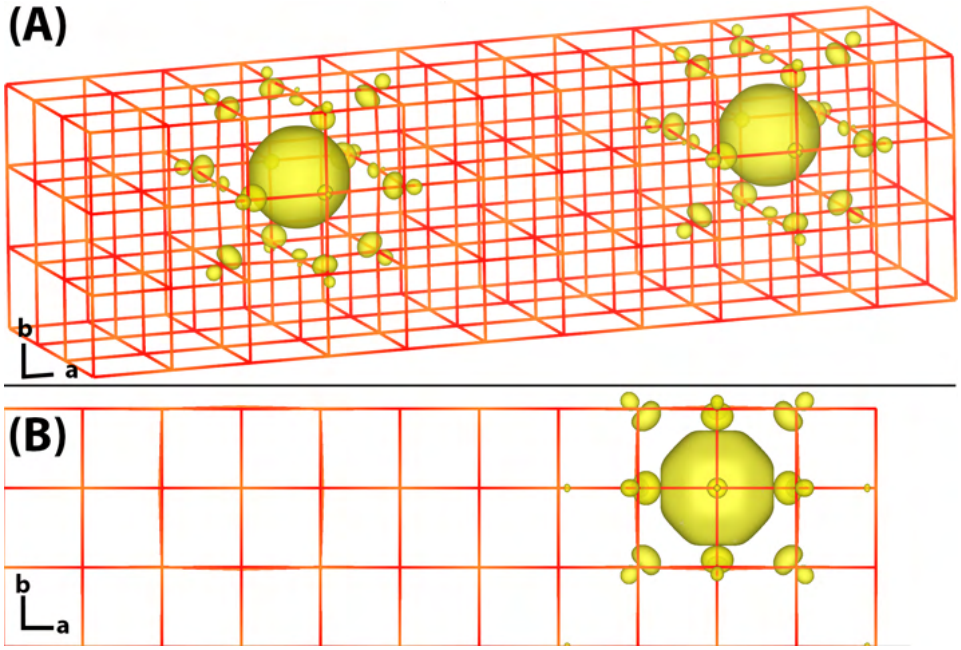

Figure 5.2: Oxygen defects in MgO. Excess spin density for: (A) DFT adiabatic ground state and (B) CDFT diabatic state on the adiabatic ground state optimised geometry with a defect separation of 12.76 Å. The increase in spin density (yellow) is composed of a s-like function at the defect site and the p-orbitals of the surrounding oxygen atoms.

10 Å, as it should do. Not surprisingly, DFT predicts that the excess hole is equally delocalized over both molecules and the geometry of the two molecules is the same, between the one for neutral water and the water radical cation, i.e. $H_2O^{0.5+}$-$H_2O^{0.5+}$. Similar results are found for CDFT-MD performed at 300 K.

5.2.1.2 Electron transfer in solid MgO

While CDFT is an established method for calculating electron transfer (ET) parameters in molecular systems [34, 80–83], applications to condensed phase/periodic systems remain rare to date. A notable example however is the electron tunnelling between between charged oxygen vacancies (termed F-centre defects) in MgO, previously calculated with a plane-wave implementation of CDFT in CPMD [34, 82]. Oxygen vacancies have been shown to exist in MgO in three possible charge states: F^0, F^+ and F^{2+}, corresponding to the localisation of two, one or zero electrons at the defect site [82]. The electron tunnelling process between defect sites *i* and *ii* is therefore written as

$$F_i^0 + F_{ii}^+ \rightarrow F_i^+ + F_{ii}^0. \tag{5.6}$$

The ET process is modelled by removing two oxygen atoms at a separation d from a MgO rocksalt structure, while removing only one electron. With a total charge of +1 and a multiplicity of 2, a charge difference of N_c=1e defined between the defect sites is used to form the diabatic states. The Hirshfeld weight function is defined as the 6 Mg atoms nearest to the respective defect site. The reorganisation energy for this reaction is defined as

$$\lambda = E_A(\mathbf{R}_B) - E_A(\mathbf{R}_A), \tag{5.7}$$

where $\mathbf{R}_A$ and $\mathbf{R}_B$ are the optimised geometries in the diabatic states A and B. As the initial and final states are the same, the reorganisation energy can be calculated as the vertical energy gap at the minimum of a diabatic state,

$$\lambda = \Delta E(\mathbf{R}_A) = E_B(\mathbf{R}_A) - E_A(\mathbf{R}_A). \tag{5.8}$$

CDFT geometry optimisations of the diabatic states are performed using the PBE functional [46], with single point calculations of the reorganisation energy also performed using the PBE0-TC-LRC functional [46, 58, 91, 163]. The chosen cutoff radius R_c of 7 Å has been shown in previous work to reproduce the experimental MgO band gap of 7.2 eV [34, 164]. For Mg the 2s, 2p and 3s electrons and for O the 2s and 2p electrons are treated explicitly. Due to the very hard pseudopotential of Mg, a real-space integration grid cutoff of 3000 Ry is used.

Fig. 5.2 shows an isosurface of excess spin density for the DFT adiabatic ground state, showing delocalisation of the excess charge over both defect sites, and the CDFT diabatic state calculated for the same geometry with a charge difference of N_c=1e defined between the defect sites. The results of geometry optimising the diabatic state and calculating the vertical energy gap λ are shown in Fig. 5.3. The corresponding reorganisation energies (dashed lines) are very similar (mean residual unsigned error of 4%) to the ones obtained from CP2K CDFT single point

% HFX	n	Cell	λ BW (eV)	λ HW (eV)	λ_{opt} HW (eV)	λ [34] (eV)
0	3	211-240-3	0.94	0.89	0.93	0.76
	4	110-096-4	0.84	0.76	0.78	0.64
	4	110-240-4	1.07	0.96	1.01	0.79
	6	111-216-6	1.27	1.18	1.19	0.98
	9	110-144-9	1.25	1.13	1.14	0.92
	18	100-192-18	1.44	1.35	1.26	1.12
	24	111-288-24	1.37	1.34	1.32	1.11
25	3		1.07	1.00	1.06	0.86
	4		1.01	0.91	1.06	0.78
	4		1.34	1.19	1.29	0.98
	6		1.69	1.56	1.63	1.33
	9		1.69	1.52	1.59	1.26
	18		1.97	1.89	1.85	1.66
	24		1.87	1.85	1.87	1.63

Table 5.3: Comparison of reorganisation energies obtained from CDFT calculations in CP2K with Becke weighting (BW), Hirshfeld weighting (HW) and reference values from CPMD. Results are shown for different percentages of Hartree-Fock exchange and for different defect separations n.

calculations on CPMD CDFT geometries (solid lines) giving reassurance to the present CDFT force implementation. Though the reorganisation energies obtained from CP2K CDFT tend to be somewhat larger than they were reported for CPMD CDFT (mean residual unsigned error of 22%), even if the are calculated on the same geometries. This difference is most likely related to the different functional form of the weight function w (Eq. 2.19) in the two implementations, Gaussian functions in CP2K and Slater functions in CPMD [34, 82]. Other differences such as the basis set, use of ADMM and slight variations in the PBE0-TC-LRC functional used for electronic structure calculations could also contribute to the difference.

I note that while the reorganisation energies are similar for both Becke and Hirshfeld CDFT in CP2K, upon geometry re-optimisation they differ significantly. For the 110-096-4 cell the CPMD PBE0 reorganisation energy is 0.78, increasing to 1.06 eV (+0.28 eV) with CP2K geometry re-optimisation with Hirshfeld partitioning and increasing further to 1.64 eV (+0.87 eV) with Becke partitioning.

In addition to reorganisation energies, I can also compare with the CPMD electronic couplings. The electronic coupling matrix elements between the initial

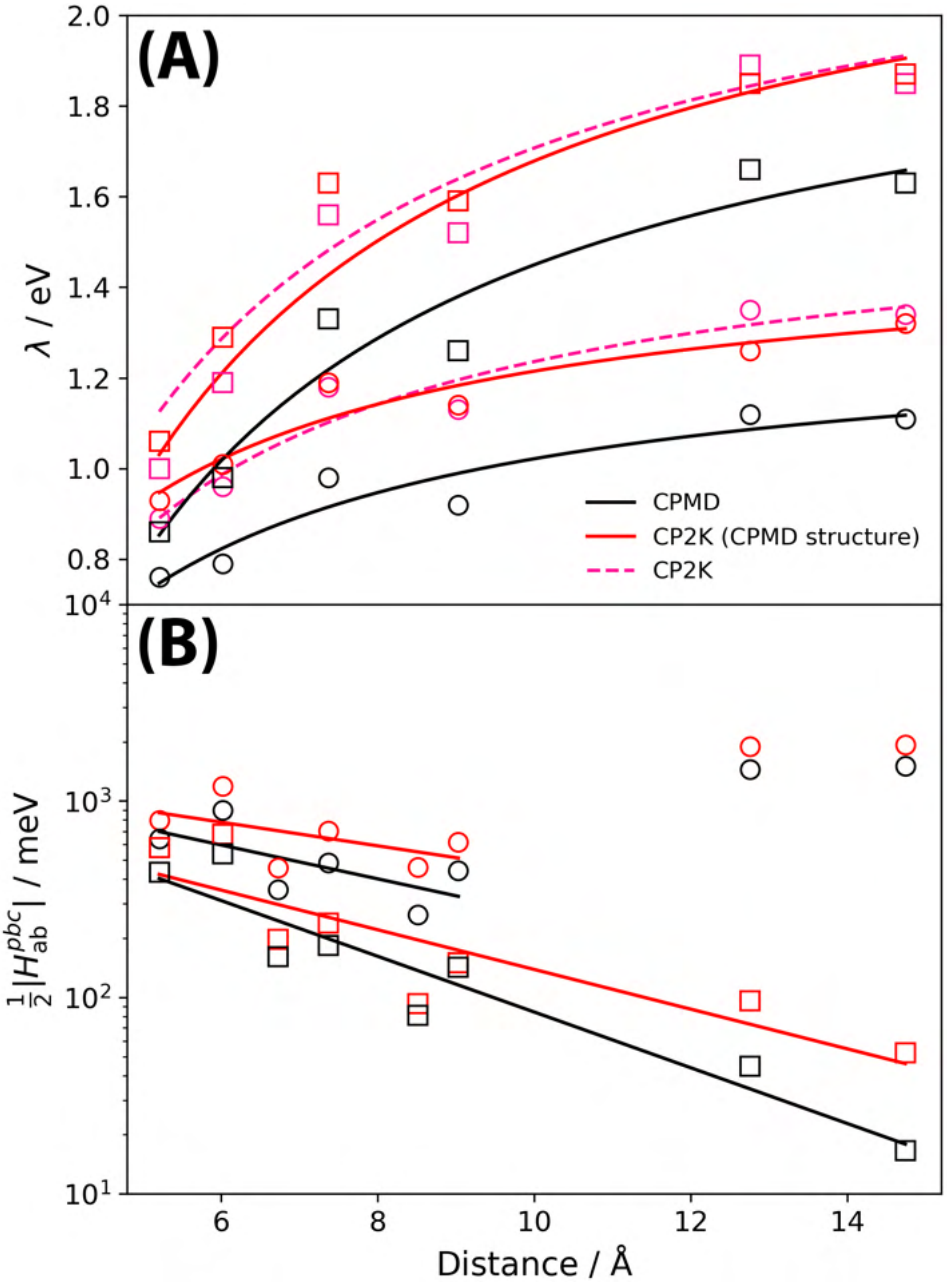

Figure 5.3: (A) Reorganisation energies λ and (B) electronic couplings $\frac{1}{2}H_{ab}^{pbc}$ obtained for tunnelling between oxygen defects in MgO. The black markers represent the CPMD reference values [34], red markers the CP2K values calculated using the CPMD structures and pink markers the CP2K values from re-optimised structures. Results are shown for different percentages of Hartree-Fock exchange and for different defect separations. Circles represent PBE calculations, while squares represent PBE0-TC-LRC calculations. Best fits are indicated by solid and dashed lines.

and final ET states are calculated with CDFT [52] on the transition state structures, approximated by the DFT adiabatic ground state where the electron hole is delocalised over both defects. The supercell size and defect separation were chosen such that in one direction the distance between the defects is equal to the distance to the periodic image of the defects, while the other directions are sufficiently large that periodic images in these directions have only a small effect [34, 82]. The finite size corrected electronic coupling H_{ab} is therefore equal to half of the coupling obtained in periodic boundary conditions $H_{\mathrm{ab}}^{\mathrm{pbc}}$ minus a correction term that accounts for the artificial contribution from the remaining periodic images,

$$H_{\mathrm{ab}}(\mathbf{r}^a,\mathbf{r}^b) = \frac{1}{2}H_{\mathrm{ab}}^{\mathrm{pbc}}(\mathbf{r}^a,\mathbf{r}^b) - \frac{1}{2}\sum_{i,j,k\in[-1,0,1]}^{n} H_{\mathrm{ab}}(\mathbf{r}^a,\mathbf{r}^b_{i,j,k}), \tag{5.9}$$

where in this work the latter correction term is neglected to enable a direct comparison to the CPMD electronic couplings.

Fig. 5.3 compares the electronic couplings calculated with CPMD and CP2K on the CPMD optimised geometries as a function of defect distance, with good agreement for defect distances of up to 10 Å (MRUE = 26%). At larger distances both the PBE and PBE0-TC-LRC CP2K couplings are somewhat larger than reported for CPMD, resulting in a smaller exponential decay value for PBE0-TC-LRC of β = 0.47 $\pm$ 0.06 Å^{-1}, compared to the one reported for CPMD couplings, 0.73 $\pm$ 0.10 Å^{-1} [34, 82]. The overall MRUE error is reasonably small, 58%. For PBE I find a smaller exponential decay value of β = 0.28 $\pm$ 0.10 consistent with CPMD β = 0.40 $\pm$ 0.22.

5.2.2 CDFT molecular dynamics

5.2.2.1 H_2^+ in vacuum

An important consideration in any molecular dynamics calculation is total energy conservation. For CDFT-MD this can be particularly challenging as the constraint is introduced through an additional self-consistent field (SCF) loop, and as such both the DFT and CDFT SCF loops must be well converged in order to ensure total energy conservation. The justification for this is that without a well converged SCF

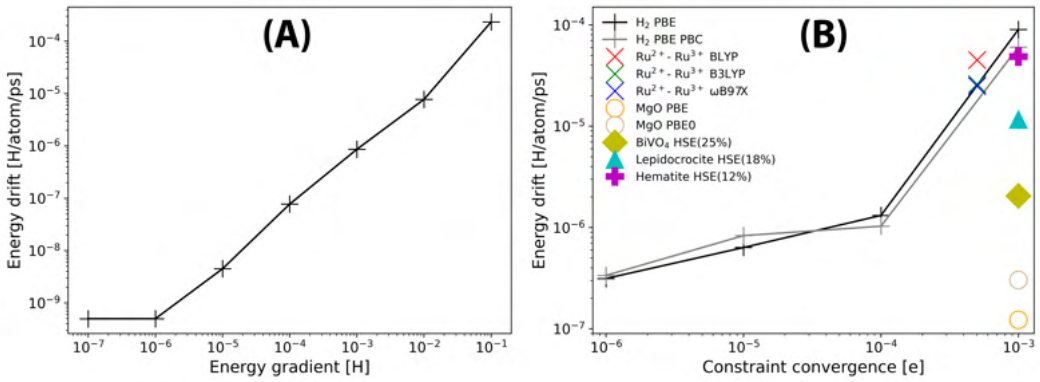

Figure 5.4: (A) Total energy conservation in DFT-MD for the hydrogen dimer H_2^+ as a function of the wavefunction convergence. (B) Total energy conservation in CDFT-MD as a function of the constraint convergence, where the grey and black markers represent H_2^+ CDFT-MD calculations in vacuum performed with and without periodic boundary conditions. Cross markers represent Ru^{2+}-Ru^{3+} CDFT-MD calculations in aqueous solution with BLYP (red), B3LYP (green) and ωB97X (blue). Cyan triangle marker represents lepidocrocite CDFT-MD with an electron hole, orange circle marker represents MgO CDFT-MD calculations with a defect separation of 6 Å and yellow diamond marker represents $BiVO_4$ CDFT-MD with an excess electron.

loop, different energies and forces could be obtained breaking time reversibility. The use of wavefunction extrapolation for the DFT loop and Lagrange multiplier extrapolation for the CDFT loop further exacerbate this problem [165, 166].

The hydrogen dimer H_2^+ presents one of the simplest benchmarks for examining energy convergence, performed in vacuum for a temperature of 300 K in the NVE ensemble with the PBE functional. Fig. 5.4 shows the average drift of the conserved energy for both DFT-MD as a function of the SCF convergence criterion, and CDFT-MD as a function of the constraint convergence. The constraint is defined as a charge difference of N_c=0.5e between the two hydrogen atoms. The resultant energy drift is less than 1×10^{-6} H/atom/ps for a constraint convergence of $1 \times 10^{-6}e$, the same as found in CPMD calculations for this system [33]. For unconstrained DFT-MD of H_2^+ the energy drift is negligible for the chosen DFT convergence of 1×10^{-5}, less than 1×10^{-8} H/atom/ps, and therefore the observed energy drift is introduced through the use of CDFT.

On average, the CDFT-MD calculations presented in this work are a factor of 3 times more expensive than corresponding DFT-MD calculations, consistent with

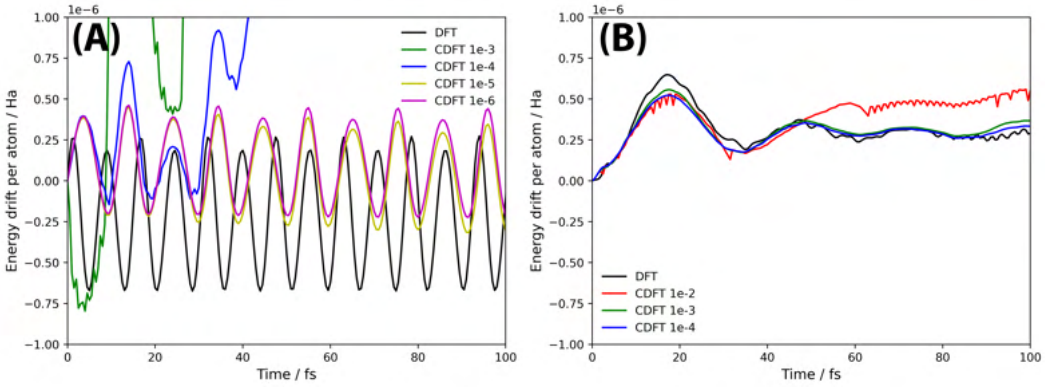

Figure 5.5: Drift of the conserved energy per atom as a function of time for CDFT-MD simulations for (A) a hydrogen dimer H_2^+ and (B) solid MgO with a defect separation of 6 Å with the PBE functional.

other CDFT implementations [33]. This additional cost is introduced by the CDFT SCF loop, with around 2-3 additional SCF cycles per MD step.

5.2.2.2 Excess electrons and holes in oxide materials

Also included in Fig. 5.4 is the energy drift for CDFT-MD of MgO with a defect separation of 6 Å, constraining the charge difference over the defects sites as described in Section 5.2.1.2. Likely as a result of the well defined oxygen defects with large reorganisation energies, even for a loose constraint convergence of $1 \times 10^{-3} e$ total energy conservation below 1×10^{-6} H/atom/ps is achieved for both PBE and PBE0-TC-LRC CDFT-MD. Fig. 5.5 shows the drift of the conserved energy as a function of time for different values of the constraint convergence for both the hydrogen dimer H_2^+ and MgO CDFT-MD with the PBE functional.

Energy drifts for CDFT-MD calculations for three further systems are shown in Fig. 5.6: an excess electron in bismuth vanadate ($BiVO_4$) [167], an electron hole in lepidocrocite ($\gamma-FeOOH$) [103] and an electron hole in hematite ($\alpha-Fe_2O_3$) [103, 104]. The HSE06 functional is used for all systems, with the percentage of Hartree-Fock exchange (HFX) optimised for each material: 25% for bismuth vanadate, 18% for lepidocrocite and 12% for hematite (see Chapter 3). The bismuth vanadate calculations are for a 1x2x1 supercell, the lepidocrocite calculations are for a 3x1x3 supercell and the hematite calculations are for a 2x2x1 supercell.

For each system, the electron or electron hole polaron is localised on a single

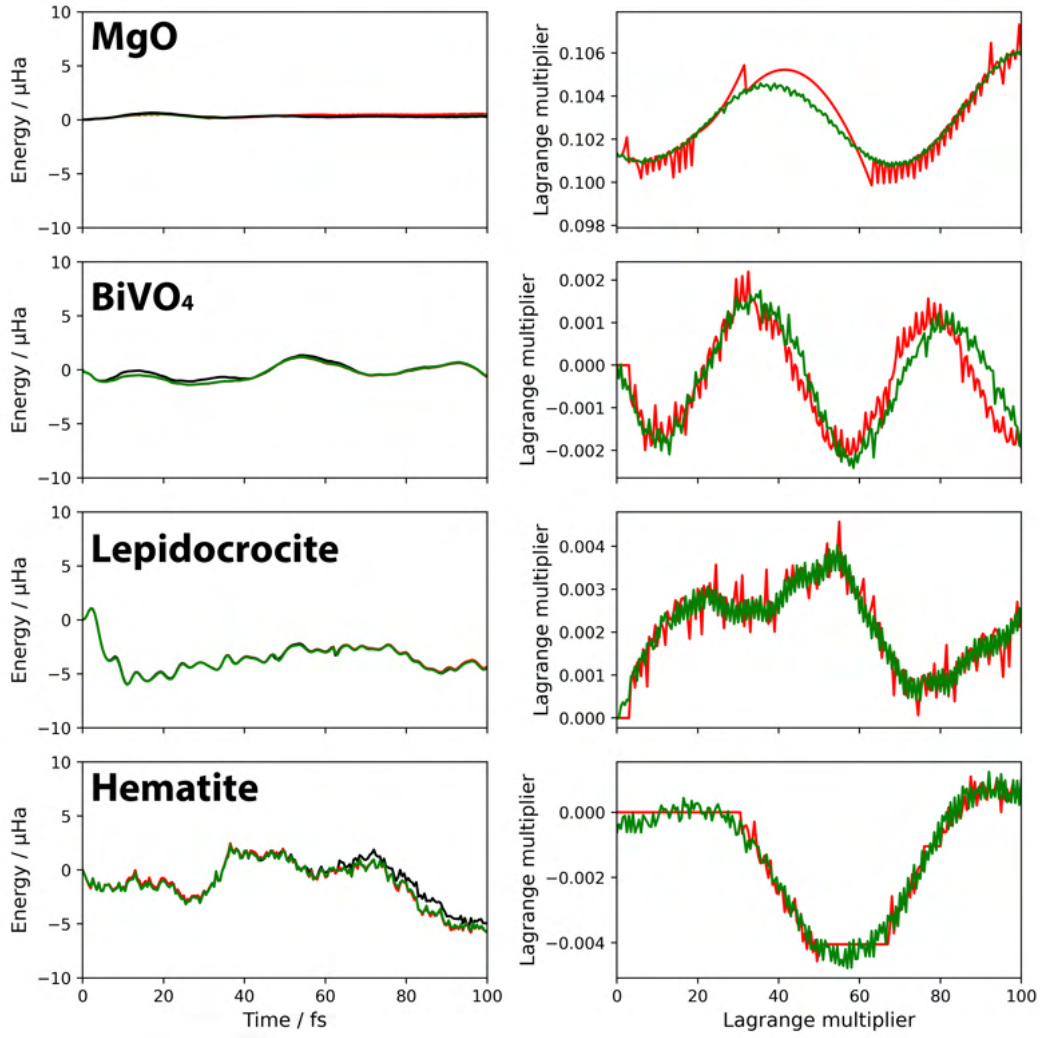

Figure 5.6: Drift of the conserved energy per atom as well as the Lagrange multiplier for CDFT-MD calculations performed for: solid MgO with a defect separation of 6 Å with the PBE functional, a hole polaron in lepidocrocite with HSE06(18%), an electron polaron in bismuth vanadate $BiVO_4$ with HSE06(25%) and a hole polaron in hematite with HSE06(12%). Importantly, the use of CDFT-MD introduces negligible additional energy drift.

atom as indicated by a large change in spin moment from Hirshfeld analysis. As such, I use a spin constraint to constrain the spin moment of the atom where the polaron localises to the spin moment of the geometry optimised charged ground state: 0.91 for the vanadium atom in bismuth vanadate, -3.59 for the iron atom in lepidocrocite and -3.29 for the iron atom in hematite. Figure 5.6 compares the drift of the conserved energy as well as the value of the Lagrange multiplier as a function of time for these systems.

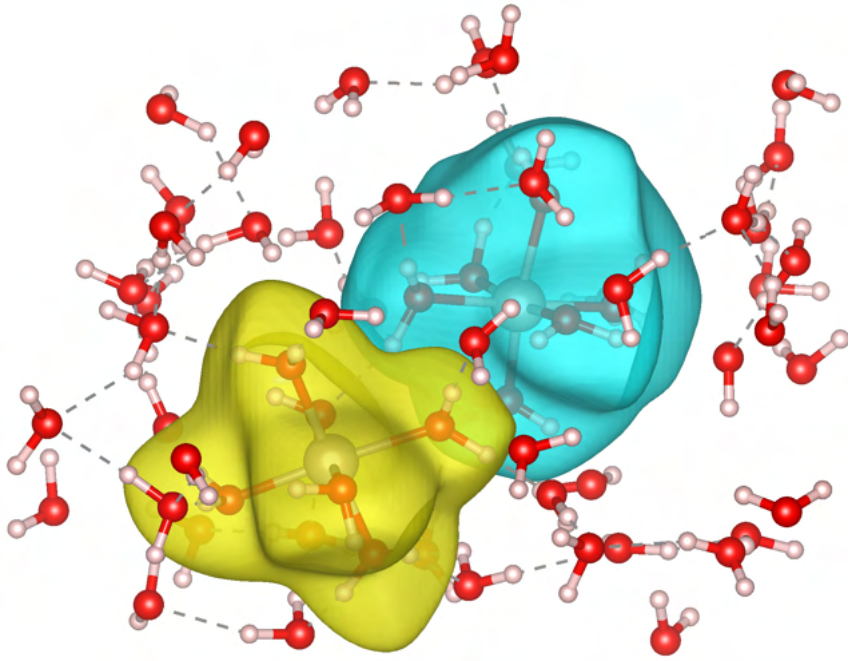

Figure 5.7: CDFT-MD of Ru^{2+}-Ru^{3+} in aqueous solution. An isosurface of the weight function (Eq. 2.19) is shown, where the electron donating group $Ru^{2+}(H_2O)_6$ is shown color coded yellow and the electron accepting group $Ru^{3+}(H_2O)_6$ is shown color coded blue. The bonds between the two Ru ions and the 6 water molecules in their first solvation shell are shown explicitly.

5.2.2.3 Ru^{2+}-Ru^{3+} in aqueous solution

For an example of condensed phase CDFT MD, I choose the previously studied Ru^{2+}-Ru^{3+} electron self-exchange in aqueous solution [33]. This is arguably one of the simplest electron self-exchange reactions in aqueous solution. Both Ru ions are low-spin and coordinated by 6 water molecules in an octahedral geometry. The most significant difference between aqueous Ru^{2+} and Ru^{3+} are the Ru-O bond lengths, around 0.08 Å shorter in the oxidised state [168].

Starting from the same initial structure from classical MD as the reference CPMD calculations [33], with two Ru ions and 63 water molecules, 1 ps of DFT-MD equilibration is performed with a timestep of 0.96 fs in the NVT ensemble with a Nose-Hoover thermostat at 300 K, and a fixed Ru-Ru distance of 5.5 Å. Where possible I use the same computational setup as the calculations in CPMD [33, 169, 170], including use of the BLYP functional [171, 172]. A charge difference constraint of N_c=1e is defined between the electron donating and accepting groups, chosen as

the Ru ion and the 6 water molecules in the first solvation shell: $Ru^{2+}(H_2O)_6$ for the electron donating group and $Ru^{3+}(H_2O)_6$ for the electron accepting group. The constraint is converged until the residual error is less than $5 \times 10^{-4}e$. An isosurface of the weight function (Eq. 2.19) is shown in Fig. 5.7.

The total linear drift of the conserved energy is shown in Fig. 5.4, for both DFT-MD and CDFT-MD. The use of CDFT introduces minimal additional energy drift, with only a small increase from 4.0×10^{-5} H/atom/ps to 4.5×10^{-5} H/atom/ps. While this energy drift is reasonably large, it is smaller than that found in CPMD calculations of 9.7×10^{-5} H/atom/ps [33].

Following 1 ps of CDFT-MD equilibration, I find that the average absolute charge for the electron donating group $Ru^{2+}(H_2O)_6$ is 0.47e and the electron accepting group $Ru^{3+}(H_2O)_6$ is 1.47e. Only the charge difference between the two groups is constrained to 1, and as such the absolute charges are free to vary during the dynamics. These average charges are similar to those found from CPMD calculations, 0.52e and 1.52e [33]. The remaining charge of 3.06e (2.96e from CPMD) is delocalised over the solvent.

While the average charges of the electron donating and accepting groups are similar between the CP2K and CPMD calculations, the geometries are different. For CP2K CDFT-MD the Ru-O bond lengths are on average 0.086 Å shorter in the oxidised state $Ru^{3+}(H_2O)_6$ than $Ru^{2+}(H_2O)_6$, in comparison to only 0.02 Å shorter for CPMD CDFT-MD [33]. X-ray diffraction experiments performed on isolated ions in solution found that the average Ru-O bond lengths were 0.08 Å shorter in the oxidised state [168], consistent with unconstrained calculations performed in CPMD [169, 170]. However, without any experimental data available for an ion-ion distance of 5.5 Å it is not possible to determine which of the CPMD or CP2K CDFT-MD geometries are more accurate.

The CDFT simulation can be used to calculate the reorganisation free energy for electron transfer between the two Ru ions. For self-exchange and assuming linear response, it is simply equal to the thermal average of the vertical energy gap,

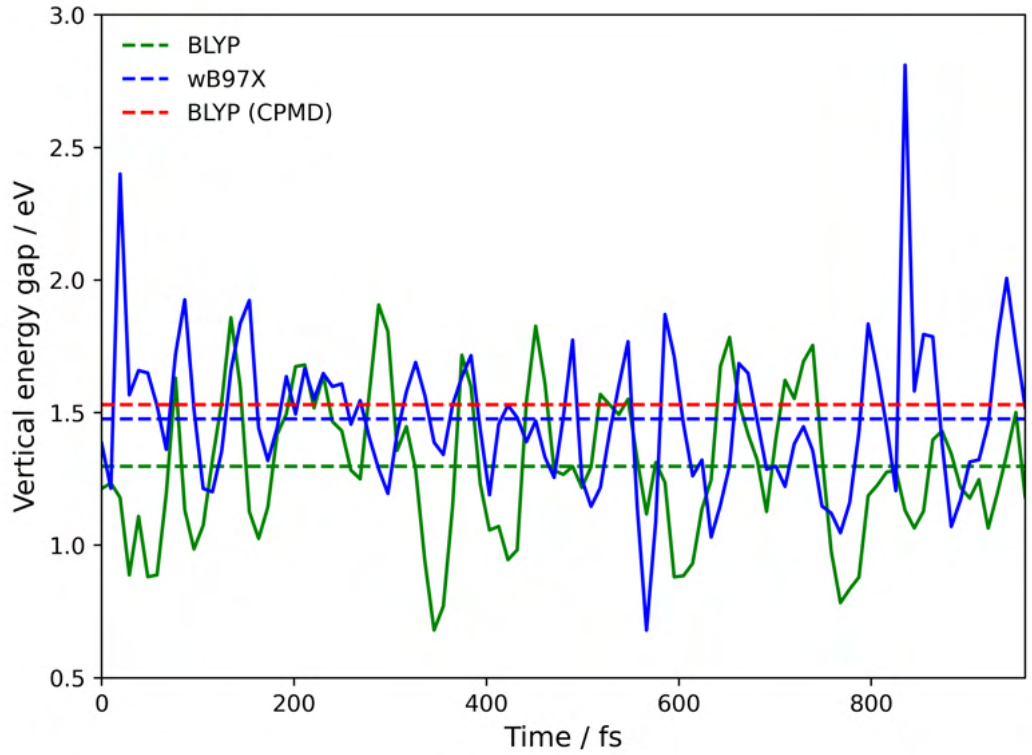

Figure 5.8: Vertical energy gap for the electron self exchange reaction of Ru^{2+}-Ru^{3+} in aqueous solution. Single point calculations are performed on 100 equally spaced structures sampled from 1ps of CDFT-MD. The green dotted line shows the BLYP average of 1.30 $\pm$ 0.03 eV, the blue line the ωB97X average of 1.48 $\pm$ 0.08 and the red dotted line the CPMD value from Oberhofer et al. of 1.53 $\pm$ 0.06 eV [33].

$$\lambda = \langle \Delta E \rangle_A, \tag{5.10}$$

where $\Delta E = E_B - E_A$ and the average is taken along a CDFT trajectory in diabatic state A. The vertical energy gap is sampled with 100 equally spaced single point calculations, shown in Fig. 5.8, with an average $\langle \Delta E \rangle_A$=1.30 $\pm$ 0.03 eV, slightly smaller than the CPMD calculated value of 1.53 $\pm$ 0.06 eV [33]. The error of the average due to the finite length of the trajectory is calculated from the difference of the vertical energy gap obtained from the first and second half of the trajectory.

With the increasing efficiency of computer codes and platforms it is now possible to perform hybrid CDFT calculations on system sizes that would have been out of reach of the earlier CPMD work [33]. In particular, I am able to perform CDFT-MD

Functional	Average Ru-O / Å	Energy gap / eV
BLYP	2.18, 2.10	1.30 ± 0.03
B3LYP	2.18, 2.08	1.42 ± 0.18
ωB97X	2.17, 2.07	1.48 ± 0.08
BLYP [33]	2.15, 2.13	1.53 ± 0.06

Table 5.4: Average Ru-O bond lengths and vertical energy gap (Eq. 5.10) for the electron self exchange reaction of Ru^{2+}-Ru^{3+} in aqueous solution. The average of the six Ru^{2+}-O and Ru^{3+}-O bond lengths are calculated following 1ps of CDFT-MD equilibration. The error of the vertical energy gap (Eq. 5.10) is calculated from the difference of the vertical energy gap obtained from the first and second half of the trajectory.

with B3LYP [173] and the long-range corrected hybrid functional ωB97X [174]. Following CDFT-MD equilibration I find only a small increase in the average absolute charges of the $Ru^{3+}(H_2O)_6$ and $Ru^{2+}(H_2O)_6$ compared to charges obtained from BLYP CDFT-MD: +0.08e for B3LYP and +0.13e for ωB97X. The remaining charge of 2.92e and 2.82e remains delocalised over the solvent. Therefore, even these hybrid functionals are unable to prevent spurious charge delocalisation across the solvent. Table 5.4 shows the average Ru-O bond lengths and vertical energy gap for BLYP, B3LYP and ωB97X. Similar to the charge, the reorganisation energy increases only slightly: +0.12 eV for B3LYP, and +0.18 eV for ωB97X.

The reorganisation energy calculated for the electron self-exchange reaction accounts for the two Ru-hexahydrates and the 51 water molecules solvating the electron transfer complex, neglecting the effects of higher solvation shells and the bulk solvent. Blumberger et al. [175] calculated a finite size correction from classical MD with extrapolation to the limit of infinite dilution, resulting in a correction term of 0.09 eV [33]. As such, the reorganisation free energy of the infinitely diluted system for the BLYP, B3LYP and ωB97X functionals is: 1.30+0.09=1.39 eV, 1.42+0.09=1.51 eV and 1.48+0.09=1.57 eV. Comparison to experiment is challenging as a direct experimental measurement of the reorganisation free energy is not available, and the experimental Ru-O bond lengths for the electron transfer complex at a distance of 5.5 Å are not known. A continuum study [176] with a Ru-Ru distance of 6.5 Å reported a reorganisation free energy of 1.95 eV, which fits well the experimental rate constant [177], and is expected to decrease to 1.75 eV for a Ru-Ru distance of

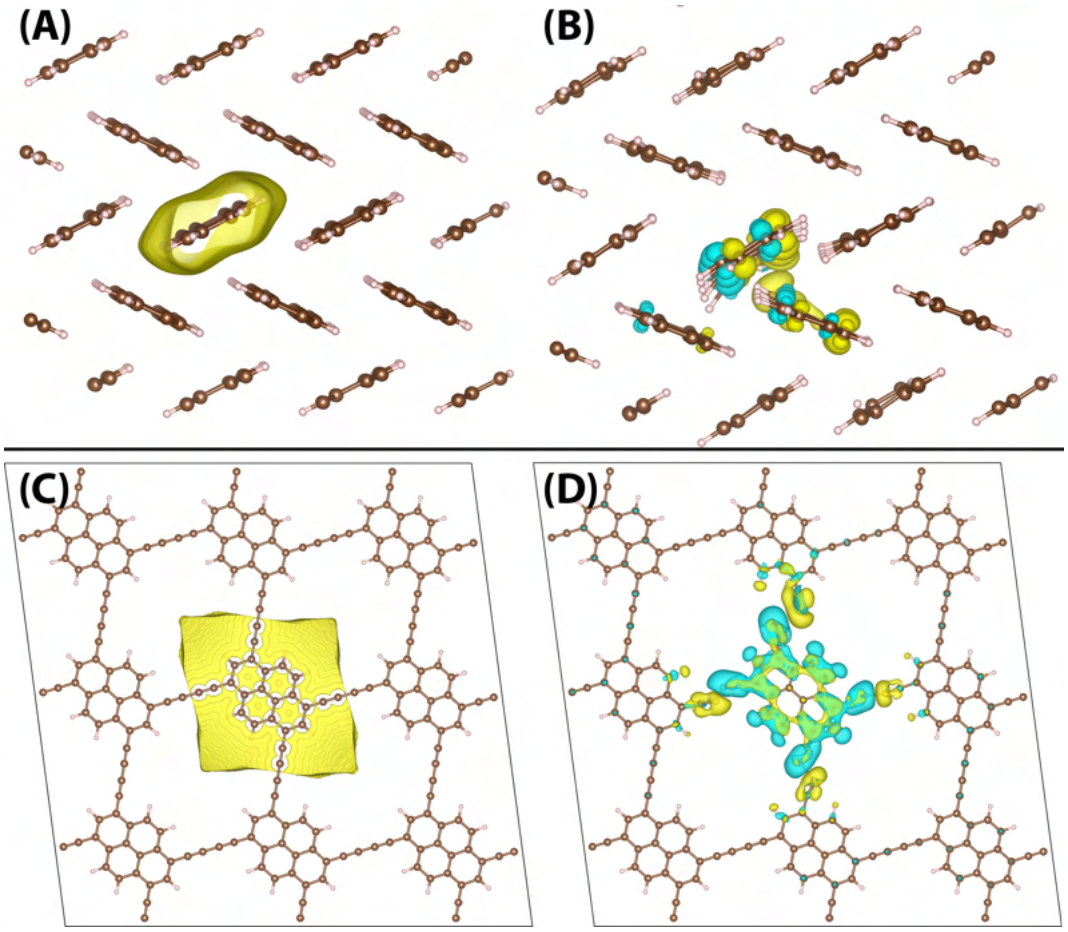

Figure 5.9: Hole transfer in two organic semiconductors: (A, B) a 3x2x1 supercell of pentacene and (C, D) a 3x3 supercell of a pyrene 2D covalent organic framework (pyrene-COF). The left column (A, C) shows the CDFT weight function (Eq. 2.19), while the right column shows the spin density (B) and excess electron density (D) following a 4 steps of CDFT geometry optimisation. In an attempt to stabilise the excess hole, the pentacene molecule moves closer to its highest coupling neighbour while the pyrene-COF forms cyclic structures between the acetylene linkers.

5.5 Å [33]. In addition, under a number of assumptions, an experimental value of 2.0 eV has been reported [177].

5.2.3 Charge transfer in organic crystals

A useful application of CDFT in organic semiconductor research would be to calculate reorganisation energies for charge transfer in organic semiconductors, including the full outer-sphere contribution from the periodic crystal which is usually presumed to be small and therefore neglected. However, it would be useful to check this assumption from case to case. Refined values for reorganisation free energy

would improve the accuracy of the parametrisation of charge transport simulations including e.g. charge hopping and non-adiabatic molecular dynamics [115, 178, 179].

Fig 5.9 shows the weight functions for hole transfer in two organic semiconductors: a 3x3 supercell of a pyrene 2D covalent organic framework (pyrene-COF) [180], and a 3x2x1 supercell of pentacene [181]. For both systems, the electron donating and accepting regions are defined as adjacent units or molecules. The reorganisation energy for hole transfer in these systems should be calculated using Eq. 5.8, as the vertical energy gap at the minimum of a diabatic state. Geometry optimising the diabatic state with PBE or HSE06 for either system results in unphysical distortions and even bond breaking during CDFT geometry optimisation of the donor and acceptor groups. This shows that the localisation of a full charge on a single COF unit or pentacene molecule within a crystalline environment does not correspond to a stable local minimum on the potential energy surface. Thus I conclude that fully localised polarons do not exist in these materials and cannot be enforced using CDFT. In this respect I note that previous non-adiabatic molecular dynamics simulations showed that polarons in crystalline pentacene are delocalized over 18 molecules on average at room temperature [179]. At 0 K, corresponding to the present CDFT optimisations, the charge will occupy the fully delocalized state at the top of the valence band. The physical reason for the non-existence of fully localised polaronic states is that reorganisation energy is not sufficiently large in these materials compared to electronic couplings to support fully localised states, in stark contrast to, e.g. the F centres in MgO system (Section 5.2.1.2) and the Ru^{2+}-Ru^{3+} self-exchange reaction (Section 5.2.2.3).

5.2.4 Reliability of CDFT

CDFT is a powerful method for calculation of ET parameters, but as shown in Section 5.2.3, not any arbitrary charge constrained state can be constructed this way. To examine this further, I performed a experiment where I deliberately applied an unphysical constraint to the Ru^{2+}-Ru^{3+} in aqueous solution (Section 5.2.2.3). Removing the 5.5 Å Ru-Ru distance constraint and switching to the NVE ensemble, I set charge constraint of 0e for the electron donating group $Ru^{2+}(H_2O)_6$ resulting

in an average Ru^{2+} charge of +0.36e and an average $(H_2O)_6$ charge of -0.36e. It is clear that such a constraint is far from the adiabatic ground state, reaching an energy drift of 2×10^{-4} H/atom after 300 fs. The constraint is fulfilled and the forces on the atoms are continuous in time, and decreasing the timestep by an order of magnitude does not reduce this energy drift. This is attributed to the use of CDFT to form an electronic state that the underlying functional is not able to adequately describe, despite the well behaved convergence of both the DFT and CDFT SCF loops. As for the CDFT geometry optimisation of organic molecules in Section 5.2.3, this highlights that not any arbitrary charge constrained state can be obtained using CDFT.

A useful diagnostic tool to identify states that the DFT functional is not able to adequately describe is the integrated absolute spin density (IASD),

$$\int_{\Omega} (\rho_{\alpha}(\mathbf{r}) - \rho_{\beta}(\mathbf{r}))\mathrm{d}\mathbf{r}, \tag{5.11}$$

where $\rho_{\alpha}(\mathbf{r})$ and $\rho_{\beta}(\mathbf{r})$ are the electron densities of the alpha and beta spin channels. For a system with a single excess charge, the IASD should have a value of 1. Small deviations are to be expected, for example the CDFT geometry optimisations of MgO in Section 5.2.1.2 have an average IASD of 1.05, and the CDFT-MD of Ru^{2+}-Ru^{3+} in Section 5.2.2.3 have an average IASD of 1.09.

While neutral DFT calculations for the pyrene-COF and pentacene crystal in Section 5.2.3 have an IASD of 0.00 as expected, with the addition of an electron hole this increases to 1.18 for the pyrene-COF and 1.33 for the pentacene crystal. Using CDFT to localise the electron hole fully on a single unit or molecule raises the IASD to 1.46 (+0.28) and 1.55 (+0.22), with further increases during CDFT geometry optimisation. These large values of IASD indicate the breaking of electron pairs, as the DFT functional is not able to adequately describe the charged states. This is particularly problematic for CDFT, where the transfer of fractions of electrons from donor to acceptor can lead to electronic couplings that do not decay exponentially with distance [182]. In the context of this work, I attribute symmetry breaking and the transfer of fractional electrons to the formation of an unphysical diabatic state

that the DFT functional is not able to adequately describe.

I note that the IASD does not distinguish between the transfer of fractional electrons within the same unit and between the donor and acceptor, the latter which is particularly problematic for CDFT. Mavros and Van Voorhis have recently proposed an alternative metric [182] which directly uses the difference between the electron donor and acceptor densities, and therefore more specifically targets the transfer of fractional electrons between the donor and acceptor. However, similar to the IASD their metric has no clear cutoff, and has been shown to provide both false positives and false negatives in identifying the whether calculated electronic couplings will decay exponentially with distance. As such I believe that more research is needed to better understand the problem of fractional electrons within the context of CDFT, and the effect this may have on the reliability of calculated electron transfer parameters.

5.3 Conclusion

In this Chapter I have provided an extension to CDFT in a popular DFT package CP2K, implementing the necessary force terms which arise from a constraint based on Hirshfeld partitioning of the electron density. The previously used Becke partitioning is prone to predict qualitatively incorrect atomic charges, as a result of dividing space equally among all atoms.

I have verified and benchmarked this new implementation against systems previously studied in a plane-wave implementation of CDFT, showing good agreement for both geometry optimisation and molecular dynamics for: electron tunnelling between oxygen defects in MgO [34], and electron self-exchange in aqueous Ru^{2+}-Ru^{3+} [33]. With the increasing efficiency of computer codes and platforms it is now possible to perform hybrid CDFT calculations on system sizes that would have been out of reach of the earlier CPMD work [33]. In particular, I am able to perform CDFT-MD for electron transfer reactions in the condensed phase where both solute and solvent are treated at the hybrid or long-range corrected hybrid DFT level.

Consistent with previous work [182], I find that an IASD markedly larger than 1 is an indicator of systems for which CDFT calculations can be unreliable.

With the exception of these pathological cases, I find that CDFT is a powerful tool for the calculation of electron transfer parameters at a reasonable computational cost. I expect the method to become valuable also for the simulation of electron transfer reactions across interfaces between different semiconductors or between semiconductors (e.g. oxides) and liquid solutions (e.g. water), thus becoming part of the toolbox for first principles electrochemistry [155].

Chapter 6

Polaron structure at the hematite/liquid water interface

The calculations of charge transport in bulk hematite in Chapters 3-4 set the scene for similar calculations at the hematite/liquid water interface. In particular, it will be important to understand if and how the presence of water at the interface changes the picture obtained for the bulk material. Such investigations could help refine models, and resolve ongoing questions, about rate-limiting transport processes governing photocatalytic water splitting efficiency at hematite/water interfaces [11, 154].

In this Chapter I first discuss the computational setup of the hematite/liquid water calculations in Section 6.1, before discussing the results for both the hole polaron in Section 6.2.1 and for the electron polaron in Section 6.2.2. This work is currently unpublished, and there is still much to understand about the charge transport mechanisms and how these differ to bulk hematite. However, I will discuss the early results of this work as well as some of the challenges in regards to trivial crossings (Section 6.3) during the molecular dynamics simulation and the problem of charge delocalisation across the solvent (Section 6.4). These calculations build upon the work of Dr Guido Falk von Rudorff who carried out DFT-MD calculations of the neutral interface, and Dr Philipp Schienbein who subsequently trained a neural network potential for the neutral interface. I note that while Dr Philipp Schienbein was responsible for running the calculations in Section 6.2, I led the investigation and performed all analysis.

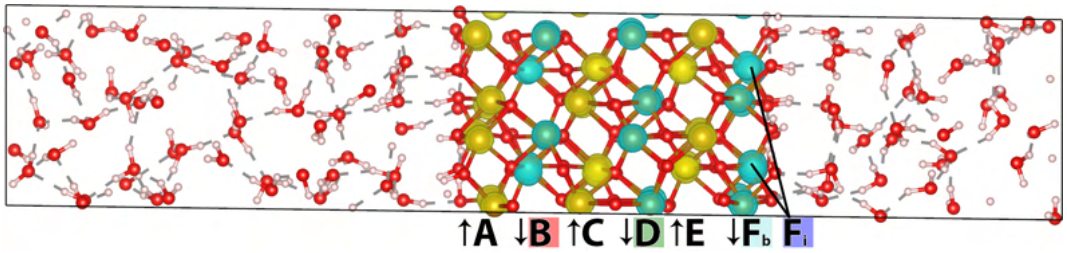

Figure 6.1: Neutral spin density for the hematite/water interface. Oxygen terminated hematite c-cut (001) in contact with 30 Å liquid water, prepared by Dr Guido Falk von Rudorff. The Fe-bilayers are color coded according to their spin and labelled A-F, where the interfacial 'F' bilayer is composed of two rows: 'F_b' which is closer to the bulk-like hematite, and 'F_i' which is closer to the interface.

6.1 Computational setup

The calculations of polaron structures and charge transport at the hematite/liquid water interface in this Chapter builds directly upon the previous work by Dr Guido Falk von Rudorff [30, 97, 99, 100], who carried out extensive DFT-MD calculations of the neutral interface. As such, please refer to his work for a full description of the interface and corresponding computational setup which I will only briefly summarise.

Figure 6.1 shows the neutral spin density for the system prepared by Dr Guido Falk von Rudorff, composed of a 2 x 2 x 1 hematite slab in contact with 30 Å liquid water. A mutli-stage system preparation scheme combining both classical MD and DFT-MD with HSE06(12%) was used to set up the system [97]. The oxygen terminated hematite c-cut (001) was chosen as the structure of this surface is known experimentally [183–185]. The 2 x 2 x 1 supercell was determined to be an appropriate compromise between accuracy and computational cost, and as shown in Chapter 3 there is little difference in polaron structure between the 2 x 2 x 1 and larger supercells.

With a total of six Fe-bilayers, the 2 x 2 x 1 hematite slab has three parallel Fe-bilayers where the electron or hole polaron may localise. These are labelled in Figure 6.1 as the 'B' layer (1 layer away from the surface), the 'D' layer (bulk-like) and the 'F' layer (at the surface).

I note that while the computational setup in this work and the work of Rudorff

and co-workers is largely consistent, there is a slight increase in the convergence criteria in order to ensure consistent convergence for the charged systems. The wavefunction gradient was increased from 1×10^{-5} to 1×10^{-6} H, and the planewave cutoff was increased from 400 to 600 Ry (as discussed in Chapter 3.1). These changes make very little difference to the neutral simulations, while are essential for the systematic convergence of the charged simulations. In addition, for molecular dynamics the ensemble was changed from NPT to NVT, avoiding any complications of a flexible cell during the MD. A final difference, that does not effect the dynamics, is the implementation of Hirshfeld charge partitioning. Rudorff and co-workers used an implementation of Hirshfeld partitioning where the weight function was constructed using covalent radii, rather than the promolecular density, and therefore my calculated charges and spin moments are different.

In order to better understand polaron formation and any dependence on the starting geometry, working together with Dr Philipp Schienbein we have performed 10 statistically independent DFT-MD simulations starting from completely different nuclear configurations. These configurations were drawn from one long simulation of the neutral hematite/liquid water interface performed using a machine learning (ML) model by Dr Philipp Schienbein [186]. This ML model is based on the recently introduced committee neural network potentials (c-NNP) [187], and is likely the first such application to a transition metal oxide/liquid water interface. The advantage of a ML model is that it is is able to significantly speed up the simulations by several orders of magnitudes, while keeping the same accuracy. This ensures that the starting nuclear geometries are very different, and represent a statistical ensemble.

I note that as an alternative to expensive DFT-MD I have considered geometry optimisation of the hematite slab, with frozen water molecules. While I found spontaneous polaron formation, I also found that these structures were iso-enegetic with delocalised polarons ($\Delta E < 5$ meV). This highlights the importance of the effect of the solvent, and therefore I do not consider geometry optimisation of the hematite/liquid water interface further in this work.

Given that the electron hole is generally of greater interest due to the use of

hematite as a photoanode material, and the higher computational cost for calculations of the excess electron, in this Chapter the primary focus will be DFT-MD of the electron hole at the hematite/liquid water interface.

6.2 Results

6.2.1 Hole polaron

While in bulk hematite the two distinct planes of iron atoms that comprise an Fe-bilayer are equivalent, at the hematite/liquid water interface they are not due to the asymmetry of the interface. One row of the bilayer ('F_i') is closer the water interface, while the other ('F_b') is closer to the bulk-like hematite. As a result, the geometry of the hole polaron will differ depending on which row of the bilayer localisation occurs.

Figure 6.2 shows the spin moment of all Fe atoms of the three Fe-bilayers where the hole polaron may localise, for 10 statistically independent DFT-MD simulations. For each trajectory, the hole relaxes from a delocalized band state to a polaron localised on a single iron atom. In 8/10 of the trajectories the hole polaron localises onto the 'F' bilayer, with the remaining two trajectories on the 'B' layer. This represents the high probability of the hole polaron to localise at the interface, where the reorganisation energy is expected to be larger than bulk. As previously explored in Chapters 3-4, charge transport in hematite occurs within the same spin Fe-bilayers and therefore a polaron that localises onto the 'B' layer will become trapped, even if there is a lower energy state at the 'F' layer. The transport between different spin layers observed in Figure 6.2 is attributed to trivial crossings, a consequence of not propagating continuously the electronic state. See Chapter 6.3 for further discussion.

As an example, in trajectory 8 the hole polaron localises within 70 fs at the interface with an average spin moment of -3.35, very similar to the spin moment found for bulk hematite of -3.29 (shown as the dotted line in Figure 6.2). The decreased polaron spin moment at the interface is attributed to the interaction with the water, where polarisation results in an increase in both the charge and spin moment of the interfacial iron atoms even for the neutral state. As a result, the

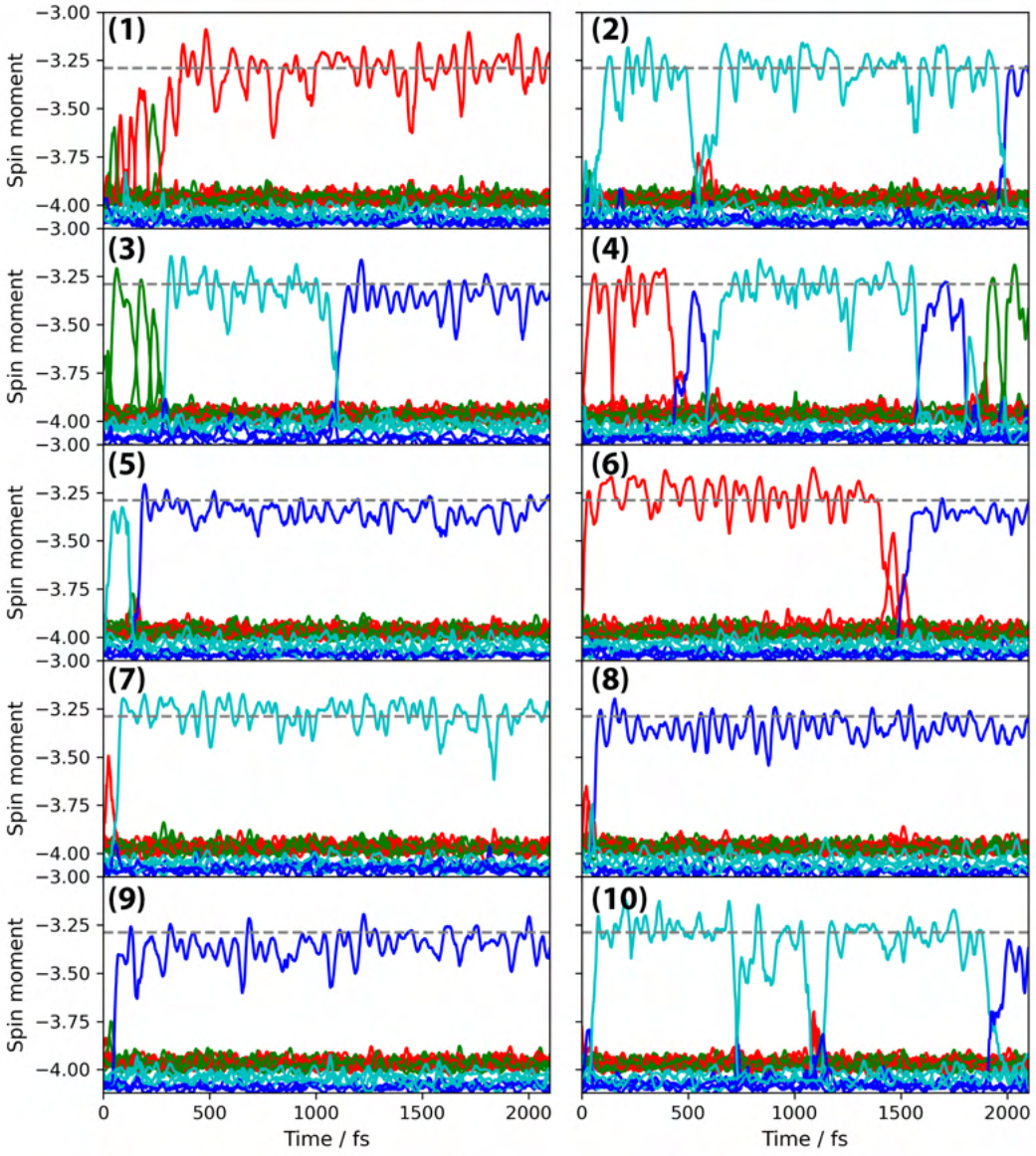

Figure 6.2: Hole polaron spin moment at the hematite/water interface. Spin moments of all iron atoms where the hole polaron may localise, shown for 10 statistically independent DFT-MD trajectories starting from completely different nuclear configurations. Red line refers to the 'B' Fe-bilayer, green line to the 'D' Fe-bilayer, light blue to the 'F_b' row of the F-bilayer and dark blue to the 'F_i' row of the F-bilayer. Dashed line shows the spin moment of the hole polaron from DFT geometry optimisation of bulk hematite. Refer to Figure 6.1 for layer labelling.

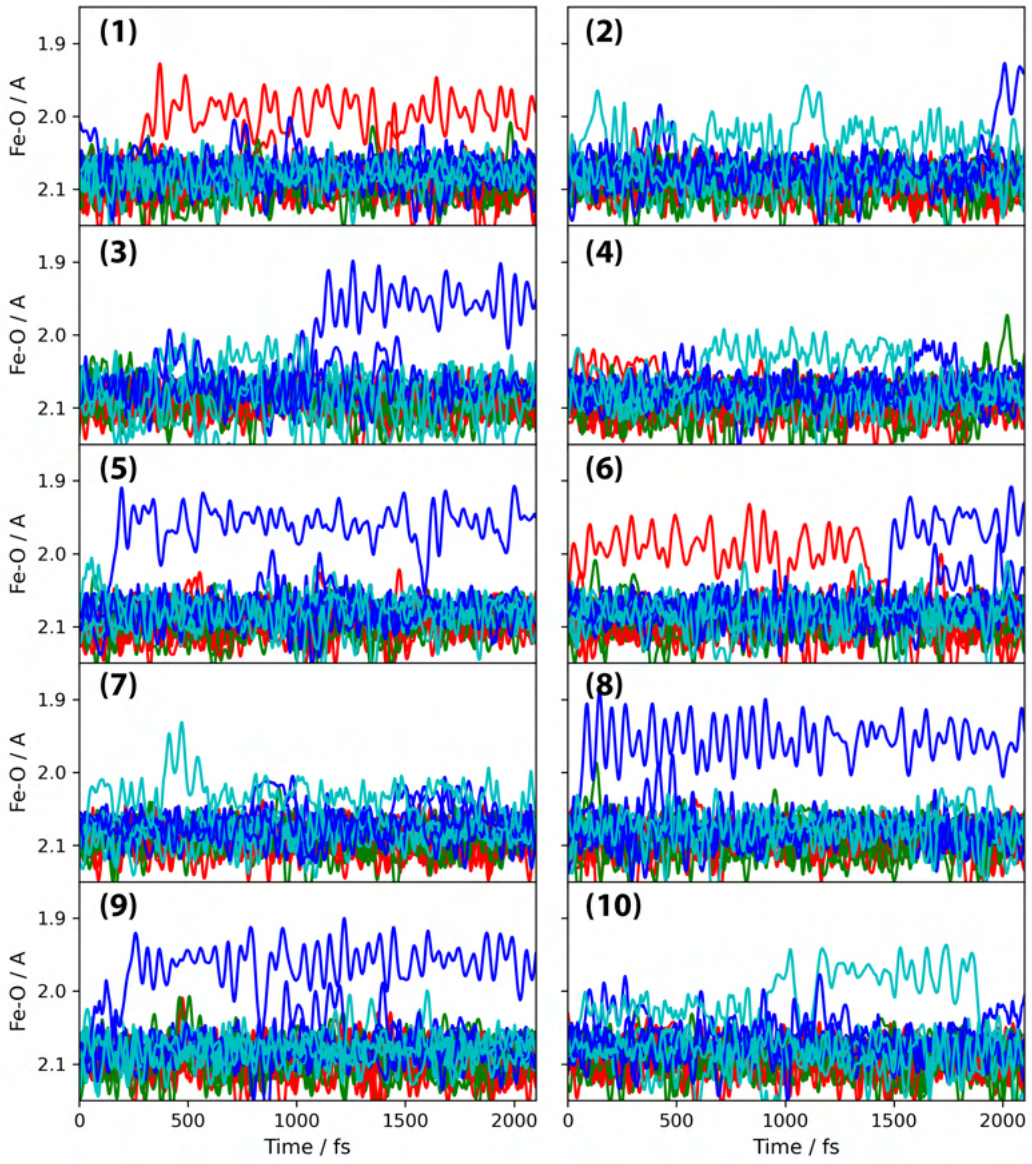

Figure 6.3: Hole polaron structure at the hematite/water interface. Average of the 6 first nearest neighbour Fe-O bonds for all iron atoms where the hole polaron may localise, shown for 10 statistically independent DFT-MD trajectories starting from completely different nuclear configurations. Red line refers to the 'B' Fe-bilayer, green line to the 'D' Fe-bilayer, light blue to the 'F_b' row of the F-bilayer and dark blue to the 'F_i' row of the F-bilayer. Refer to Figure 6.1 for layer labelling.

average spin moment of -3.97 for the bulk-like 'D' Fe-bilayer is decreased to -4.05 for the 'F_b' row and -4.09 for the 'F_i' row. Therefore, the change in spin moment upon localisation of the hole polaron of +0.74 is actually larger than that found for bulk hematite of +0.64. Nuclear relaxation of the polaron structure (Figure 6.3) continues until around 250 fs, resulting in an average Fe-O bond length of 1.95 Å. The change in bond lengths per Fe-O bond, accounting for the different bond lengths of the two Fe-bilayer rows, is -0.08 Å compared to -0.06 Å in the bulk hematite 2x2x1 supercell. As would be expected due to the increased reorganisation energy at the interface, both the change in spin moment and change in bond lengths are larger than for bulk hematite. For the remainder of the 2ps DFT-MD, the hole polaron remains localised on this iron atom.

A surprising feature in Figure 6.3 is that some hole polarons appear to be localised with only a very small change in geometry. Figure 6.4 explores this in further detail, showing examples of the polaron structure at the 'F_i' row and 'F_b' row of the Fe-bilayer. While the electronic structure is similar, the Fe-O bond lengths differ considerably. The polaron at the 'F_i' row has an average Fe-O bond length of 1.95 Å, while the polaron at the 'F_b' row has an average Fe-O bond length of 2.06 Å. Further, the tetragonal elongation found in bulk calculations of the hole polaron is far more pronounced for the 'F_i' row than the 'F_b' row, where only one of the Fe-O-H bond lengths decreases. This is likely due to the interaction of the hole polaron with the water, where the row of the bilayer closer to the water experiences a greater degree of polarisation and therefore stabilisation of excess charge.

Figure 6.5 shows an example of hole polaron hopping at the hematite/liquid water interface, with comparison to DFT-MD of bulk hematite. A significant difference compared to bulk hematite is that at the interface the initial and final states are not the same, and as such the spin moments are asymmetric in time. In addition, the time taken for hole polaron hopping at the interface is larger. The distance between the maxima in the spin moment for bulk hematite is around 40 fs, while for the hematite/liquid water interface the first spin moment maxima of -3.50 is at 50 fs and the equilibrated maxima of -3.28 occurs at 150 fs. This is likely due to the

rearrangement of the water molecules at the interface, which acts to stabilise the excess charge. These time periods are consistent with an Fe-O stretch (around 50 fs) [38], and multiple O-H stretches (around 10 fs) [188]. As there are only a total of 5 hops during the 20 ps of DFT-MD, more statistics will be required to investigate this effect further. In addition, it is unlikely that the 2 ps DFT-MD performed is sufficient to equilibrate the polaron fully at the interface.

While the hole polaron appears to localise with equal probability onto the 'F_i' and 'F_b' rows, nearly all hopping of the hole polaron in Figures 6.2-6.3 is from the 'F_b'to 'F_i' row. The only exception is a hopping in trajectory 10 from an 'F_b' Fe atom to another 'F_b' Fe atom at around 800 fs, which is the rare event of a second nearest neighbour hop and is likely a result of the non-equilibrium hole polaron. As no hops are observed from 'F_i' to 'F_b' this suggests that the hole polaron localised closer to the interface is more stable, consistent with the larger change in Fe-O bond lengths and therefore a larger reorganisation energy. With only 5 successful hops during 20 ps DFT-MD, more statistics is required to investigate this further. In future work it would be interesting to compare the hopping rates between the two rows of the Fe-bilayer, and to relate this to the orientation of the hydrogen atoms and the dipole of the solvent.

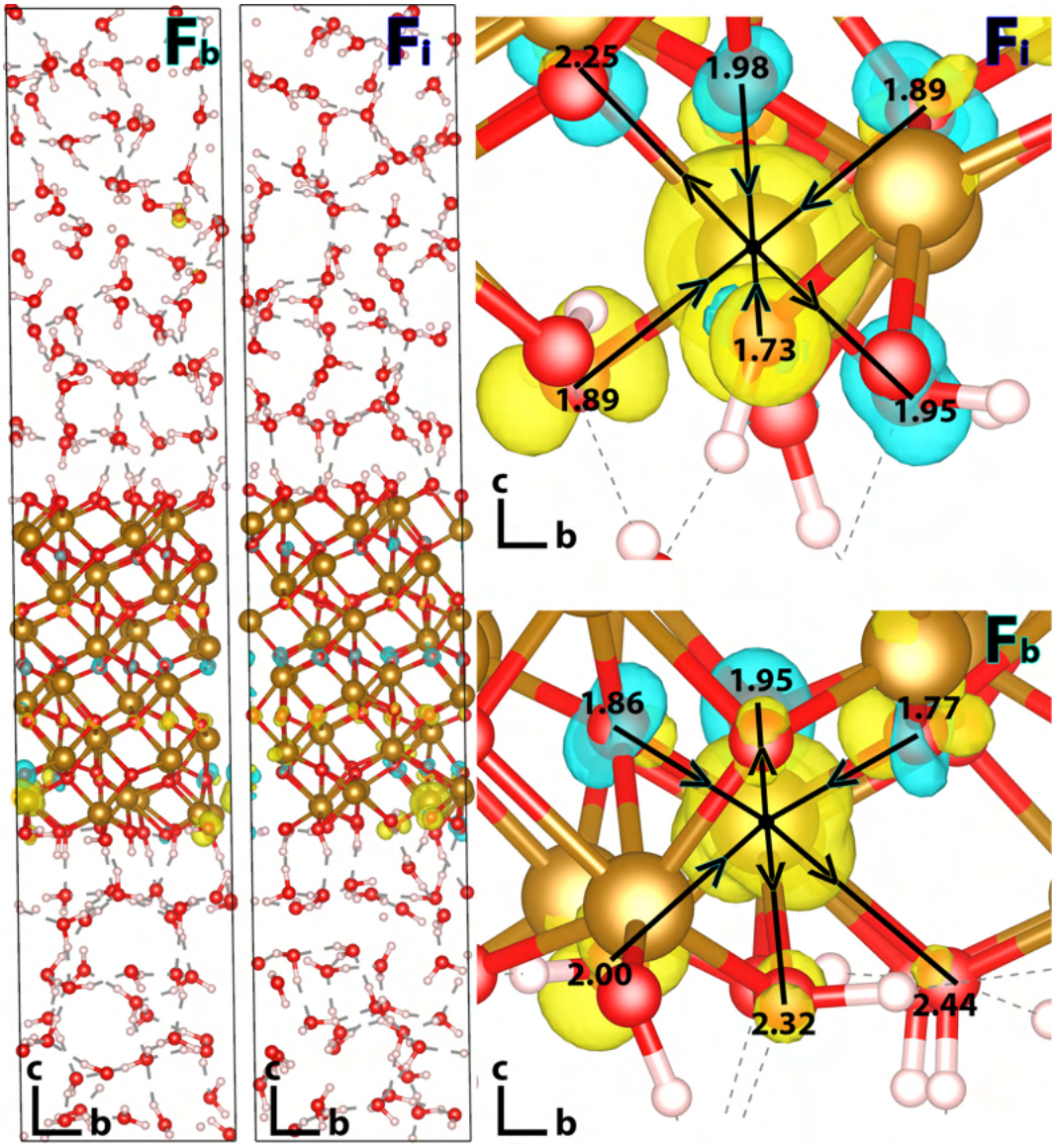

Figure 6.4: Hole excess spin density at the hematite/liquid water interface. The 'F_b' hole polaron corresponds to the final geometry of trajectory 7, with an average Fe-O bond length of 2.06 Å, while the 'F_i' hole polaron corresponds to the final geometry of trajectory 9, with an average Fe-O bond length of 1.95 Å. For comparison, the average Fe-O bond lengths for iron atoms where the hole polaron does not localise are 2.08 Å for both the 'F_b' and 'F_i' row. Both hole polarons have been localised on their respective iron atoms for 2 ps of DFT-MD, and therefore should be close to equilibrium. Bond lengths between the iron atom and bonded oxygen atoms are shown in Angstrom. Arrows show contraction and elongation of the Fe-O bonds with respect to their neutral bond lengths.

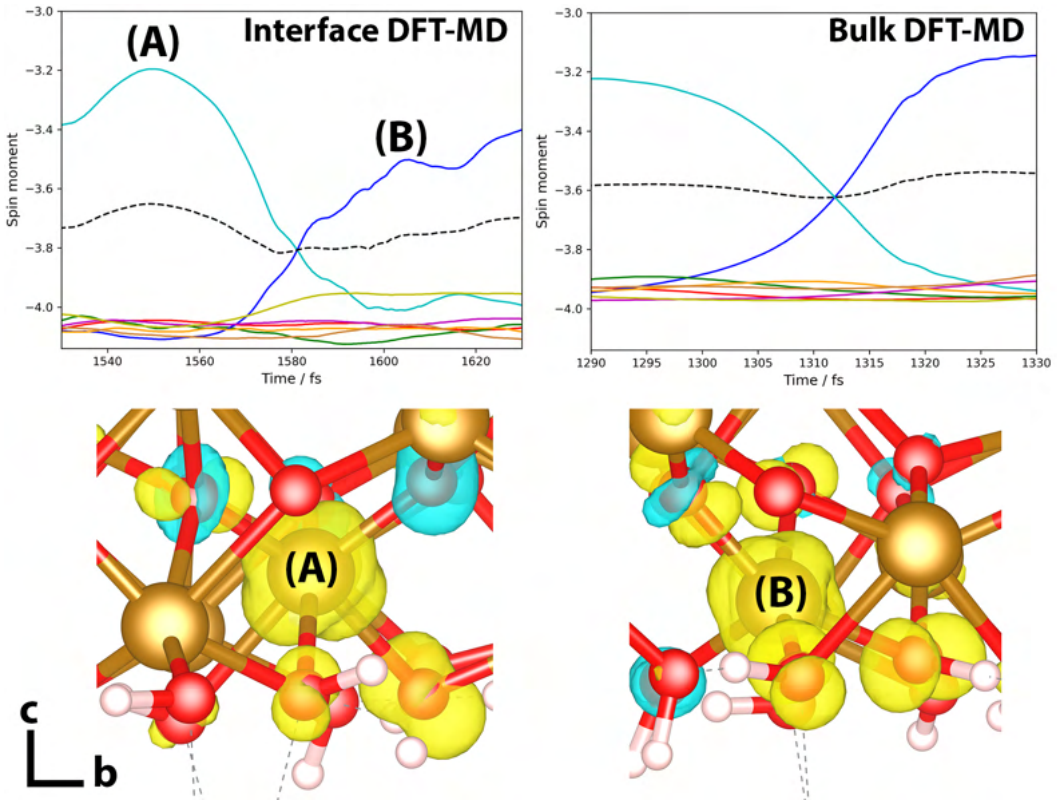

Figure 6.5: Hole polaron hopping during DFT-MD of the hematite/liquid water interface for trajectory 4 (top left) and bulk hematite (top right). Spin moments of all 8 atoms of the Fe-bilayer shown color coded, with the average spin moment of the two iron atoms where the hole polaron localises shown with a black dotted line. Notably, in bulk hematite the initial and final states are the same due to symmetry, which is broken at the hematite/liquid water interface.

6.2.2 Electron polaron

Figure 6.6 show a plot of the spin moment for all relevant iron atoms against time, demonstrating the weaker localisation of the 2-site delocalised electron polaron in comparison to the 1-site localised hole polaron. Similar to the hole polaron, for 8/10 trajectories there is localisation at the interfacial 'F' layer and the remaining 2/10 trajectories at at the 'B' layer.

The electron polaron delocalises across the two rows of an Fe-bilayer, and therefore the geometric complications found for the hole polaron structure do not apply to the electron polaron. Figure 6.7 shows the excess spin density of an electron polaron, very similar to that found in calculations of bulk hematite. The spin moment of the two iron atoms where the electron polaron is delocalised are -3.84 for the 'F_b' row and -3.89 for the 'F_i', corresponding to an increase in spin moment of +0.25 and +0.20, similar to that found for bulk hematite of +0.23.

The hopping of the electron polaron observed during the 2ps DFT-MD is for the shortest transfer distance only (e.g. (0,1)-(0,2) as described in Chapter 4), which is likely a result of the small 2 x 2 x 1 supercell. While the highest coupling was found for the next largest distance (e.g (0,2)-(1,6) as described in Chapter 4), this would require delocalisation of the electron polaron across the entire Fe-bilayer and therefore subject to strong finite size effects. As larger supercells would be prohibitively expensive, and the primary use of hematite is as a photoanode, I do not consider the electron polaron further in this work.

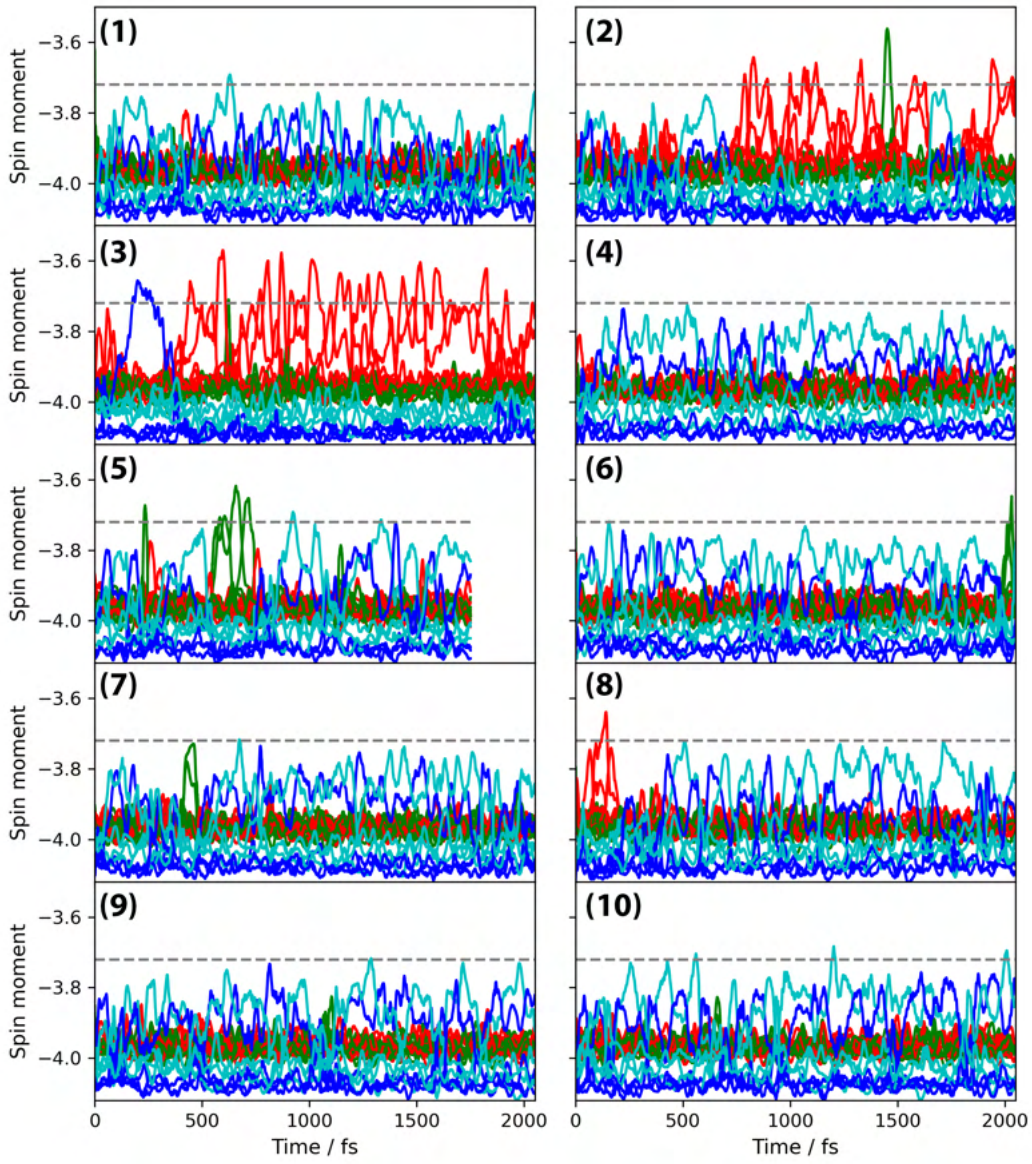

Figure 6.6: Electron polaron spin moment at the hematite/water interface. Spin moments of all iron atoms where the hole polaron may localise, shown for 10 statistically independent DFT-MD trajectories starting from completely different nuclear configurations. Red line refers to the 'B' Fe-bilayer, green line to the 'D' Fe-bilayer, light blue to the 'F_b' row of the F-bilayer and dark blue to the 'F_i' row of the F-bilayer. Dashed line shows the spin moment of the hole polaron from DFT geometry optimisation of bulk hematite. Refer to Figure 6.1 for layer labelling. I note that due to the significant computational cost, DFT-MD for trajectory 5 was stopped before the 2ps MD was complete.

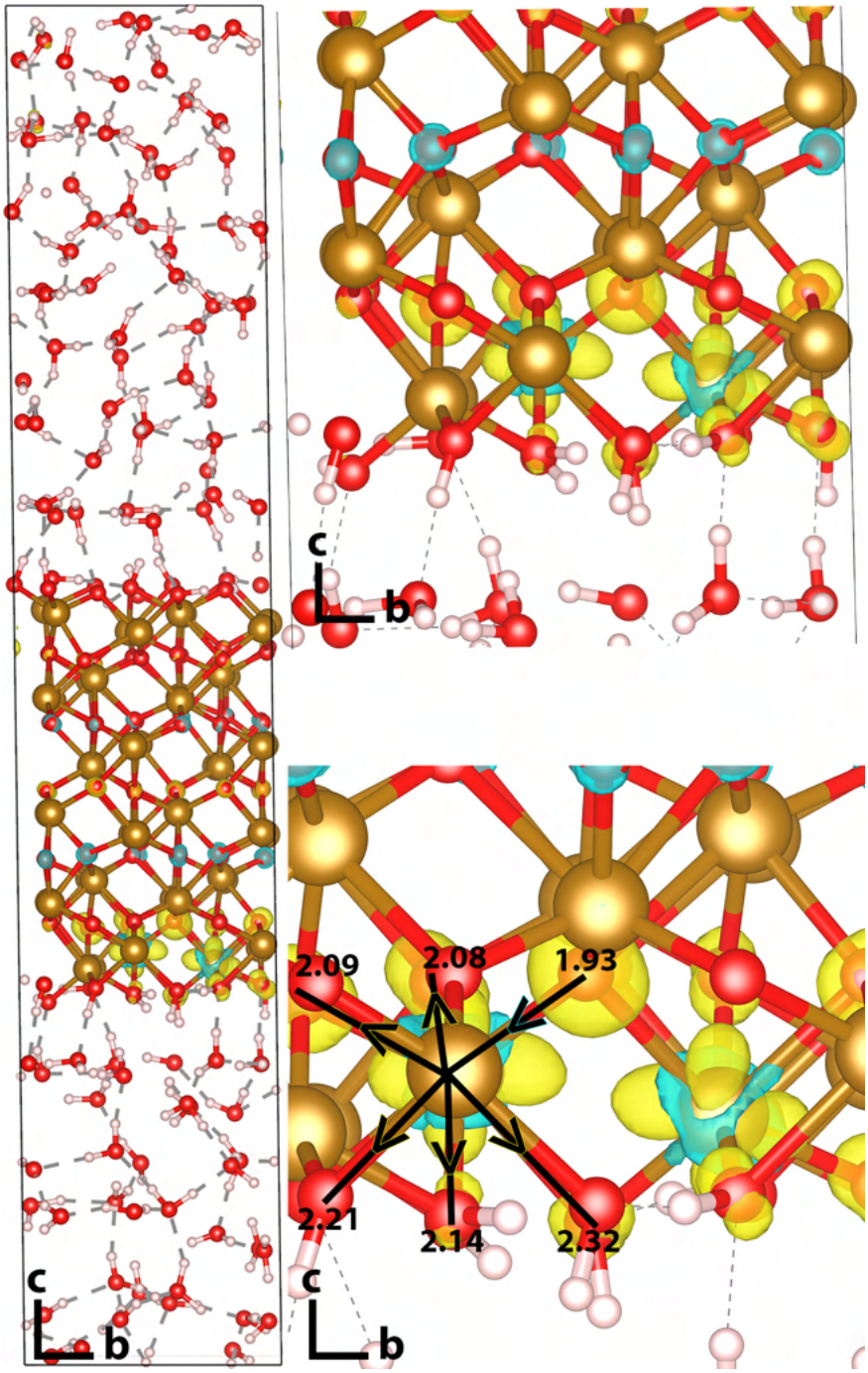

Figure 6.7: Electron polaron excess spin density at the hematite/liquid water interface. All plots correspond to the final geometry of trajectory 4, with an average Fe-O bond length of 2.12 Å for the 'F_i' row and 2.13 Å for the 'F_b' row. For comparison, the average Fe-O bond lengths for iron atoms where the electron polaron does not localise are 2.08 Å for both the 'F_b' and 'F_i' row. The electron polaron has been localised on these two iron atoms for the 2 ps of DFT-MD, and therefore should be close to equilibrium. Bond lengths between one of the iron atoms and bonded oxygen atoms are shown in Angstrom. Arrows show contraction and elongation of the Fe-O bonds with respect to their neutral bond lengths.

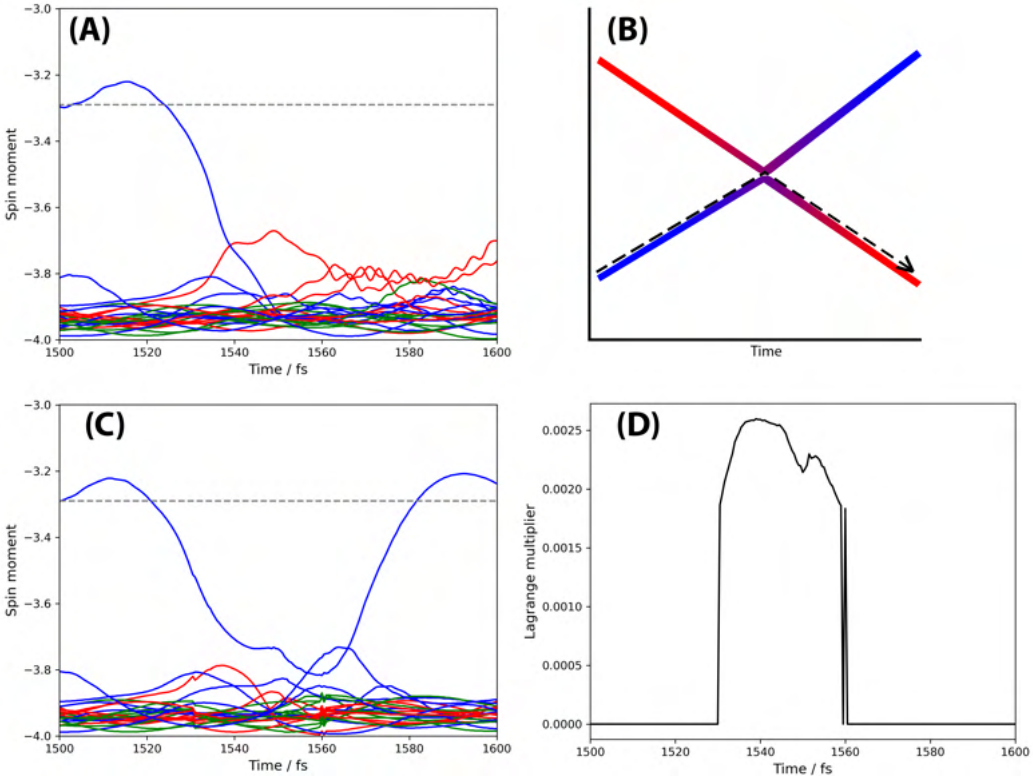

Figure 6.8: Trivial crossing during DFT-MD of bulk hematite. (A) spin moment of all iron atoms where the hole polaron may localise during DFT-MD, (B) a schematic of the the energy levels where the line color represents the diabatic identity of each energy surface (inspired by Ref [190]), (C) spin moment of all iron atoms where the hole polaron may localise during CDFT-MD using a spin constraint for the total spin moment of iron atoms on the 'B' and 'D' Fe-bilayers and (D) the value of the Lagrange multiplier during CDFT-MD.

6.3 Trivial crossings

In Figures 6.2-6.3 there are 5 total successful hole polaron hops in 20 ps of DFT-MD, with an equal number of trivial crossings. Trivial crossings refer to crossings of the potential energy surfaces where there is no interaction, but as a result of not propagating continuously the electronic state the system moves into the wrong potential energy surface [189, 190]. For example at around 1450 fs in trajectory 6 a polaron localised on the 'B' layer moves to the interfacial 'F' layer, which would correspond to transport through 3 Fe-bilayers and a distance greater than 10 Å. This clearly does not correspond to a genuine hopping or tunnelling event of the hole polaron, but instead a trivial crossing.

One possible method for preventing these trivial crossings, with minimal com-

putational cost, is CDFT as explored in Chapter 5. By constraining the total spin moment of the 'B' and 'D' Fe-bilayers, erroneous localisation of the hole polaron on these layers can be prevented. Figure 6.8 shows an example of this, for DFT-MD of bulk hematite chosen as a simpler test of this methodology. When the total spin spin moment of iron atoms on the 'B' and 'D' Fe-bilayer increases above their mean value of -63$\pm$0.2, the CDFT SCF loop activates and the Lagrange multiplier (Eq. 2.18) becomes finite. For around 30 fs the system is propagated using CDFT-MD, preventing the increase in spin density over the 'B' and 'D' Fe-bilayers. As CDFT only activates in response to an increase in spin density over the incorrect Fe-bilayers, this is effectively a post-hoc correction and not a replacement for non-adiabatic molecular dynamics. Furthermore, because the system is not propagated with self-consistent CDFT there is no conservation of total energy. Refer to Chapter 5.2.2.1 for a discussion of CDFT-MD energy conservation. While further work is ongoing to examine this methodology further, CDFT-MD is currently too expensive and problematic for studying the dynamics at the hematite/liquid water interface.

An alternative to hybrid DFT-MD or CDFT-MD would be to use a machine learning model, which has been shown to perform well for the neutral interface [186]. The training data could combine DFT-MD with single point CDFT calculations where the hole polaron localises on an incorrect Fe-bilayer, which would provide a high energy penalty for these structures such that the machine learning model propagates the hole polaron continuously within the correct bilayer. Work towards this is currently in progress.

6.4 Charge delocalisation

In unpublished work in his thesis [191], Dr Guido Falk von Rudorff briefly examined the charged hematite/liquid water interface and identified charge delocalisation across the solvent as a concern. This is very similar to the previously studied Ru^{2+}-Ru^{3+} in aqueous solution (Chapter 5.2.2.3), where the calculated Hirshfeld charges were $Ru^{0.5+}$-$Ru^{1.5+}$ with the remaining charge delocalised across the solvent. It is likely that this charge delocalisation is a result of an incomplete electronic description of

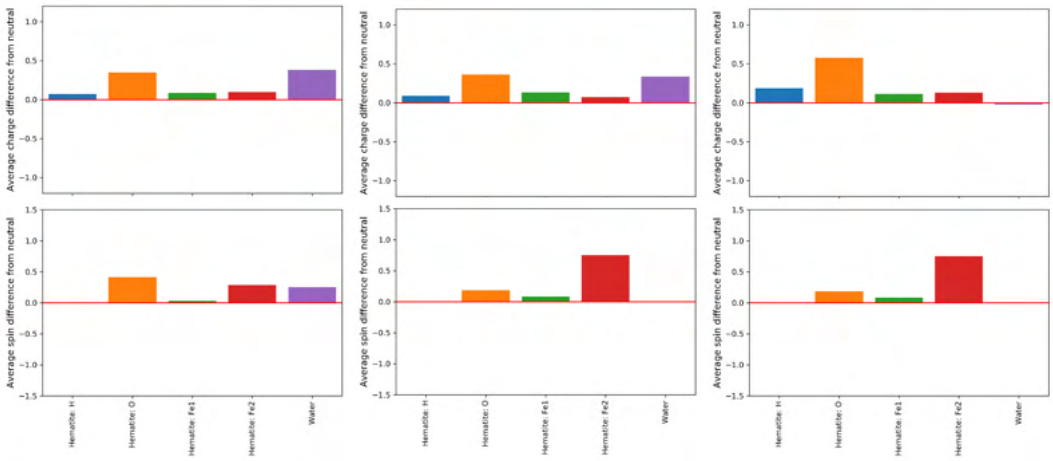

Figure 6.9: Charge delocalisation over the solvent at the hematite/liquid water interface. Average charge (top row) and spin (bottom row) difference from neutral calculated for: DFT on the neutral equilibrated geometry (left column), after 400 steps of excess hole DFT-MD (middle column) and a CDFT calculation constraining the total charge difference to the hematite slab. The neutral charge and spin are averaged over 500 structures from neutral DFT-MD calculated by Dr Guido Falk von Rudorff. Inspired by Ref [191]

liquid water, for example Sprik and co-workers [192] showed that the experimental water band gap of 8.7 eV [193] is underestimated with HSE06(25%) as 6.6 eV. This suggests that reproducing both the experimental band gap of bulk hematite and water with the same functional would be very challenging, as lowering the amount of HFX to 12% to reproduce the experimental band gap of bulk hematite will have the effect of further underestimating the water band gap. Sprik and co-workers [192] further found that the narrowing of the gap between the HOMO of water and the HOMO of the electrode places the valence band of water almost in coincidence with the electroactive levels of the electrode, which is likely the cause of the charge delocalisation found in this work. I do note however that for structural properties and dynamics, such as the radial distribution function and the self-diffusion coefficient, HSE06(12%) has been shown to provide good agreement with experiment [97, 186]. As such, it would be prudent to investigate this charge delocalisation problem further, and to examine the effect of using CDFT to constrain the total charge to the hematite slab.

Figure 6.9 shows a reproduction of Figure 3.41 from the thesis of Dr Guido Falk von Rudorff [191], but where the calculations are performed with the more strongly

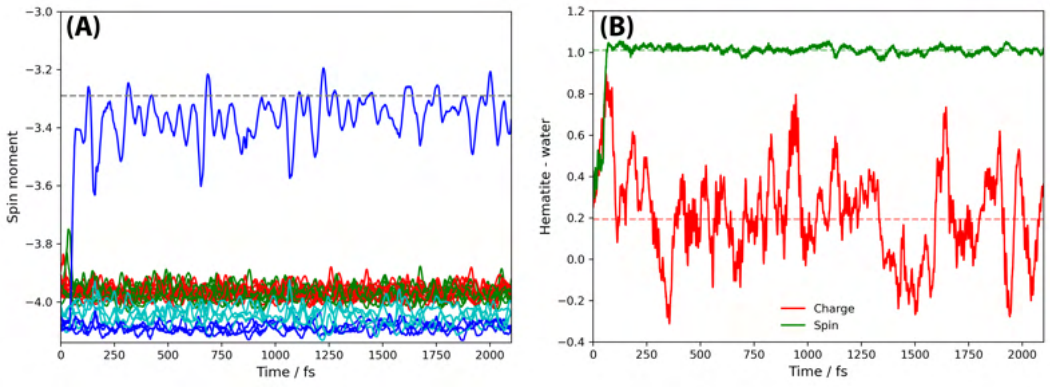

Figure 6.10: Charge delocalisation over the solvent at the hematite/liquid water interface. (A) spin moments of all iron atoms where the hole polaron may localise for trajectory 8 (see Fig 6.2), (B) difference in charge (red) and spin (green) between hematite slab and water. As the hole polaron localises onto a single iron atom the spin difference becomes 1.0, while the charge remains delocalised over both the hematite slab and water with an average value of 0.2 corresponding to (1-0.20)/2=40% of the charge delocalised across the solvent.

converged DFT parameters as discussed in Section 6.1. This is important because with the under-converged DFT criteria, Dr Guido Falk von Rudorff found that there was no hole polaron at the hematite/liquid water interface. Despite this, there is qualitative agreement between Figure 6.9 and Figure 3.41 from the thesis of Guido Falk von Rudorff [191], as in both sets of calculations ∼40% of the excess charge is delocalised over the solvent. Notably, there is no significant difference in charge delocalisation for the delocalised hole polaron or the localised hole polaron. This is in agreement with bulk DFT calculations in Chapter 3, where it was found that the hole polaron localises without any significant change in charge. The formation of a hole polaron is indicated only by a change in spin moment, consistent with Figure 6.9 where the spin moment over the iron atoms labelled 'Fe2' (layers B, D and F in Figure 6.1) increases and the spin moment over the solvent decreases to zero.

While useful for reference, Figure 6.9 is problematic as this requires comparison to neutral DFT-MD which may not be statistically converged and makes analysis more challenging. As an alternative, Figure 6.10 shows a plot of the difference in charge and spin between the hematite slab and solvent as a function of time for 2 ps of DFT-MD. Table 6.1 summarises this information, showing the average charge and spin for each trajectory. In agreement with Figure 6.9, at time 0 fs before nuclear

Table 6.1: Charge delocalisation over the solvent at the hematite/liquid water interface. For each trajectory, the total charge difference ('ΔTotal charge') and total spin difference ('ΔTotal spin') between the hematite slab and water is shown. The spin moment for the iron atom where the electron or hole polaron is localised is shown for both DFT ('DFT polaron') and CDFT ('CDFT polaron'), as well as the difference ('ΔPolaron'). The average charge difference for the hole polaron is 0.24, corresponding to (1-0.24)/2=38% of the charge delocalised across the solvent, and for the electron polaron is 0.12, corresponding to (-1-0.12)/2=56% of the charge delocalised across the solvent. These values correspond to the final structures of 2 ps DFT-MD, shown in Figures 6.2-6.3 and 6.6.

Hole polaron					
Trajectory	ΔTotal charge	ΔTotal spin	DFT polaron	CDFT polaron	ΔPolaron
1	0.16	1.01	-3.249	-3.249	0.000
2	0.19	0.99	-3.322	-3.326	-0.004
3	(0.33)[a]	(1.55)[a]	-3.266	-3.266	0.000
4	0.20	1.00	-3.304	-3.271	0.033[b]
5	0.20	1.02	-3.304	-3.312	-0.008
6	0.39	1.01	-3.315	-3.318	-0.003
7	0.25	0.98	-3.332	-3.335	-0.003
8	0.32	1.00	-3.349	-3.351	-0.002
9	0.19	1.01	-3.313	-3.318	-0.005
10	0.25	0.98	-3.300	-3.301	-0.001
Average	0.24	1.00			-0.003
Electron polaron					
1	0.07	1.00	-3.870, -3.837	-3.863, -3.837	-0.007, 0.000
2	0.16	0.99	-3.822, -3.661	-3.821, -3.661	0.001, 0.000
3	0.23	0.98	-3.821, -3.762	-3.821, -3.761	0.000, 0.001
4	0.10	1.01	-3.871, -3.861	-3.865, -3.861	0.006, 0.000
5	0.15	1.00	-3.847, -3.840	-3.845, -3.834	0.002, 0.006
6	0.08	1.00	-3.953, -3.741	-3.946, -3.744	0.007, -0.003
7	-0.06	0.99	-3.969. -3.865	-3.959, -3.874	0.010, -0.009
8	0.11	1.02	-3.953, -3.845	-3.945, -3.845	0.008, 0.000
9	0.15	0.99	-3.960, -3.820	-3.959, -3.810	0.001, 0.010
10	0.19	1.00	-3.856, -3.809	-3.850, -3.812	0.006, -0.003
Average	0.12	1.00			0.002

[a] Trajectory 3 hole polaron has a highly unusual starting geometry, where one interfacial iron atom has left the Fe-bilayer and moved closer to the water. This is a very rare event observed during neutral DFT-MD with the ML model, and work is ongoing to determine the validity of this structure. As such, the Hirshfeld charge and spin moment do not count towards the average values shown.

[b] Trajectory 4 hole polaron undergoes an trivial crossing around 1850 fs, and therefore the difference in CDFT and DFT spin moment is caused by the resulting non-equilibrium state. See Section 6.3.

relaxation when the hole polaron is delocalised, a small amount of spin is delocalised over the water. Following nuclear relaxation, the spin difference becomes 1.0 while the charge persists with around 38% delocalised across the solvent even after 2 ps of DFT-MD.

These results show that while ∼40% of the excess charge is delocalised across the solvent, the excess spin is 100% over the hematite slab. As the polaron in hematite localises with a change in spin, this suggests that the hole polaron may not be significantly affected by this spurious charge delocalisation.

Table 6.1 also shows the change in spin moment for the hole and electron polaron upon constraining 100% of the excess charge to the hematite slab using CDFT. It is found that the change in spin moment is 0.00 for both the electron and hole polaron, such that the excess charge is fully delocalised over the hematite slab and does not affect the structure of the polaron. Unfortunately running CDFT-MD under this constraint breaks energy conservation, which is very similar to Chapter 5.2.4 where fully constraining the excess charge to a single unit in an organic semiconductor does not lead to successful geometry optimisation. It would appear that HSE06(12%) is not able to describe the state where 100% of the excess charge is localised on the hematite slab, and that a more sophisticated functional capable of reproducing the electronic structure of both bulk hematite and water would be required. However, despite these caveats it is reassuring that there is no immediate change in polaron structure upon constraining 100% of the excess charge to the hematite slab.

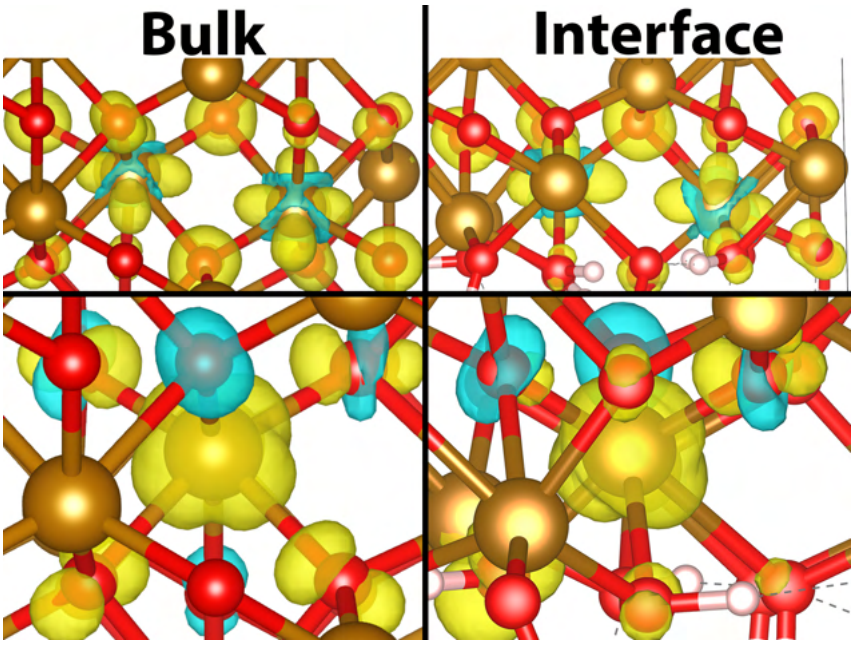

Figure 6.11: Comparison of polaron structure for bulk hematite and at the hematite/liquid water interface. Excess spin density for an excess electron (top row) and an electron hole (bottom row) for bulk hematite (left column) and at the hematite/liquid water interface (right column). The polaron structures are qualitatively the same, and the visible differences in excess spin density are largely caused by the different methodologies used: geometry optimisation for bulk hematite, and 400 K DFT-MD for the hematite/liquid water interface.

6.5 Conclusion

In this Chapter electron and hole polaron structures and charge transport have been investigated at the hematite/liquid water interface. A total of 20 ps DFT-MD has been performed for the excess electron and electron hole, demonstrating that both polarons relax from a delocalised band state to polarons localised at the interfacial Fe-bilayer. The structures of the electron and hole polaron at the hematite/liquid water interface are qualitatively the same as those found from calculations of bulk hematite, with a final comparison of the excess spin density show in Figure 6.11.

The presence of the interface breaks the symmetry of the Fe-bilayer present in bulk hematite, such that hole polarons localised on the row of the Fe-bilayer closest to the interface (referred to as the 'F_i' row) have a larger reorganisation energy than hole polarons localised on the row of the bilayer further from the interface (referred to as the 'F_b' row). Furthermore no 'F_i' to 'F_b' hole polaron hopping events

were observed during the 20 ps dynamics, which suggests that that hole polarons may become trapped on iron atoms closest to the interface for long periods of time. As such, in comparison to bulk hematite the hole mobility at the hematite/liquid water interface is expected to be greatly reduced. This preferential trapping at the interface may be beneficial in the context of water splitting, allowing sufficient time for chemical reactions to take place.

The electron polaron delocalises across two Fe atoms, which are on different rows of the Fe-bilayer, and therefore there is not expected to be any anisotropy of the mobility as for the hole polaron. The 2 x 2 x 1 hematite slab used in this work is not sufficiently large to describe the dynamics of the electron polaron, as the transfer shown to have the largest effect on the mobility in bulk hematite (Chapter 4.2.3) would require delocalisation of the electron polaron across the entire Fe-bilayer. To fully describe the dynamics of the electron polaron larger system sizes would be required, which would be prohibitively expensive with hybrid DFT-MD. As the primary application of hematite is as a photoanode material, the hole polaron is of greater interest and therefore I expect that future work will focus on the hole polaron at the hematite/liquid water interface.

The DFT-MD performed in this Chapter is very expensive, and so for future work it is hoped that a machine learning model may be used to accelerate these calculations. This would allow for calculation of the hole mobility at the hematite/liquid water interface, which can be compared to the bulk mobilities calculated in Chapter 4.

Chapter 7

Conclusions and outlook

Charge transport has been identified as a key issue for the use of hematite in a number of technological applications, especially in photocatalysis and photoelectrochemistry [6, 9, 11, 154]. This thesis has provided a comprehensive and detailed understanding of the physical mechanisms that lead to the sluggish transport of charge carriers in bulk hematite, and has further extended this analysis to the hematite/liquid water interface. To the best of my knowledge these are the most sophisticated calculations performed to date of hematite, using spin-constrained gap-optimised hybrid density functional theory in combination with large supercells.

In Chapter 3 I presented the structure of the excess electron and electron hole polarons and associated reorganisation energies for a series of bulk iron oxides: hematite ($\alpha-Fe_2O_3$), lepidocrocite ($\gamma-$FeOOH), goethite ($\alpha-$FeOOH) and white rust ($Fe(OH)_2$). The polaron structures and extent of charge localisation remains largely consistent across the studied iron oxides, except for the hole in goethite which according to my calculations is delocalised as a result of the energy penalty for disrupting the extended hydrogen bonding framework. This may make this material a promising candidate as a hole conducting material.

Chapter 4 extended the work performed in Chapter 3, with calculation of both the electron and hole mobility for bulk hematite using CDFT. I was also to provide further insight into the 2-site delocalisation of the electron polaron identified for all iron oxides in Chapter 3, showing that $H_{ab} > \frac{\lambda}{2}$ such that the transition state of electron transfer theory becomes the minimum. I also discussed how the three-fold

degenerate tetragonal distortion of the Fe octahedron is responsible for the low hole mobility in hematite, calculated as 0.031 cm^2/Vs, a property well recognised to bear directly upon the photocatalytic behaviour of hematite [6, 9]. The higher mobility of the electron polaron, 0.098 cm^2/Vs, was attributed to a delocalisation over two neighbouring iron atoms, advantageous for charge transport due to the larger spatial displacements per transfer step.

In Chapter 5 I provided an extension to CDFT in the popular DFT package CP2K, implementing the necessary force terms which arise from a constraint based on Hirshfeld partitioning of the electron density. The previously used Becke partitioning was shown to predict qualitatively incorrect atomic charges, as a result of dividing space equally among all atoms. I verified and benchmarked this new implementation against systems previously studied in a plane-wave implementation of CDFT, showing good agreement for both geometry optimisation and molecular dynamics. Consistent with previous work [182], I found that an IASD markedly larger than 1 is an indicator of systems for which CDFT calculations can be unreliable. With the exception of these pathological cases, I found that CDFT is a powerful tool for the calculation of electron transfer parameters at a reasonable computational cost.

In Chapter 6 electron and hole polaron structures and charge transport was investigated at the hematite/liquid water interface. A total of 20 ps DFT-MD was been performed for both the excess electron and electron hole, demonstrating that both charges relax from a delocalised band state to polarons localised at the interfacial Fe-bilayer. The structures of the electron and hole polaron at the hematite/liquid water interface are qualitatively the same as those found from calculations of bulk hematite, however the presence of the interface breaks the symmetry of the Fe-bilayer and as a result the hole mobility is expected to be greatly reduced.

Outlook

While this thesis has presented new insight into the structure and dynamics of charge carriers in bulk hematite and other materials, there is still much to understand about

these differ for natural systems and in device applications. Chapter 6 provides a glimpse of future research that is made possible through the contributions of my work, extending the calculations of bulk hematite to the hematite/liquid water interface. Calculation of charge mobility at the interface would allow a better understanding of the rate-limiting transport processes governing photocatalytic water splitting efficiency [11, 154]. With a machine learning model it would also be possible to calculate other properties not accessible with standard DFT-MD, such as diffusion coefficients and thermodynamic integration to calculate free energy differences.

I have presented an implementation of the necessary force terms which arise from a constraint based on Hirshfeld partitioning of the electron density, which will allow for Hirshfeld based CDFT geometry optimisation and CDFT-MD in the popular DFT package CP2K. I expect this method to become valuable for the simulation of condensed phase electron transfer reactions, such across interfaces between different semiconductors or between semiconductors and liquid solutions, thus becoming part of the toolbox for first principles electrochemistry [155].

Alongside future computational work that this thesis has made possible, experimental studies may be motivated from my results. I predicted that the electron hole in goethite is fully delocalised, which makes this material a promising candidate as a hole conducting material. I would recommend that temperature dependent conductivity measurements be performed to verify if the temperature dependence is band-like.

A significant challenge for this work is that the charge mobility for undoped hematite is not known experimentally. I hope that motivated from this work, time of flight experiments [194] could be performed from which the mobility of undoped hematite can be calculated. It would also be valuable to see whether the electron and electron hole polaron structures predicted in this work are experimentally verifiable, such as with IR spectroscopy performed on thin hematite films.

Bibliography

[1] M. Dare-Edwards, J. Goodenough, A. Hamnett, and P. Trevelick. Electrochemistry and Photoelectrochemistry of Iron(III) Oxide. *J. Chem. Soc. Faraday Trans. I*, 79(1):2027–2041, 1983.

[2] Madeline Vargas, Kazem Kashefi, Elizabeth L. Blunt-Harris, and Derek R. Lovley. Microbiological evidence for Fe(III) reduction on early Earth. *Nature*, 395(6697):65–67, 1998.

[3] Carrick M. Eggleston. Geochemistry: Toward new uses for hematite. *Science*, 320(5873):184–185, 2008.

[4] Juliane Braunschweig, Julian Bosch, and Rainer U. Meckenstock. Iron oxide nanoparticles in geomicrobiology: From biogeochemistry to bioremediation. *New Biotechnol.*, 30(6):793–802, 2013.

[5] Allan Philippe and Gabriele E. Schaumann. Interactions of dissolved organic matter with natural and engineered inorganic colloids: A review. *Environ. Sci. Technol.*, 48(16):8946–8962, 2014.

[6] Kevin Sivula, Florian Le Formal, and Michael Grätzel. Solar water splitting: Progress using hematite (α-Fe_2O_3) photoelectrodes. *ChemSusChem*, 4(4):432–449, 2011.

[7] Alvaro Valdés, Jeremie Brillet, Michael Grätzel, Hildur Gudmundsdóttir, Heine A. Hansen, Hannes Jónsson, Peter Klüpfel, Geert Jan Kroes, Florian Le Formal, Isabela C. Man, Rafael S. Martins, Jens K. Nørskov, Jan Rossmeisl, Kevin Sivula, Aleksandra Vojvodic, and Michael Zäch. Solar hydrogen

production with semiconductor metal oxides: New directions in experiment and theory. *Phys. Chem. Chem. Phys.*, 14(1):49–70, 2012.

[8] Shenzhen Xu and Emily A. Carter. Theoretical Insights into Heterogeneous (Photo)electrochemical CO_2 Reduction. *Chem. Rev.*, 119(11):6631–6669, 2019.

[9] Qian Wang and Kazunari Domen. Particulate Photocatalysts for Light-Driven Water Splitting: Mechanisms, Challenges, and Design Strategies. *Chem. Rev.*, 120(2):919–985, 2020.

[10] Pierre-Marie Deleuze, Héléne Magnan, Antoine Barbier, Mathieu Silly, Bruno Domenichini, and Céline Dupont. Unraveling the Surface Reactivity of Pristine and Ti-Doped Hematite with Water. *J. Phys. Chem. Lett.*, 12(47):11520–11527, 2021.

[11] Jingguo Li, Hang Chen, Carlos A. Triana, and Greta R. Patzke. Hematite Photoanodes for Water Oxidation: Electronic Transitions, Carrier Dynamics, and Surface Energetics. *Angew. Chem. - Int. Ed.*, 60(34):18380–18396, 2021.

[12] Somnath Biswas, Spencer Wallentine, Savini Bandaranayake, and L. Robert Baker. Controlling polaron formation at hematite surfaces by molecular functionalization probed by XUV reflection-absorption spectroscopy. *J. Chem. Phys.*, 151(10):1–14, 2019.

[13] Tanehiro Nakau. Electrical conductivity of α-Fe_2O_3. *J. Phys. Soc. Jpn.*, 15(4):727–727, 1960.

[14] Driss Benjelloun, Jean Pierre Bonnet, Jean Pierre Doumerc, Jean Claude Launay, Marc Onillon, and Paul Hagenmuller. Anisotropie des proprietes electriques de l'oxyde de fer α-Fe_2O_3. *Mater. Chem. Phys.*, 10(6):503–518, 1984.

[15] Kevin M Rosso, Dayle M.A. Smith, and Michel Dupuis. An ab initio model of electron transport in hematite (α-Fe_2O_3) basal planes. *J. Chem. Phys.*, 118(14):6455–6466, 2003.

[16] Kevin M. Rosso and Eugene S. Ilton. Charge transport in micas: The kinetics of FeII/III electron transfer in the octahedral sheet. *J. Chem. Phys.*, 119(17):9207–9218, 2003.

[17] Kevin M. Rosso and Michel Dupuis. Reorganization energy associated with small polaron mobility in iron oxide. *J. Chem. Phys.*, 120(15):7050–7054, 2004.

[18] N. Iordanova, M. Dupuis, and K. M. Rosso. Charge transport in metal oxides: A theoretical study of hematite α-Fe_2O_3. *J. Chem. Phys.*, 122(14):144305, 2005.

[19] Konstantin Klyukin, Kevin M. Rosso, and Vitaly Alexandrov. Iron Dissolution from Goethite (α-FeOOH) Surfaces in Water by Ab Initio Enhanced Free-Energy Simulations. *J. Phys. Chem. C*, 122(28):16086–16091, 2018.

[20] Eric J. Bylaska and Kevin Rosso. Corresponding Orbitals Derived from Periodic Bloch States for Electron Transfer Calculations of Transition Metal Oxides. *J. Chem. Theory Comput.*, 14(8):4416–4426, 2018.

[21] Peilin Liao, Maytal Caspary Toroker, and Emily A. Carter. Electron transport in pure and doped hematite. *Nano Lett.*, 11(4):1775–1781, 2011.

[22] Peilin Liao and Emily A. Carter. Hole transport in pure and doped hematite. *J. Appl. Phys.*, 112(1):013701, 2012.

[23] R. F.G. Gardner, F. Sweett, and D. W. Tanner. The electrical properties of alpha ferric oxide-I. The impure oxide. *J. Phys. Chem. Solids*, 24(10):1175–1181, 1963.

[24] R. F.G. Gardner, F. Sweett, and D. W. Tanner. The electrical properties of alpha ferric oxide-II. Ferric oxide of high purity. *J. Phys. Chem. Solids*, 24(10):1183–1196, 1963.

[25] Artur Braun, Kevin Sivula, Debajeet K. Bora, Junfa Zhu, Liang Zhang, Michael Grätzel, Jinghua Guo, and Edwin C. Constable. Direct observation of two electron holes in a hematite photoanode during photoelectrochemical water splitting. *J. Phys. Chem. C*, 116(32):16870–16875, 2012.

[26] Joohee Lee and Seungwu Han. Thermodynamics of native point defects in α-Fe_2O_3: An ab initio study. *Phys. Chem. Chem. Phys.*, 15(43):18906–18914, 2013.

[27] Vladimir I. Anisimov, F. Aryasetiawan, and A. I. Lichtenstein. First-principles calculations of the electronic structure and spectra of strongly correlated systems: The LDA + U method. *J. Phys. Condens. Matter*, 9(4):767–808, 1997.

[28] Narjes Ansari, Kanchan Ulman, Matteo Farnesi Camellone, Nicola Seriani, Ralph Gebauer, and Simone Piccinin. Hole localization in Fe_2O_3 from density functional theory and wave-function-based methods. *Phys. Rev. Mater.*, 1(3):1–8, 2017.

[29] David Feller and Kirk A. Peterson. An examination of intrinsic errors in electronic structure methods using the Environmental Molecular Sciences Laboratory computational results database and the Gaussian-2 set. *J. Chem. Phys.*, 108(1):154–176, 1998.

[30] Guido Falk Von Rudorff, Rasmus Jakobsen, Kevin M. Rosso, and Jochen Blumberger. Hematite(001)-liquid water interface from hybrid density functional-based molecular dynamics. *J. Phys. Condens. Matter*, 28(39):394001, 2016.

[31] Zachary D. Pozun and Graeme Henkelman. Hybrid density functional theory band structure engineering in hematite. *J. Chem. Phys.*, 134(22):1–9, 2011.

[32] Vitaly Alexandrov and Kevin M. Rosso. Electron transport in pure and substituted iron oxyhydroxides by small-polaron migration. *J. Chem. Phys.*, 140(23):234701, 2014.

[33] Harald Oberhofer and Jochen Blumberger. Charge constrained density functional molecular dynamics for simulation of condensed phase electron transfer reactions. *J. Chem. Phys.*, 131(6):1–12, 2009.

[34] Jochen Blumberger and Keith P. McKenna. Constrained density functional theory applied to electron tunnelling between defects in MgO. *Phys. Chem. Chem. Phys.*, 15(6):2184–2196, 2013.

[35] M. Newton. Electron Transfer Reactions in Condensed Phases. *Annu. Rev. Phys. Chem.*, 35(1):437–480, 1984.

[36] Marshall D. Newton. Quantum Chemical Probes of Electron-Transfer Kinetics: The Nature of Donor-Acceptor Interactions. *Chem. Rev.*, 91(5):767–792, 1991.

[37] Jochen Blumberger. Recent Advances in the Theory and Molecular Simulation of Biological Electron Transfer Reactions. *Chem. Rev.*, 115(20):11191–11238, 2015.

[38] Anderson F.M. Santos, Lucyano J.A. Macedo, Mariana H. Chaves, Marisol Espinoza-Castañeda, Arben Merkoçi, Francisco Das Chagas A. Limac, and Welter Cantanhêde. Hybrid self-assembled materials constituted by ferromagnetic nanoparticles and tannic acid: A theoretical and experimental investigation. *J. Braz. Chem. Soc.*, 27(4):727–734, 2016.

[39] Jacob Spencer, Laura Scalfi, Antoine Carof, and Jochen Blumberger. Confronting surface hopping molecular dynamics with Marcus theory for a molecular donor-acceptor system. *Faraday Discuss.*, 195(0):215–236, 2016.

[40] Feng Wu and Yuan Ping. Combining Landau-Zener theory and kinetic Monte Carlo sampling for small polaron mobility of doped $BiVO_4$from first-principles. *J. Mater. Chem. A*, 6(41):20025–20036, 2018.

[41] Samuele Giannini, Antoine Carof, and Jochen Blumberger. Crossover from Hopping to Band-Like Charge Transport in an Organic Semiconductor Model: Atomistic Nonadiabatic Molecular Dynamics Simulation. *J. Phys. Chem. Lett.*, 9(11):3116–3123, 2018.

[42] Harald Oberhofer, Karsten Reuter, and Jochen Blumberger. Charge Transport in Molecular Materials: An Assessment of Computational Methods. *Chem. Rev.*, 117(15):10319–10357, 2017.

[43] Nicole Adelstein, Jeffrey B. Neaton, Mark Asta, and Lutgard C. De Jonghe. Density functional theory based calculation of small-polaron mobility in hematite. *Phys. Rev. B - Condens. Matter Mater. Phys.*, 89(24):245115, 2014.

[44] P Hohenberg and W Kohn. Inhomogeneous Electron Gas. *Phys. Rev.*, 136(3B):B864–B871, 1964.

[45] W Kohn and L J Sham. Self-Consistent Equations Including Exchange and Correlation Effects. *Phys. Rev.*, 140(4A):A1133–A1138, 1965.

[46] John P Perdew, Kieron Burke, and Matthias Ernzerhof. Generalized Gradient Approximation Made Simple. *Phys. Rev. Lett.*, 77(18):3865–3868, 1996.

[47] Aron J. Cohen, Paula Mori-Sánchez, and Weitao Yang. Challenges for density functional theory. *Chem. Rev.*, 112(1):289–320, 2012.

[48] J. P. Perdew and Alex Zunger. Self-interaction correction to density-functional approximations for many-electron systems. *Phys. Rev. B*, 23(10):5048–5079, 1981.

[49] Yingkai Zhang and Weitao Yang. A challenge for density functionals: Self-interaction error increases for systems with a noninteger number of electrons. *J. Chem. Phys.*, 109(7):2604–2608, 1998.

[50] Aron J. Cohen, Paula Mori-Sánchez, and Weitao Yang. Insights into current limitations of density functional theory. *Science*, 321(5890):792–794, 2008.

[51] Paula Mori-Sánchez, Aron J. Cohen, and Weitao Yang. Localization and delocalization errors in density functional theory and implications for band-gap prediction. *Phys. Rev. Lett.*, 100(14):1–4, 2008.

[52] Qin Wu and Troy Van Voorhis. Extracting electron transfer coupling elements from constrained density functional theory. *J. Chem. Phys.*, 125(16):164105, 2006.

[53] Qin Wu, Chiao Lun Cheng, and Troy Van Voorhis. Configuration interaction based on constrained density functional theory: A multireference method. *J. Chem. Phys.*, 127(16):164119, 2007.

[54] A. R. Elmaslmane, M. B. Watkins, and K. P. McKenna. First-Principles Modeling of Polaron Formation in TiO_2 Polymorphs. *J. Chem. Theory Comput.*, 14(7):3740–3751, 2018.

[55] John P. Perdew, Robert G. Parr, Mel Levy, and Jose L. Balduz. Density-functional theory for fractional particle number: Derivative discontinuities of the energy. *Phys. Rev. Lett.*, 49(23):1691–1694, 1982.

[56] A. Janotti, J. B. Varley, P. Rinke, N. Umezawa, G. Kresse, and C. G. Van De Walle. Hybrid functional studies of the oxygen vacancy in TiO_2. *Phys. Rev. B - Condens. Matter Mater. Phys.*, 81(8):085212, 2010.

[57] Aliaksandr V. Krukau, Oleg A. Vydrov, Artur F. Izmaylov, and Gustavo E. Scuseria. Influence of the exchange screening parameter on the performance of screened hybrid functionals. *J. Chem. Phys.*, 125(22):224106, 2006.

[58] Carlo Adamo and Vincenzo Barone. Toward reliable density functional methods without adjustable parameters: The PBE0 model. *J. Chem. Phys.*, 110(13):6158–6170, 1999.

[59] Jochen Heyd, Gustavo E. Scuseria, and Matthias Ernzerhof. Hybrid functionals based on a screened Coulomb potential. *J. Chem. Phys.*, 118(18):8207–8215, 2003.

[60] Jochen Heyd and Gustavo E. Scuseria. Efficient hybrid density functional calculations in solids: Assessment of the Heyd-Scuseria-Ernzerhof screened Coulomb hybrid functional. *J. Chem. Phys.*, 121(3):1187–1192, 2004.

[61] Jochen Heyd and Gustavo E. Scuseria. Assessment and validation of a screened Coulomb hybrid density functional. *J. Chem. Phys.*, 120(16):7274–7280, 2004.

[62] Viktor Atalla, Igor Ying Zhang, Oliver T. Hofmann, Xinguo Ren, Patrick Rinke, and Matthias Scheffler. Enforcing the linear behavior of the total energy with hybrid functionals: Implications for charge transfer, interaction energies, and the random-phase approximation. *Phys. Rev. B*, 94(3):1–17, 2016.

[63] Nicola Colonna, Ngoc Linh Nguyen, Andrea Ferretti, and Nicola Marzari. Koopmans-Compliant Functionals and Potentials and Their Application to the GW100 Test Set. *J. Chem. Theory Comput.*, 15(3):1905–1914, 2019.

[64] David M. Sherman. Electronic structures of iron(III) and manganese(IV) (hydr)oxide minerals: Thermodynamics of photochemical reductive dissolution in aquatic environments. *Geochim. Cosmochim. Acta*, 69(13):3249–3255, 2005.

[65] John P. Perdew, Adrienn Ruzsinszky, Jianmin Tao, Viktor N. Staroverov, Gustavo E. Scuseria, and Gábor I. Csonka. Prescription for the design and selection of density functional approximations: More constraint satisfaction with fewer fits. *J. Chem. Phys.*, 123(6):062201, 2005.

[66] Jianwei Sun, Adrienn Ruzsinszky, and Johnp Perdew. Strongly Constrained and Appropriately Normed Semilocal Density Functional. *Phys. Rev. Lett.*, 115(3):1–6, 2015.

[67] Vladimir I. Anisimov, Jan Zaanen, and Ole K. Andersen. Band theory and Mott insulators: Hubbard U instead of Stoner I. *Phys. Rev. B*, 44(3):943–954, 1991.

[68] Amra Peles. GGA+U method from first principles: Application to reduction-oxidation properties in ceria-based oxides. *J. Mater. Sci.*, 47(21):7542–7548, 2012.

[69] Xu Huang, Sai Kumar Ramadugu, and Sara E. Mason. Surface-Specific DFT + U Approach Applied to α-Fe_2O_3(0001). *J. Phys. Chem. C*, 120(9):4919–4930, 2016.

[70] Rossitza Pentcheva and Hasan Sadat Nabi. Interface magnetism in Fe_2O_3/$FeTiO_3$. *Phys. Rev. B*, 77(17):172405, 2008.

[71] Julian Velev, A. Bandyopadhyay, W. H. Butler, and S. Sarker. Electronic and magnetic structure of transition-metal-doped α-hematite. *Phys. Rev. B - Condens. Matter Mater. Phys.*, 71(20):205208, 2005.

[72] G. Rollmann, A. Rohrbach, P. Entel, and J. Hafner. First-principles calculation of the structure and magnetic phases of hematite. *Phys. Rev. B*, 69(16):165107, 2004.

[73] J Klimeš and A Michaelides. Perspective: Advances and challenges in treating van der Waals dispersion forces in density functional theory. *J. Chem. Phys.*, 137:120901–120913, 2012.

[74] J. G. Brandenburg, J. E. Bates, J. Sun, and J. P. Perdew. Benchmark tests of a strongly constrained semilocal functional with a long-range dispersion correction. *Phys. Rev. B*, 94(11):17–19, 2016.

[75] Zeng Hui Yang, Haowei Peng, Jianwei Sun, and John P. Perdew. More realistic band gaps from meta-generalized gradient approximations: Only in a generalized Kohn-Sham scheme. *Phys. Rev. B*, 93(20):1–9, 2016.

[76] John P. Perdew and Adrienn Ruzsinszky. Density-functional energy gaps of solids demystified. *Eur. Phys. J. B*, 91(6):108, 2018.

[77] Eric B. Isaacs and Chris Wolverton. Performance of the strongly constrained and appropriately normed density functional for solid-state materials. *Phys. Rev. Mater.*, 2(6):1–11, 2018.

[78] Gopalakrishnan Sai Gautam and Emily A. Carter. Evaluating transition metal oxides within DFT-SCAN and SCAN+U frameworks for solar thermochemical applications. *Phys. Rev. Mater.*, 2(9):1–14, 2018.

[79] Yitao Si, Mingtao Li, Zhaohui Zhou, Maochang Liu, and Oleg Prezhdo. Improved description of hematite surfaces by the SCAN functional. *J. Chem. Phys.*, 152(2):024706, 2020.

[80] Benjamin Kaduk, Tim Kowalczyk, and Troy Van Voorhis. Constrained density functional theory. *Chem. Rev.*, 112(1):321–370, 2012.

[81] Aurélien de la Lande and Dennis R. Salahub. Derivation of interpretative models for long range electron transfer from constrained density functional theory. *J. Mol. Struct. THEOCHEM*, 943(1-3):115–120, 2010.

[82] Keith P. McKenna and Jochen Blumberger. Crossover from incoherent to coherent electron tunneling between defects in MgO. *Phys. Rev. B - Condens. Matter Mater. Phys.*, 86(24):245110, 2012.

[83] Adam Kubas, Felix Hoffmann, Alexander Heck, Harald Oberhofer, Marcus Elstner, and Jochen Blumberger. Electronic couplings for molecular charge transfer: Benchmarking CDFT, FODFT and FODFTB against high-level ab initio calculations. *J. Chem. Phys.*, 140(10):104105, 2014.

[84] Nico Holmberg and Kari Laasonen. Efficient Constrained Density Functional Theory Implementation for Simulation of Condensed Phase Electron Transfer Reactions. *J. Chem. Theory Comput.*, 13(2):587–601, 2017.

[85] Jan Řezáč, Bernard Lévy, Isabelle Demachy, and Aurélien De La Lande. Robust and efficient constrained DFT molecular dynamics approach for biochemical modeling. *J. Chem. Theory Comput.*, 8(2):418–427, 2012.

[86] Marko Melander, Elvar O. Jónsson, Jens J. Mortensen, Tejs Vegge, and Juan Maria García Lastra. Implementation of Constrained DFT for Computing Charge Transfer Rates within the Projector Augmented Wave Method. *J. Chem. Theory Comput.*, 12(11):5367–5378, 2016.

[87] Matthew B. Goldey, Nicholas P. Brawand, Márton Vörös, and Giulia Galli. Charge Transport in Nanostructured Materials: Implementation and Verification of Constrained Density Functional Theory. *J. Chem. Theory Comput.*, 13(6):2581–2590, 2017.

[88] He Ma, Wennie Wang, Siyoung Kim, Man-Hin Ma-Hin Cheng, Marco Govoni, and Giulia Galli. PyCDFT: A Python package for constrained density functional theory. *J. Comput. Chem.*, 41(20):1–9, 2020.

[89] Joost Vandevondele, Matthias Krack, Fawzi Mohamed, Michele Parrinello, Thomas Chassaing, and Jürg Hutter. Quickstep: Fast and accurate density functional calculations using a mixed Gaussian and plane waves approach. *Comput. Phys. Commun.*, 167(2):103–128, 2005.

[90] Thomas D. Kühne, Marcella Iannuzzi, Mauro Del Ben, Vladimir V. Rybkin, Patrick Seewald, Frederick Stein, Teodoro Laino, Rustam Z. Khaliullin, Ole Schütt, Florian Schiffmann, Dorothea Golze, Jan Wilhelm, Sergey Chulkov, Mohammad Hossein Bani-Hashemian, Valéry Weber, Urban Borštnik, Mathieu Taillefumier, Alice Shoshana Jakobovits, Alfio Lazzaro, Hans Pabst, Tiziano Müller, Robert Schade, Manuel Guidon, Samuel Andermatt, Nico Holmberg, Gregory K. Schenter, Anna Hehn, Augustin Bussy, Fabian Belleflamme, Gloria Tabacchi, Andreas Glöß, Michael Lass, Iain Bethune, Christopher J. Mundy, Christian Plessl, Matt Watkins, Joost VandeVondele, Matthias Krack, Jürg Hutter, Urban Borstnik, Mathieu Taillefumier, Alice Shoshana Jakobovits, Alfio Lazzaro, Hans Pabst, Tiziano Müller, Robert Schade, Manuel Guidon, Samuel Andermatt, Nico Holmberg, Gregory K. Schenter, Anna Hehn, Augustin Bussy, Fabian Belleflamme, Gloria Tabacchi, Andreas Glöß, Michael Lass, Iain Bethune, Christopher J. Mundy, Christian Plessl, Matt

Watkins, Joost VandeVondele, Matthias Krack, and Jürg Hutter. CP2K: An Electronic Structure and Molecular Dynamics Software Package – Quickstep: Efficient and Accurate Electronic Structure Calculations. *J. Chem. Phys.*, 194103(19):194103, 2020.

[91] Manuel Guidon, Jürg Hutter, and Joost VandeVondele. Robust periodic Hartree-Fock exchange for large-scale simulations using Gaussian basis sets. *J. Chem. Theory Comput.*, 5(11):3010–3021, 2009.

[92] Manuel Guidon, Jürg Hutter, and Joost Vandevondele. Auxiliary density matrix methods for Hartree-Fock exchange calculations. *J. Chem. Theory Comput.*, 6(8):2348–2364, 2010.

[93] Douglas L. Strout and Gustavo E. Scuseria. A quantitative study of the scaling properties of the Hartree-Fock method. *J. Chem. Phys.*, 102(21):8448–8452, 1995.

[94] Marc Haser and Reinhart Ahlrichs. Improvements on the Direct SCF Method. *J. Comput. Chem.*, 10(1):104–111, 1989.

[95] Manuel Guidon, Florian Schiffmann, Jürg Hutter, and Joost Vandevondele. Ab initio molecular dynamics using hybrid density functionals. *J. Chem. Phys.*, 128(21):214104, 2008.

[96] Joost VandeVondele and Jürg Hutter. Gaussian basis sets for accurate calculations on molecular systems in gas and condensed phases. *J. Chem. Phys.*, 127(11):114105, September 2007.

[97] Guido Falk Von Rudorff, Rasmus Jakobsen, Kevin M. Rosso, and Jochen Blumberger. Fast Interconversion of Hydrogen Bonding at the Hematite (001)-Liquid Water Interface. *J. Phys. Chem. Lett.*, 7(7):1155–1160, 2016.

[98] Guido Falk Von Rudorff, Rasmus Jakobsen, Kevin M. Rosso, and Jochen Blumberger. Improving the Performance of Hybrid Functional-Based Molecu-

lar Dynamics Simulation through Screening of Hartree-Fock Exchange Forces. *J. Chem. Theory Comput.*, 13(5):2178–2184, 2017.

[99] Martin E. McBriarty, Guido Falk Von Rudorff, Joanne E. Stubbs, Peter J. Eng, Jochen Blumberger, and Kevin M. Rosso. Dynamic Stabilization of Metal Oxide-Water Interfaces. *J. Am. Chem. Soc.*, 139(7):2581–2584, 2017.

[100] Oliver R Gittus, Guido Falk Von Rudorff, Kevin M Rosso, and Jochen Blumberger. Acidity Constants of the Hematite−Liquid Water Interface from Ab Initio Molecular Dynamics. *J. Phys. Chem. Lett.*, 9:5574–5582, 2018.

[101] Stefan Grimme, Stephan Ehrlich, and Lars Goerigk. Effect of the damping function in dispersion corrected density functional theory. *J. Comput. Chem.*, 32(7):1456–1465, 2011.

[102] Ernest Pastor, Ji Sang Park, Ludmilla Steier, Sunghyun Kim, Michael Grätzel, James R. Durrant, Aron Walsh, and Artem A. Bakulin. In situ observation of picosecond polaron self-localisation in α-Fe_2O_3photoelectrochemical cells. *Nat. Commun.*, 10(1):1–7, 2019.

[103] Christian S. Ahart, Jochen Blumberger, and Kevin M. Rosso. Polaronic structure of excess electrons and holes for a series of bulk iron oxides. *Phys. Chem. Chem. Phys.*, 22(19):10699–10709, 2020.

[104] Christian S. Ahart, Kevin M. Rosso, and Jochen Blumberger. Electron and Hole Mobilities in Bulk Hematite from Spin-Constrained Density Functional Theory. *J. Am. Chem. Soc.*, 144(10):4623–4632, 2022.

[105] E. N. Maslen, V. A. Streltsov, N. R. Streltsova, and N. Ishizawa. Synchrotron X-ray study of the electron density in α-Fe_2O_3. *Acta Crystallogr. B*, 50(4):435–441, 1994.

[106] A. P. Zhukhlistov. Crystal structure of lepidocrocite FeO(OH) from the electron-diffractometry data. *Crystallogr. Rep.*, 46(5):730–733, 2002.

[107] Yang Hexiong, Lu Ren, Robert T. Downs, and Gelu Costin. Goethite, α-FeO(OH), from single-crystal data. *Acta Crystallogr. Sect. E Struct. Rep. Online*, 62(12):250–252, 2006.

[108] John B. Parise, William G. Marshall, Ronald I. Smith, H. D. Luiz, and Hendrik Möller. The nuclear and magnetic structure of "white rust". *Am. Mineral.*, 85(1):189–193, 2000.

[109] E. Krén, P. Szabó, and G. Konczos. Neutron diffraction studies on the (1-x) Fe_2O_3-xRh_2O_3 system. *Phys. Lett.*, 19(2):103–104, 1965.

[110] A. Oleś, A. Szytuła, and A. Wanic. Neutron Diffraction Study of γ-FeOOH. *Phys. Status Solidi B*, 41(1):173–177, 1970.

[111] A. Szytula, A. Burewicz, Z. Dimitrij, S. Krasnick, H. Rzany, Todorovi.J, A Wanic, W Wolski, Z Dimitrijvic, S Krasnicki, and J Todorovic. Neutron Diffraction Studies of α-FeOOH. *Phys. Status Solidi*, 429(2):429–434, 1968.

[112] Stephen F. Nelsen, Silas C. Blackstock, and Yaesil Kim. Estimation of Inner Shell Marcus Terms for Amino Nitrogen Compounds by Molecular Orbital Calculations. *J. Am. Chem. Soc.*, 109(3):677–682, 1987.

[113] F. L. Hirshfeld. Bonded-atom fragments for describing molecular charge densities. *Theor. Chim. Acta*, 44(2):129–138, 1977.

[114] Oliver A. Dicks and Alexander L. Shluger. Theoretical modeling of charge trapping in crystalline and amorphous Al_2O_3. *J. Phys. Condens. Matter*, 29(31):314005, 2017.

[115] Samuele Giannini, Antoine Carof, Matthew Ellis, Hui Yang, Orestis George Ziogos, Soumya Ghosh, and Jochen Blumberger. Quantum localization and delocalization of charge carriers in organic semiconducting crystals. *Nat. Commun.*, 10(1):1–12, 2019.

[116] Jeanet Conradie. Jahn-Teller effect in high spin d4 and d9 octahedral metal-complexes. *Inorganica Chim. Acta*, 486:193–199, 2019.

[117] Patrick Bultinck, Christian Van Alsenoy, Paul W. Ayers, and Ramon Carbó-Dorca. Critical analysis and extension of the Hirshfeld atoms in molecules. *J. Chem. Phys.*, 126(14):11–13, 2007.

[118] Thomas A. Manz and Nidia Gabaldon Limas. Introducing DDEC6 atomic population analysis: Part 1. Charge partitioning theory and methodology. *RSC Adv.*, 6(53):47771–47801, 2016.

[119] Graeme Henkelman, Andri Arnaldsson, and Hannes Jónsson. A fast and robust algorithm for Bader decomposition of charge density. *Comput. Mater. Sci.*, 36(3):354–360, 2006.

[120] Sofie Van Damme, Patrick Bultinck, and Stijn Fias. Electrostatic potentials from self-consistent hirshfeld atomic charges. *J. Chem. Theory Comput.*, 5(2):334–340, 2009.

[121] Satish Kumar Iyemperumal and N. Aaron Deskins. Activation of CO_2 by supported Cu clusters. *Phys. Chem. Chem. Phys.*, 19(42):28788–28807, 2017.

[122] Indrani Choudhuri and Donald G. Truhlar. Calculating and Characterizing the Charge Distributions in Solids. *J. Chem. Theory Comput.*, 16(9):5884–5892, 2020.

[123] John J Carey, James A Quirk, and Keith P Mckenna. Hole Polaron Migration in Bulk Phases of TiO_2 Using Hybrid Density Functional Theory. *J. Phys. Chem. C*, 125(22):12441–12450, 2021.

[124] Taifeng Liu, Viswanath Pasumarthi, Christine Laporte, Zhaochi Feng, Qiuye Li, Jianjun Yang, Can Li, and Michel Dupuis. Bimodal hole transport in bulk $BiVO_4$ from computation. *J. Mater. Chem. A*, 6(8):3714–3723, 2018.

[125] Haibo Guo and Amanda S. Barnard. Proton transfer in the hydrogen-bonded chains of lepidocrocite: A computational study. *Phys. Chem. Chem. Phys.*, 13(39):17864–17869, 2011.

[126] R M Cornell and U Schwertmann. *The Iron Oxides: Structure, Properties, Reactions, Occurences and Uses*. Wiley-VCH, 2003.

[127] Henrik Christensen, A. Nørlund Christensen, Urho Turpeinen, Arne F. Andresen, Olav Smidsrød, Cha-On Pontchour, Pathana Phavanantha, Supanich Pramatus, Bjørg N. Cyvin, and Sven J. Cyvin. Hydrogen Bonds of γ-FeOOH. *Acta Chem. Scand.*, 32a:87–88, 1978.

[128] Silvia A. Fuente, Patricia G. Belelli, Norberto J. Castellani, and Marcelo Avena. LDA + U and GGA + U studies of Al-rich and bulk goethite (α-FeOOH). *Mater. Chem. Phys.*, 137(3):1012–1020, 2013.

[129] Nora H. de Leeuw and Timothy G. Cooper. Surface simulation studies of the hydration of white rust $Fe(OH)_2$, goethite α-FeO(OH) and hematite α-Fe_2O_3. *Geochim. Cosmochim. Acta*, 71(7):1655–1673, 2007.

[130] Sergio Speziale, Raymond Jeanloz, Alla Milner, Moshe Paz Pasternak, and Joseph M Zaug. Vibrational spectroscopy of $Fe(OH)_2$ at high pressure: Behavior of the O-H bond. *Phys. Rev. B - Condens. Matter Mater. Phys.*, 71(18):184106, 2005.

[131] H. D. Lutz, H. Möller, and M. Schmidt. Lattice vibration spectra. Part LXXXII. Brucite-type hydroxides $M(OH)_2$(M = Ca, Mn, Co, Fe, Cd) - IR and Raman spectra, neutron diffraction of $Fe(OH)_2$. *J. Mol. Struct.*, 328(C):121–132, 1994.

[132] H. D. Lutz, K. Beckenkamp, and H. Möller. Weak hydrogen bonds in solid hydroxides and hydrates. *J. Mol. Struct.*, 322(C):263–266, 1994.

[133] Matthew C.F. Wander, Kevin M. Rosso, and Martin A.A. Schoonen. Structure and charge hopping dynamics in green rust. *J. Phys. Chem. C*, 111(30):11414–11423, 2007.

[134] R. Hepzi Pramila Devamani and M. Alagar. Synthesis and characterisation of Iron II Hydroxide nano particles. *Elixir Nanotechnol.*, 61(1):16845–16848, 2013.

[135] Regla Ayala and Michiel Sprik. A classical point charge model study of system size dependence of oxidation and reorganization free energies in aqueous solution. *J. Phys. Chem. B*, 112(2):257–269, 2008.

[136] Stephan Lany and Alex Zunger. Assessment of correction methods for the band-gap problem and for finite-size effects in supercell defect calculations: Case studies for ZnO and GaAs. *Phys. Rev. B - Condens. Matter Mater. Phys.*, 78(23):17–20, 2008.

[137] C. Schlenker and M. Marezio. The order–disorder transition of Ti^{3+}–Ti^{3+} pairs in Ti_4O_7 and $(Ti_{1-x}V_x)_4O_7$. *Philos. Mag. B Phys. Condens. Matter Stat. Mech. Electron. Opt. Magn. Prop.*, 42(3):453–472, 1980.

[138] Morrel H. Cohen, E. N. Economou, and Costas M. Soukoulis. Small-bipolaron formation. *Phys. Rev. B*, 29(8):4496, 1984.

[139] Y. Yamada. Molecular polarons and valence fluctuations in Fe_3O_4. *Philos. Mag. B Phys. Condens. Matter Stat. Mech. Electron. Opt. Magn. Prop.*, 42(3):377–385, 1980.

[140] Alexander J.E. Rettie, Heung Chan Lee, Luke G. Marshall, Jung Fu Lin, Cigdem Capan, Jeffrey Lindemuth, John S. McCloy, Jianshi Zhou, Allen J. Bard, and C. Buddie Mullins. Combined charge carrier transport and photoelectrochemical characterization of $BiVO_4$ single crystals: Intrinsic behavior of a complex metal oxide. *J. Am. Chem. Soc.*, 135(30):11389–11396, 2013.

[141] Alexander J.E. Rettie, William D. Chemelewski, Jeffrey Lindemuth, John S. McCloy, Luke G. Marshall, Jianshi Zhou, David Emin, and C. Buddie Mullins. Anisotropic small-polaron hopping in W:$BiVO_4$ single crystals. *Appl. Phys. Lett.*, 106(2):022106, 2015.

[142] Julia Wiktor, Igor Reshetnyak, Francesco Ambrosio, and Alfredo Pasquarello. Comprehensive modeling of the band gap and absorption spectrum of $BiVO_4$. *Phys. Rev. Mater.*, 1(2):1–6, 2017.

[143] Taifeng Liu, Mengsi Cui, and Michel Dupuis. Hole Polaron Transport in Bismuth Vanadate $BiVO_4$ from Hybrid Density Functional Theory. *J. Phys. Chem. C*, 124(42):23038–23044, 2020.

[144] Robert Seidel, Stephan Thürmer, Jan Moens, Paul Geerlings, Jochen Blumberger, and Bernd Winter. Valence photoemission spectra of aqueous $Fe^{2+/3+}$ and $[Fe(CN)_6]^{4-/3-}$ and their interpretation by DFT calculations. *J. Phys. Chem. B*, 115(40):11671–11677, 2011.

[145] Robert Seidel, Manfred Faubel, Bernd Winter, and Jochen Blumberger. Single-ion reorganization free energy of aqueous $Ru(bpy)_3{}^{2+/3+}$ and $Ru(H2O)_6{}^{2+/3+}$ from photoemission spectroscopy and density functional molecular dynamics simulation. *J. Am. Chem. Soc.*, 131(44):16127–16137, 2009.

[146] Jan Moens, Robert Seidel, Paul Geerlings, Manfred Faubel, Bernd Winter, and Jochen Blumberger. Energy levels and redox properties of aqueous $Mn^{2+/3+}$ from photoemission spectroscopy and density functional molecular dynamics simulation. *J. Phys. Chem. B*, 114(28):9173–9182, 2010.

[147] H. M. Lu and X. K. Meng. Neel Temperature of Hematite Nanocrystals. *J. Phys. Chem.*, 114(49):21291–21295, 2010.

[148] F. J. Morin. Electrical properties of α-Fe_2O_3. *Phys. Rev.*, 93(6):1195–1199, 1954.

[149] B. M. Warnes, F. F. Aplan, and G. Simkovich. Electrical conductivity and seebeck voltage of Fe_2O_3, pure and doped, as a function of temperature and oxygen pressure. *Solid State Ion.*, 12(C):271–276, 1984.

[150] Pavan Kumar Behara and Michel Dupuis. Electron transfer in extended systems: Characterization by periodic density functional theory including the electronic coupling. *Phys. Chem. Chem. Phys.*, 22(19):10609–10623, 2019.

[151] H. J. Van Daal and A. J. Bosman. Hall effect in CoO, NiO, and α-Fe_2O_3. *Phys. Rev.*, 158(3):736–747, 1967.

[152] E. Gharibi, A. Hbika, B. Dupre, and C. Gleitzer. Electrical Properties of Pure and Titanium-Doped Hematite Single Crystals, in the Basal Plane, at Low Oxygen Pressure. *Eur. J. Solid State Inorg. Chem.*, 27(647):647–658, 1990.

[153] B. Zhao, T. C. Kaspar, T. C. Droubay, J. McCloy, M. E. Bowden, V. Shutthanandan, S. M. Heald, and S. A. Chambers. Electrical transport properties of Ti-doped Fe_2O_3(0001) epitaxial films. *Phys. Rev. B*, 84(24):245325, 2011.

[154] Daniel A. Grave, Natav Yatom, David S. Ellis, Maytal Caspary Toroker, and Avner Rothschild. The "Rust" Challenge: On the Correlations between Electronic Structure, Excited State Dynamics, and Photoelectrochemical Performance of Hematite Photoanodes for Solar Water Splitting. *Adv. Mater.*, 30(41):1706577, 2018.

[155] Jochen Blumberger, Yoshitaka Tateyama, and Michiel Sprik. Ab initio molecular dynamics simulation of redox reactions in solution. *Comput. Phys. Commun.*, 169(1-3):256–261, 2005.

[156] Christian S. Ahart, Kevin M. Rosso, and Jochen Blumberger. Implementation and validation of constrained density functional theory forces in the CP2K package. *J. Chem. Theory Comput.*, 2022.

[157] Alex M.P. Sena, Tsuyoshi Miyazaki, and David R. Bowler. Linear scaling constrained density functional theory in CONQUEST. *J. Chem. Theory Comput.*, 7(4):884–889, 2011.

[158] Calvin Ku and Patrick H.L. Sit. Oxidation-State Constrained Density Functional Theory for the Study of Electron-Transfer Reactions. *J. Chem. Theory Comput.*, 15(9):4781–4789, 2019.

[159] Qin Wu and Troy Van Voorhis. Direct optimization method to study constrained systems within density-functional theory. *Phys. Rev. - At. Mol. Opt. Phys.*, 72(2):7–10, 2005.

[160] Per Olov Löwdin. Quantum theory of many-particle systems. I. Physical interpretations by means of density matrices, natural spin-orbitals, and convergence problems in the method of configurational interaction. *Phys. Rev.*, 97(6):1474–1489, 1955.

[161] A. D. Becke. A multicenter numerical integration scheme for polyatomic molecules. *J. Chem. Phys.*, 88(4):2547–2553, 1988.

[162] Stefan Grimme, Jens Antony, Stephan Ehrlich, and Helge Krieg. A consistent and accurate ab initio parametrization of density functional dispersion correction (DFT-D) for the 94 elements H-Pu. *J. Chem. Phys.*, 132(15):154104, 2010.

[163] Matthias Ernzerhof and Gustavo E Scuseria. Assessment of the Perdew-Burke-Ernzerhof exchange-correlation functional. *J. Chem. Phys.*, 110(1998):5029–5036, 1999.

[164] Zdenek Futera and Jochen Blumberger. Electronic Couplings for Charge Transfer across Molecule/Metal and Molecule/Semiconductor Interfaces: Performance of the Projector Operator-Based Diabatization Approach. *J. Phys. Chem. C*, 121(36):19677–19689, 2017.

[165] John M. Herbert and Martin Head-Gordon. Accelerated, energy-conserving Born-Oppenheimer molecular dynamics via Fock matrix extrapolation. *Phys. Chem. Chem. Phys.*, 7(18):3269–3275, 2005.

[166] Anders M.N. Niklasson, Peter Steneteg, Anders Odell, Nicolas Bock, Matt Challacombe, C. J. Tymczak, Erik Holmström, Guishan Zheng, and Valery Weber. Extended Lagrangian Born-Oppenheimer molecular dynamics with dissipation. *J. Chem. Phys.*, 130(21), 2009.

[167] Julia Wiktor, Francesco Ambrosio, and Alfredo Pasquarello. Role of Polarons in Water Splitting: The Case of $BiVO_4$. *ACS Energy Lett.*, 3(7):1693–1697, 2018.

[168] Bruce S. Brunschwig, Carol Creutz, Donal H. MacArtney, T. K. Sham, and Norman Sutin. The role of inner-sphere configuration changes in electron-exchange reactions of metal complexes. *Faraday Discuss. Chem. Soc.*, 74(2):113–127, 1982.

[169] Jochen Blumberger and Michiel Sprik. Ab initio molecular dynamics simulation of the aqueous Ru^{2+}/Ru^{3+} redox reaction: The marcus perspective. *J. Phys. Chem. B*, 109(14):6793–6804, 2005.

[170] Jochen Blumberger and Michiel Sprik. Quantum versus classical electron transfer energy as reaction coordinate for the aqueous Ru^{2+}/Ru^{3+} redox reaction. *Theor. Chem. Acc.*, 115(2-3):113–126, 2006.

[171] A. D. Becke. Density-functional exchange-energy approximation with correct asymptotic behavior. *Phys. Rev. A*, 38(6):3098, 1988.

[172] Chengteh Lee, Weitao Yang, and Robert G. Parr. Development of the Colle-Salvetti correlation-energy formula into a functional of the electron density. *Phys. Rev. B*, 37(2):785, 1988.

[173] P J Stephen, F J Devlin, C F Chabalowski, and M J Frisch. Ab Initio Calculation of Vibrational Absorption. *J. Phys. Chem.*, 98(45):11623–11627, 1994.

[174] Jeng Da Chai and Martin Head-Gordon. Systematic optimization of long-range corrected hybrid density functionals. *J. Chem. Phys.*, 128(8), 2008.

[175] Jochen Blumberger and Guillaume Lamoureux. Reorganization free energies and quantum corrections for a model electron self-exchange reaction: Comparison of polarizable and non-polarizable solvent models. *Mol. Phys.*, 106(12-13):1597–1611, 2008.

[176] François P. Rotzinger. The self-exchange of a nonbonding electron via the outer-sphere pathway: Reorganizational energy and electronic coupling matrix element for the $V(OH_2)_6^{2+/3+}$, $Ru(OH_2)_6^{2+/3+}$, $V(OH_2)_6^{3+/4+}$, and $Ru(OH_2)_6^{3+/4+}$. *Dalton Trans.*, 728(5):719–728, 2002.

[177] Paul Bernhard, Lothar Helm, André E. Merbach, and Andreas Ludi. Direct Measurement of a Prominent Outer-Sphere Electron Self-Exchange: Kinetic Parameters for the Hexaaquaruthenium(II)/(III) Couple Determined by Oxygen-17 and Ruthenium-99 NMR. *J. Am. Chem. Soc.*, 107(2):312–317, 1985.

[178] Matthew Ellis, Hui Yang, Samuele Giannini, Orestis G. Ziogos, and Jochen Blumberger. Impact of Nanoscale Morphology on Charge Carrier Delocalization and Mobility in an Organic Semiconductor. *Adv. Mater.*, 33(45):1–8, 2021.

[179] Samuele Giannini and Jochen Blumberger. Charge Transport in Organic Semiconductors: The Perspective from Nonadiabatic Molecular Dynamics. *Acc. Chem. Res.*, 55(6):819–830, 2022.

[180] Simil Thomas, Hong Li, Raghunath R. Dasari, Austin M. Evans, Ioannina Castano, Taylor G. Allen, Obadiah G. Reid, Garry Rumbles, William R. Dichtel, Nathan C. Gianneschi, Seth R. Marder, Veaceslav Coropceanu, and Jean Luc Brédas. Design and synthesis of two-dimensional covalent organic frameworks with four-arm cores: Prediction of remarkable ambipolar charge-transport properties. *Mater. Horiz.*, 6(9):1868–1876, 2019.

[181] Samuele Giannini, Orestis George Ziogos, Antoine Carof, Matthew Ellis, and Jochen Blumberger. Flickering Polarons Extending over Ten Nanometres

Mediate Charge Transport in High-Mobility Organic Crystals. *Adv. Theory Simul.*, 3(9):1–11, 2020.

[182] Michael G. Mavros and Troy Van Voorhis. Communication: CDFT-CI couplings can be unreliable when there is fractional charge transfer. *J. Chem. Phys.*, 143(23):231102, 2015.

[183] Jeffrey G. Catalano. Weak interfacial water ordering on isostructural hematite and corundum (001) surfaces. *Geochim. Cosmochim. Acta*, 75(8):2062–2071, 2011.

[184] Thomas P. Trainor, Anne M. Chaka, Peter J. Eng, Matt Newville, Glenn A. Waychunas, Jeffrey G. Catalano, and Gordon E. Brown. Structure and reactivity of the hydrated hematite (0001) surface. *Surf. Sci.*, 573(2):204–224, 2004.

[185] Kunaljeet S. Tanwar, Sarah C. Petitto, Sanjit K. Ghose, Peter J. Eng, and Thomas P. Trainor. Fe(II) adsorption on hematite (0 0 0 1). *Geochim. Cosmochim. Acta*, 73(15):4346–4365, 2009.

[186] Philipp Schienbein and Jochen Blumberger. Nanosecond solvation dynamics of the hematite/liquid water interface at hybrid DFT accuracy using committee neural network potentials. *Phys. Chem. Chem. Phys.*, 24(25):15365–15375, 2022.

[187] Christoph Schran, Krystof Brezina, and Ondrej Marsalek. Committee neural network potentials control generalization errors and enable active learning. *J. Chem. Phys.*, 153(10), 2020.

[188] Andrei Pakoulev, Zhaohui Wang, and Dana D. Dlott. Vibrational relaxation and spectral evolution following ultrafast OH stretch excitation of water. *Chem. Phys. Lett.*, 371(5-6):594–600, 2003.

[189] Linjun Wang and Oleg V. Prezhdo. A simple solution to the trivial crossing problem in surface hopping. *J. Phys. Chem. Lett.*, 5(4):713–719, 2014.

[190] Elizabeth M.Y. Lee and Adam P. Willard. Solving the Trivial Crossing Problem while Preserving the Nodal Symmetry of the Wave Function. *J. Chem. Theory Comput.*, 15(8):4332–4343, 2019.

[191] Guido Falk Von Rudorff. *Structure and Dynamics of the Hematite / Liquid Water Interface*. PhD thesis, University College London, 2017.

[192] Jun Cheng and Michiel Sprik. Alignment of electronic energy levels at electrochemical interfaces. *Phys. Chem. Chem. Phys.*, 14(32):11245–11267, 2012.

[193] Annette Bernas, Christiane Ferradini, and Jean Paul Jay-Gerin. On the electronic structure of liquid water: Facts and reflections. *Chem. Phys.*, 222(2-3):151–160, 1997.

[194] Masahiro Funahashi. *Time-of-Flight Method for Determining the Drift Mobility in Organic Semiconductors*. John Wiley and Sons, Ltd, 2021.